POLITECNICO DI MILANO
DEPARTMENT OF PHYSICS
DOCTORAL PROGRAMME IN PHYSICS

Compressive sensing in Light Sheet Fluorescence Microscopy

Doctoral Dissertation of:
Gianmaria Calisesi

Supervisor:
Prof. Andrea Bassi
Tutor:
Prof.ssa Paola Taroni
The Chair of the Doctoral Program:
Prof. Marco Finazzi

Academic year 2020-2021, XXXIII PhD cycle

“Où finit le télescope, le microscope commence. *Lequel des deux a la vue la plus grande? Choisissez. Une moisissure est une pléiade de fleurs; une nébuleuse est une fourmilière d'étoiles. Même promiscuité, et plus inouïe encore, des choses de l'intelligence et des faits de la substance.”*

Foliis ac frondibus, Victor Hugo, les Misérables

CONTENTS

ABSTRACT

Light Sheet Fluorescence Microscopy (LSFM) also known as Selective Plane Illumination Microscopy (SPIM), is a fluorescence microscopy technique which, from its first publication in 2004, has been increasingly used in biological applications, from developmental biology to mounted tissues analysis. As an alternative to LSFM, Selective Volume Illumination (SVI) microscopy has been recently developed with the goal of further increasing the acquisition rate. As is the case of LSFM, SVI uses a perpendicular illumination and detection. In this technique, rather than illuminating the sample in a single plane, the incoming excitation beam is modulated across a confined volume. On top of this, Light emitting Diodes (LED) are usually not considered a good light source for Light Sheet Fluorescence Microscopy because the lack of spatial coherence makes it difficult to tightly focus light along one direction. However, using LED in fluorescence microscopy brings advantages such as colour availability, low cost, and reduced presence of speckle patterns.

In my PhD I demonstrated that, upon selectively illuminating a volume of the sample with LEDs, it is possible to volumetrically reconstruct it. The volumetric light

modulation is possible thanks to a spatial light modulator, which is coupled to an illumination orthogonal to the detection axis. In this configuration, the modulation happens within the depth of field of the detection objective. After the acquisition of N patterns, an inversion problem is solved, resulting in the sample volumetric reconstruction.

Furthermore, I illustrated how the use of patterned acquisition is compatible with Compressive Sensing, a signal analysis technique that reduces the number of modulation patterns to be acquired for a 3-dimensional reconstruction, compared to that given by the classical Nyquist-Shannon sampling criterion. This is achieved upon solving an ill-posed problem with further mathematical constraints which are related to the sample spatial features. The technique yields an accurate reconstruction of the sample anatomy even at significant compression ratios, up to compressed reconstruction in which only the 12.5% of the whole patterns set was used. Hence, the technique achieves higher volumetric acquisition rate, and eventually reduces photodamage on biological samples. In my PhD, I also demonstrated that the presented technique yields the absence of shadowing artifacts which are removed thanks to the broad spatial frequency support of an incoherent light source such as an LED.

Finally, once I obtained a technique in which the volume of imaging was ultimately limited by the sensor dimensions in the thesis it is reported a computational strategy based on deconvolution to overcome the limited Depth of Field extension. This limitation in fact hinders the imaging of thicker samples.

In the last part of my PhD, I extensively tested the cited strategies altogether, to assess for the overall achieved performances in samples like *Danio rerio*, a biological model in developmental and ecotoxicological studies and *Mus musculus*, i.e., lab mouse, imaged in different imaging media, both *in vivo* and *ex vivo*.

SOMMARIO

La microscopia a foglio di luce (LSFM), anche conosciuta come SPIM, è una tecnica di microscopia di fluorescenza che, dalla sua prima pubblicazione nel 2004, è stata sempre più usata per applicazioni biologiche, dalla biologia dello sviluppo all' analisi di tessuti. Come alternativa alla LSFM, la microscopia a illuminazione selettiva di volume (SVIM), è stata recentemente sviluppata con l'obiettivo di aumentare ulteriormente la velocità di acquisizione. Come nel caso della LSFM, la SVIM usa un'illuminazione perpendicolare al ramo di acquisizione. In questa tecnica, piuttosto che illuminare il campione su di un singolo piano, il fascio di illuminazione è modulato su di un volume limitato. Inoltre, diodi a emissione di luce (LED), non sono di solito considerato come buone sorgenti per la microscopia a foglio di luce poiché loro mancanza di coerenza spaziale rende difficile focalizzare finemente la luce su di una singola dimensione. In ogni caso, l'uso di LED in microscopia di fluorescenza porta vantaggi come disponibilità cromatica, basso costo e presenza ridotta di pattern a macchie.

Nel mio dottorato ho dimostrato come, dopo aver selettivamente illuminato una parte di campione con un LED, sia possibile ricostruirlo volumetricamente. La

modulazione volumetrica della luce è possibile grazie ad un modulatore spaziale di luce, che è accoppiato con un'illuminazione perpendicolare all'asse di raccolta. In questa configurazione, la modulazione è contenuta nella profondità di campo dell'obiettivo di raccolta. Dopo aver acquisito N pattern, si risolve un problema inverso, che ha come risultato la ricostruzione volumetrica del campione.

Oltretutto, Ho illustrato come l'impiego di pattern di acquisizione sia compatibile col Compressive Sensing (CS), una tecnica di analisi dei segnali che riduce il numero di pattern di modulazione da acquisire per una ricostruzione tridimensionale, rispettivamente al numero dato dal criterio classico di campionamento di Nyquist-Shannon. Ciò è ottenuto risolvendo un problema mal posto con ulteriori vincoli alla soluzione legati alle caratteristiche spaziali del campione. La tecnica apporta una ricostruzione accurata dell'anatomia del campione anche a compressioni significative, fino a ricostruzioni compresse in cui solo il 12.5% dei pattern totali è stato usato. Quindi la tecnica raggiunge velocità di acquisizione più elevate ed ottiene infine un ridotto danno al campione da esposizione alla luce. Nel mio PhD, ho anche dimostrato che la tecnica presentata mostra un'assenza di artefatti d'ombra, che sono rimossi grazie all'ampio supporto di frequenze spaziali di una sorgente di luce incoerente come un LED.

Infine, una volta ottenuta una tecnica il cui volume di imaging fosse in ultimo limitato dalle dimensioni del sensore, nella tesi è riportato una strategia computazionale basata sulla deconvoluzione per superare la limitata estensione della profondità di campo. Questo limite, infatti, impedisce di esaminare campioni più spessi.

Nell'ultima parte del mio dottorato, ho testato estensivamente nel complesso le sopracitate strategie, per quantificare le performance ottenute, in campioni come *Danio rerio,* un modello biologico per studi sullo sviluppo e sull'ecotossicologia, e come *Mus musculus,* topo da laboratorio, studiati in diversi mezzi di imaging, sia *in vivo* che *ex vivo*.

LIST OF FIGURES

1 FUNDAMENTALS

1.1 OPTICS AND THEORY

1.1.1 Optical systems

One of the most remarkable results in optics is the formulation of the resolution limit of an imaging system. This result has been obtained by Ernst Karl Abbe in 1873 and finds the smallest resolvable distance between two ideal point sources. It is expressed as function of the imaging wavelength and of the system capability of collecting light, represented by the so-called *numerical aperture* NA. This fundamental limit can be written as:

$$d = \frac{\lambda}{2 \cdot NA}, \qquad 1.1$$

and it varies accordingly to the imaging system geometrical and optical features, which are considered in its NA. In fact, $NA = n \cdot sen\theta$, with n being the refractive index of the imaging medium and θ being the half of the system maximum acceptance ray.

However, NA determines the optical system response to an object not only in the lateral and axial directions, but it affects the system response in the whole space. Let it be considered an microscope which is fed by fluorescence signal coming from a small point emitter: its characteristic behaviour in reply to such a stimulus is a fingerprint of the system itself and is the so-called Point Spread function (PSF). The Point Spread Function is one of the fundamental pieces involved in the process of image formation and it strongly influences how an object can be imaged.

The PSF mathematically represents the output diffraction pattern of light coming from an ideal point source, evaluated at the image plane after being transmitted through the imaging system. Said imaging system can collect light only from a limited angular cone, determined by its NA, which is then refocused at the image plane: this plane is in literature commonly referred to as *xy* plane. The limited light acceptance of any real system is such that it is practically impossible to recover a real point source. The light pattern that arises at the detection image plane is given by the interference of different converging light waves and is shaped as concentric rings which encircle a central bright peak [1]. The diameter of the most intense central peak is determined by the system NA, and it is related to the system resolution, as specified in Eq. 1.1. The obtained diffraction pattern takes the name after George Airy and, when considering ideal optics, is symmetrical both in axial and lateral directions. Nonetheless, real lenses suffer from different aberrations, which may result in a non-symmetrical image distortion, thus, downgrading the achievable image quality.

The knowledge of Point Spread Function of an fluorescence microscope brings together many valuable information aside from spatial resolution. Knowing in fact functional deviations from the ideal scenario, it is possible to correct for such nonidealities thanks to post processing routines which will be next introduced. If the mathematical expression of the imaging system transmission function is known as $h(x,y,z)$, the process of image $i(x,y,z)$ formation in a microscope can be formally described as a convolution between said function and the object spatial representation $o(x,y,z)$:

$$\begin{aligned} i(x,y,z) &= \iiint o(x',y',z')\, h(x-x',y-y',z-z')\, dx'dy'dz' \\ &= o(x,y,z) \otimes h(x,y,z), \end{aligned} \tag{1.2}$$

where the PSF has been assumed to be linear and space invariant. The first condition implies that the image taken of two objects simultaneously present on scene is identical to the sum of the images of the single objects, whereas the second condition signifies that the PSF does not depend on the position of the object on the field of view [2].

Known its spatial expression, the convolution operation can eventually be simplified if considered in the Fourier domain. In this domain in fact the spatial convolution is translated as a multiplication between the Fourier transform of the object and that of the PSF, so that:

$$\begin{gathered} \mathcal{F}\{i(x,y,z)\} = \mathcal{F}\{o(x,y,z) \otimes h(x,y,z)\} \\ I(u,v,w) = O(u,v,w) \cdot H(u,v,w) \end{gathered} \tag{1.3}$$

with $I(u, v, w)$ representing the image frequency representation and $H(u, v, w)$ the PSF Fourier transform, which is called Optical Transfer Function (OTF). Similarly as the PSF, the OTF explicit the response of the system to different spectral components [1]. Hence, an objective lens with infinite resolution would have unitary transmission for every frequency component. In practice, a real system acts as a low pass filter whose cut off frequency is directly related to its NA.

1.1.2 Deconvolution

Deconvolution is a computational technique whose goal is increasing the image quality upon considering the system nonidealities. In the field of microscopy, deconvolution has been widely used to compensate for PSF aberrations or broadening [3] and for rejecting light from out of focus planes.

Once the PSF is evaluated, either by theoretical simulation or by beads acquisition, Eq. 1.2 can be inverted to retrieve the imaged signal without, in principle, any loss introduced by the optical system. Being $\hat{o}$ the restored sample spatial distribution, it holds:

$$\hat{o} = \mathcal{F}^{-1}\left(I(u, v, w) \cdot \frac{1}{H(u, v, w)}\right) \qquad 1.4$$

However, Eq. 1.4 is not solvable in this form since the Optical Transfer function $H(u, v, w)$, rapidly goes to zero, so that I cannot be divided by H. Furthermore, up to this point it has not been considered any form of noise, which might induce unwanted artifacts in $\hat{o}$.

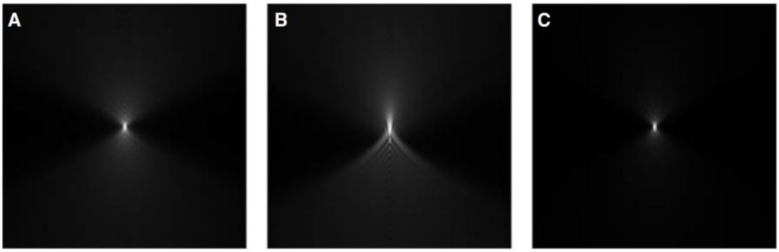

Figure i: Axial cross-sections of simulated PSFs for (A) an ideal widefield setup; (B) same microscope in A) but with introduced aberrations; and (C) ideal confocal PSF [4].

A possibility to overcome this mathematical impasse can be shown by recasting the problem in a matrix form:

$$\mathbf{i} = \mathbf{H}\mathbf{o} \qquad 1.5$$

Where $\mathbf{i}$ and $\mathbf{o}$ are vectors representing the spatial image and object representation, of size M, and $\mathbf{H}$ is $M \times M$ sized convolution operator with the PSF. From Eq. 1.5, it is possible to obtain a solvable, ill-posed inverse problem, which therefore needs for *a priori* information on the possible solution to restore $\mathbf{o}$. They have been proposed a variety of feasible algorithms, each of which has its own pros and cons, but none of them is generally preferred over the others, given the numerous possible conditions of use [4]. Finally, not only the solution depends on the chosen algorithm, but it also depends on the iteration parameters and starting conditions used in the reconstruction.

1.1.3 Deconvolution algorithms

As anticipated in the previous section, many possible solutions have been proposed throughout the years to obtain image deconvolution, an exhaustive review of which is given in [5], together with their working principle. One way of presenting these algorithms is dividing them by the underlying working principle; this leads to two main types of deconvolution algorithms, namely deblurring and image restoration algorithms.

To the first family they belong those methods which obtain cleaner images through noise rejection. This improvement can be achieved in different ways, but mainly by both considering the problem as a whole piece of information, (the so-called no-neighbours’ algorithms), or by considering the entire dataset as constituted by smaller, adjacent, piece of information (called nearest neighbours’ algorithms). In particular, this last class of deblurring strategies mitigates noise by dividing the starting volume acquisition into smaller chunks of 3 slices each. For each chunk of the volume, to the central slice it is subtracted both the previous and the sequent slice, thus obtaining a sharper image [6]. The procedure is completed once this operation is performed over every starting chunk. Differently to other families of deconvolution algorithms, deblurring methodologies do not take into consideration contribution of light coming from non-adjacent planes, making the restoration process computationally faster, but more subject to the introduction of artifacts or modification of pixels relative intensities.

A second category of deconvolution algorithms is that of linear filters. In this category, incoming out of focus photons, resulting in background noise are assigned back to their original plane in the volume. Differently from deblurring algorithms, linear filtering preserves the image intensity, i.e., the total number of photons acquired. One of the most used filters in image restoration is called Wiener filter, here, the object $\hat{o}$ is stepwise calculated as:

$$\hat{o} = \mathcal{F}^{-1}\left(I \cdot \frac{H^*}{|H|^2 + k}\right), \tag{1.6}$$

where H^* is the complex conjugate of the OTF, H and k is a reconstruction parameter which controls Signal to Noise Ratio (SNR). Despite being computationally simple and readily implementable, Wiener filtering might also output negative intensities, which may not be easy to handle.

Alternatively, nonlinear deconvolution approaches are a valuable option in image restoration. Said restoration is pursued over multiple iterations in which, at each step, a guess for the image is convolved with a PSF model and then compared to the starting frame. To “compare” means that an error metric must be defined, to quantify how far is the algorithm for a correct convergence towards the solution. Again, the correct choice for error metric must suit the type of noise, namely its statistics, involved in the imaging process. Usually in microscopy the experimental non idealities arise from shot noise, which follows a Poissonian statistics. For such condition, a maximum likelihood error metric has been shown to be an effective choice [7]. Among the many implementation of nonlinear filters, of the most famous iterative step is shown in [8] and is often referred to as Richardson-Lucy (RL), taking the form:

$$\hat{o}^{(t+1)} = \hat{o}^{(t)} \left(\frac{i}{\hat{o}^{(t)} \otimes PSF} \otimes PSF^{*} \right), \qquad 1.7$$

where t is the algorithm time step. With respect to other filters, a Richardson-Lucy iteration converges only to positive-valued images and it can reconstruct frequencies outside the Optical Transfer Function support but at cost of slow convergence. Nonetheless, RL performances can be greatly improved both in terms of convergence [9] and quality of the reconstructed image. The latter can be obtained by making a suitable initial guess of the object $\hat{o}^{(1)}$, which might be made from the raw experimental data or from a pre-processed result (with a linear filter, for example). Finally, non-linear deconvolution behaviour strongly depends on the object structure and on the accuracy of the PSF model used. In particular, frequency component outside the OTF support, which might be restored by the RL algorithm, can induce artefacts as well as shrinking in the restored image. Conversely, an inaccurate PSF in Eq. 1.7 will cause a failure in the reconstruction result.

To this aim, a third family of deconvolution approach has been proposed to tackle those situations in which an accurate PSF is difficult to model or measure, said family is that of blind deconvolutions. These methods, instead of processing object and PSF as two distinct elements, solve for the most likely combination of the two for a given dataset. However, for a better time performance and convergence, this last family of algorithms strongly needs for some *a priori* information either on the object or on the PSF. In the presented thesis work, a Richardson-Lucy approach will be considered since a simulation of the PSF can be performed.

As a final remark, when considering the possible, feasible algorithms for a given deconvolution problem, it must be considered that this choice strongly determines the outcome in terms of SNR, resolution, computational time, and resources needed, making this choice crucial.

1.2 LIGHT SHEET FLUORESCENCE MICROSCOPY

Light Sheet Fluorescence Microscopy (LSFM) is a fluorescence microscopy technique that, since its publication in 2004 [10], has been proven to be a valid tool for a variety of biological studies, form ecotoxicology [11] to developmental biology [12], from single cell specimens [13] to whole organisms [14]. These studies in fact often deal with large light sensitive samples, that need a gentle imaging approach at high resolution which could be easily repeated over time.

This second part of the thesis has the goal of introducing the working principles of LSFM, focusing on its main advantages and drawbacks compared to other commonly used fluorescence microscopy techniques. To this aim, a detailed analysis of its hardware implementation and optical performances are proposed. This section will also be helpful to put the theoretical basis of the developments in the technique which are the topic of this work.

1.2.1 Working Principles

LSFM historically finds its founding concepts in a technique named “ultramicroscopy”, presented by Richard Adolf Zsigmondy and Henry Siedentopf in 1902. In an ultramicroscope, a solution of colloidal gold is illuminated from the side by light directly focused from the sun; the resultant scattering figured is then orthogonally detected. The technique presented in this first section is named after its distinguishing feature, namely the thin plane of light. Such plane of light is used to excite fluorescence emission in a biological sample, which is consequently optically sectioned. For this reason, Light Sheet Fluorescence Microscopy can be referred to also as Selective Plane Illumination Microscopy (SPIM). Once emitted, the signal is collected by an optical detection system which is orthogonal to the incoming light sheet, as in the 1902 ultramicroscope. The mutually orthogonal spatial arrangement of the illumination and detection subsystems is indeed another fingerprint of LSFM. In the considered configuration, the excitation beam is spatially localized to a narrow plane, which is entirely imaged onto the sensor at a given time. Altogether, the excitation confinement and the orthogonal detection path grant intrinsic optical sectioning to the technique, i.e., intrinsic capability of distinguish adjacent planes one from the other. SPIM spatial design is such that illumination and detection systems do not overlap, being one of the main differences with more widespread epifluorescence techniques, confocal or multiphoton microscopes for example.

A sketch of typical LSFM setup is displayed in Figure ii. The easiest way to obtain light focusing over a single line is in fact using a collimator cascaded with a cylindrical lens. At a distance equal to the focal length of the cylindrical lens, it is placed a sample chamber, which usually contains both sample and imaging medium. The illumination light sheet profile is determined by both the collimated beam diameter and the lens optical power and must be designed according to the desired volume of imaging: thicker light sheets are well suited for larger sample, whereas narrower and more diverging light profiles match smaller samples. The fluorescence signal is focused by an objective and a tube lens onto a surface sensor, usually a Charge Coupled Device (CCD), so that the detection optical axis is orthogonal to the incoming excitation beam. To reject scattered photons, a cut band filter is usually placed in between objective and tube lens. The design of a LSFM must be such that the illumination waist coincides with the focus of the objective lens.

For its one-shot acquisition of a whole plane of the sample, LSFM is often used to image a three-dimensional volume and it can be performed in several ways. The simplest way to perform volume scanning is to rigidly move the sample across the light sheet by means of a controlled translation stage: the motion could eventually result in shocking the sample and thus introducing unwanted specimen movement or signal translation. To avoid any possible shock, a gentler approach provides for the motion of the light sheet instead of the sample. This can be obtained by using a galvanometric mirror, a swinging reflective surface, that according to an input voltage shifts plane of illumination and an electrotuneable lens, which accordingly changes its optical power so that the light sheet (i.e., the imaged plane) is always in focus at the detector plane. Said approach has been proposed by [15]. Another possible strategy to obtain motionless volumetric imaging is that of translating the light sheet within an extended Depth Of Field (DOF). Once again, said extension can be performed in a variety of ways, which can involve the presence of a known phase shift in the back focal plane of the detection lens or the introduction of determined optical nonidealities, namely spherical aberrations [16].

Despite being a strong improvement in a LSFM setup, defocus-based methods bring together many disadvantages. This methods in fact have the detection point spread function delocalised along the propagation axis, therefore notably reducing the optical efficiency of the collection. On top of that, a larger extension in the DOF implies a bigger loss of higher spatial frequencies, causing a loss of resolution of the system. Nonetheless, augmenting the volume of imaging through rotating mirrors and DOF extension has been widely used in literature, due to its relatively easy implementation.

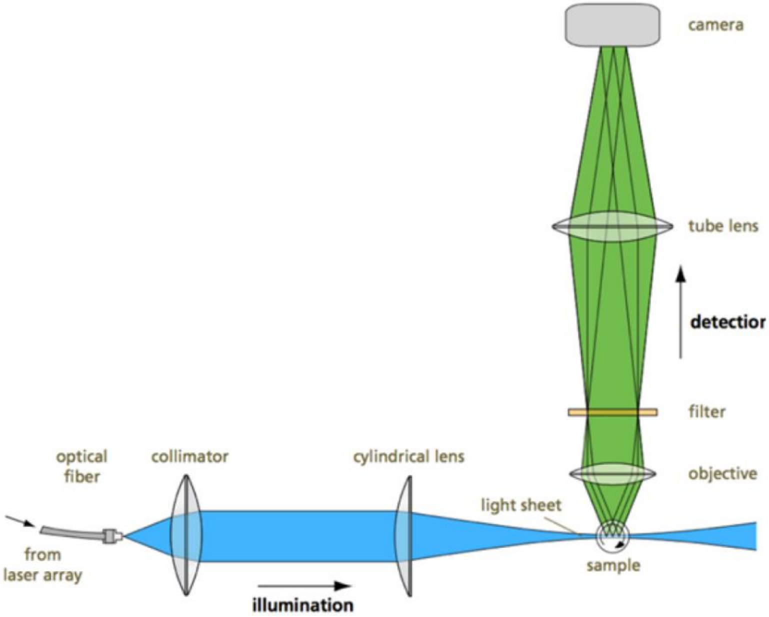

Figure ii: Light sheet fluorescence microscopy optical setup [11].

As introduced in the previous section, the peculiar design of Light Sheet Fluorescence Microscopy is such that a whole plane is illuminated and consequently acquired at a time. This feature, together with intrinsic optical sectioning, enables faster volumetric acquisition of a sample, without notable losses in resolution.

The laser confinement in a narrow plane is one of the major differences with other point scan microscopy techniques, in which the imaging of the sample is obtained by raster scanning the illumination spot over the area of interest, implying a slower acquisition. On top of a faster image acquisition, LSFM also improves the efficiency in the illumination process. In point scanning microscopy in fact, fluorescence signal is excited by a cone of light that non selectively illuminates the sample whilst the one point at the focus of the detection objective is being imaged [17]. This results in an unnecessary illumination of portions of specimen which may end up contributing to background noise or being photobleached, as depicted in Figure . LSFM, by confining light on a plane which is conjugated to that of the surface sensor, efficiently harvest information from the sample, making it a good candidate with respect to point scanning approaches when dealing with *in-vivo*, three dimensional samples.

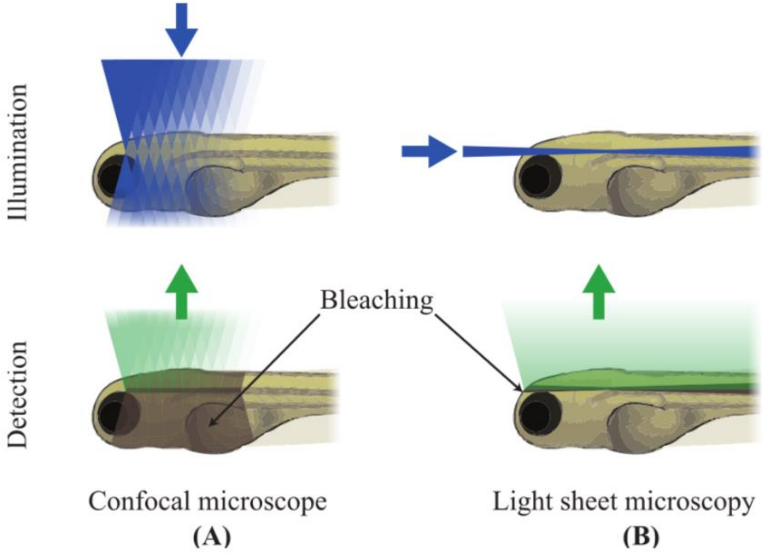

Figure iii: Difference in light focusing in illumination and detection in a confocal microscope(A) and in light sheet microscopy (B) [12].

It has been discussed how the excitation sheet enables an efficient photon harvesting from volume of interest, but how does it affect the optical imaging of said volume? Or better, what are LSFM axial and lateral resolutions? As presented in the first section of this thesis, given the excitation wavelength and the NA of the detection objective, the lateral resolution is easily calculated by equation 1.1. which is rewritten in terms of the minimum resolvable distance $\Delta\rho$ between two ideal points emitters at λ_{em} and a detection lens of NA_{det}:

$$\Delta\rho = \frac{\lambda_{em}}{2 \cdot NA_{det}} \qquad 1.8$$

From Eq. 1.1 it is clear how, to increase resolution, one could think either of reducing the emission wavelength of the markers or increasing the numerical aperture of the objective lens. While working with shorter wavelength fluorophores in biological samples is not always feasible due to autofluorescence or high absorption, it might be convenient to work at higher NA. It is nonetheless true that, by doing so, one would obtain an increased resolution, but it would also cause a reduction in the field of view (FOV) of the system, making it not always convenient to choose higher NA objectives.

Furthermore, whenever acquiring any kind of signal, this must be correctly sampled by the sensor, making it possible to effectively reach Abbe’s limit. CCD sensor are in fact divided in little pixels which, for their limited spatial extension, might end up cutting high spatial frequencies from the incoming scene. This happens when the spatial extension of a single pixel is bigger than that of a point source imaged on said pixel: this would result in an under sampling of the scenery, preserving low frequencies component and rejecting higher frequencies. The correct way to tailor the pixel size according to the wanted lateral resolution is given by the called Shannon-Nyquist theorem which states that, a point emitter must be sampled at least by two pixels or, equivalently, that the sampling frequency must at least double that of the sample; in formula this means:

$$\delta_{pixel} = \frac{\lambda_{em}}{4 \cdot NA_{det}} \qquad 1.9$$

which ensures correct spatial sampling.

The lateral resolution of LSFM quantifies the capability of distinguishing two nearby objects along a plane which is parallel to that of the light sheet, whereas axial resolution marks the same quantity but on an axis parallel to that of the detection and therefore perpendicular to that of the lateral resolution. Considering that a fluorophore emits only if excited and that the axial profile of the light sheet is equal to its thickness, it follows that the minimum axial resolvable distance is this parameter.

As previously said, the easiest way to obtain a light sheet illumination is to focus a collimated laser source with a cylindrical lens whose output is a Gaussian shaped profile, as depicted in Figure iv.

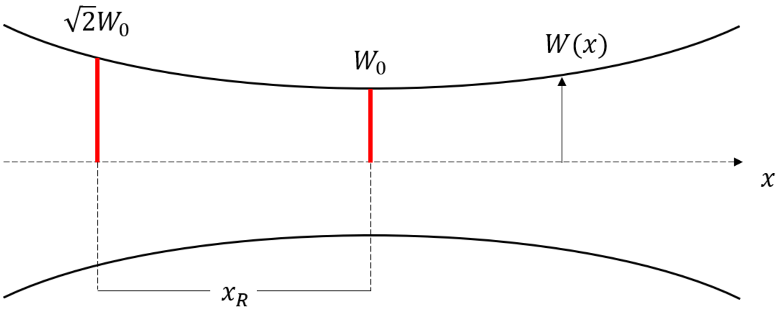

Figure iv: Gaussian beam intensity profile. The Rayleigh length x_R is defined as the distance from the minimum beam waist w_0 for which the beam intensity increases of a factor $\sqrt{2}$.

A Gaussian profile along a direction of propagation x is mathematically described as:

$$w(x) = w_0\sqrt{1+\left(\frac{x}{x_R}\right)^2} \tag{1.10}$$

with w_0 being the beam waist and x_R being the interval in which the beam assumes a dimension which is $\sqrt{2}w_0$ and is called Rayleigh length. It also holds a mathematical relation between the minimum spot size of a Gaussian beam and its persistence length, namely:

$$x_R = \frac{\pi w_0^2}{\lambda} \tag{1.11}$$

Eq. 1.10 and 1.11 highlight the mathematical relation between and x_R: the smaller the beam waist, the faster the divergence of the beam. In other words, if in a light sheet microscope, one wants to obtain high axial resolution, i.e., a small beam waist w_0, a smaller imaging region x_R must be considered.

The beam waist size $w_0$is geometrically determined by the illumination optics, it holds in fact that $w_0 \propto \frac{\lambda}{NA_{ill}}$, from which it can be inferred that $x_R \propto \frac{\lambda}{NA_{ill}^2}$. From these relations, it can be seen how by increasing NA_{ill} , x_R drastically decreases. Said z the axis, which is perpendicular to the sensor plane, in LSFM narrower light sheet profile is along z, meaning that the axial resolution of the system is given by the Gaussian profile beam waist:

$$\Delta z \sim w_0. \tag{1.12}$$

When designing an optical light sheet microscope, the light sheet persistence length must be such to evenly illuminate every region of the imaged plane at a convenient resolution. Furthermore, the light sheet profile must match the sensor dimension so that the wanted axial resolution is obtained all over the Field Of View.

To conclude, LSFM can achieve lateral resolutions that are comparable with those of epifluorescence microscopy, but such performances are obtained with a stronger light confinement which results in a stronger background rejection and a more efficient usage of excitation photons compared to Laser Scanning Confocal Microscopy [18]. Furthermore, LSFM provide a significant improvement in axial resolution and imaging speed if compared to epifluorescence techniques.

Despite being a valid alternative in most *in vivo* experiments, LSFM suffer from intrinsic limitation given by its design. The coherence of incoming light together with the mutual orthogonality between illumination and detection subsystems are such that the final acquired image may present long shadowing artefacts which arise from absorbing and scattering centres on the sample itself. Said artefacts can be easily spot as long dark stripes parallel to the light sheet, similarly to what it can be experienced in everyday life.

In second place, imaging deep inside biological tissues with a limited density of energy might degrade the acquired images quality. These, in fact, are going to show higher signal to noise ratio if taken of a part of the sample facing the detection objective. Conversely, photons coming from the back of the same sample are more likely, due to the longer path in the tissue, to incur into scattering or absorbing event, deteriorating the frame contrast. As well as the fluorescence photons, despite its high degree of the coherence, also the illumination light sheet might be downgraded by imaging part of the sample which are further away from the illumination objective.

Imaging thicker, larger samples without incurring in the presented nonidealities, is the main goal of this thesis work. In the next sections few implemented methods will be described to obtain high resolution volumetric imaging in mesoscopic sized biological samples.

1.2.2 Light Sheet Engineering

A crucial point to consider when designing a Light Sheet Microscope is axial resolution. This in fact is determined by the light sheet thickness. As described in the previous sections, the narrower the illumination beam waist (i.e., the bigger the NA_{ill}), the higher the beam divergence. This trade-off between axial resolution and Field Of View extension puts a strong constraint on LSFM use. However, in literature they have been proposed few methods to achieve higher axial resolution over an increased volume. A possible approach is that of using non-diffractive beam profiles, such as Bessel beams, which have been extensively studied for their longer persistence length and self-healing properties [19].

Having an intensity profile as that of the homonym function, Bessel beams critically suffer from the presence of significant side lobes, which altogether worsen the sectioning capability, the image contrast and unnecessary light damage induced to the sample which may result in further, unwanted external stimuli or photobleaching. Again, it is easy to find in literature a way to overcome said drawbacks: from side lobes suppression through different beams superposition [20] to parallel multiphoton illumination [10]. In this last approach, the use of multiple Bessel beams prevents the sample from being illuminated by high intensity fields, which are typical of multiphoton strategies. Finally, a remark is made on Airy beams, which outperform Gaussian beams in terms of persistence length and resiliency to perturbation. Airy beams, despite being easily implemented, nonetheless imply a big effort in data reconstruction [21].

A further paragraph is dedicated to super resolved Light Sheet Microscopes, in which a sub diffraction excitation light sheet is produced in a way that mimics Stimulated Emission

Depletion microscopy (STED). In this technique, an initial laser pulse depletes by stimulated emission (SE) all the fluorescent states of molecules located in the excitation focal plane, except for a central point, resulting in a torus shaped region. Thus, the central spot is photo-activable by a second laser pulse. The dark state saturation of molecules gives rise to a strongly non-linear response which leads the formation of an emitting region engineered to be smaller than Abbe's limit. Analogously to STED, Light Sheet Fluorescence Microscopy has been also proven to bypass the diffraction limit. In this context, the number of axis along which super resolution is achievable is given by the number of light sheets simultaneously shining the sample [22]. Despite being relatively similar in terms of working principle, STED and super resolved LSFM strongly differ when considering the involved energy density: the latter in fact needs a lower photon density. Lower energies result in a slower molecule switch time, which is best suited for *in vivo* experiments. Furthermore, super-resolved LSFM has achieved a 60% enhancement in axial resolution, compared to its diffraction limited counterpart [23].

To this point, they have only been considered those methods which extend the region of best axial resolution through light shaping. however, it is also possible to increase the light sheet persistence length by, for example, changing the optical power of an electrotuneable lens [24] or synchronizing the translation of the illumination optics with the line acquisition of the camera [25]. This dynamic use of light focusing is such to output a light profile which is effectively narrower over a longer distance, without inducing side lobes or further unwanted effects.

1.3 SELECTIVE VOLUME ILLUMINATION MICROSCOPY

Despite the major advantages discussed in the previous section, LSFM is not the best solution when fast imaging over a large volume is needed. In many cases, it is fundamental to be able to follow at high resolution, fast dynamics over a large area: in these situations, a thin light sheet might not be enough. To this extent, Selective Volume Illumination Microscopy (SVIM) is a possible alternative to Light Sheet Fluorescence Microscopy. Firstly, the two techniques are both characterised by detection and illumination path mutually orthogonal, giving an intrinsic optical sectioning and a faster acquisition with respect to raster scan approaches.

Furthermore, in SVIM, the sample is illuminated by an axial profile that lies in a confined volume, so that every acquired image is given by a weighted sum of the incoming fluorescence contribution from the different modulated planes. After the raw data acquisition, a 3D reconstruction of the imaged volume can be obtained. SVIM has been proven to further increase the acquisition rate, without loss in resolution, when compared to other microscopy techniques [26]. On top of this, the excitation profile can be modulated according to the sample spatial features, without losing sectioning. Structured volume illumination has been demonstrated to be less phototoxic and, to equivalently obtain single plane volumetric reconstruction [24].

1.3.1 The Technique

LSFM, by single plane illumination, directly images light coming from that plane onto the sensor, yielding a sectioned volume acquisition without the need for reconstructions. Having the volume sequentially sampled by a scanning light sheet or by a moving stage implies that the different parts of the specimen are acquired at different times. Moreover, the time taken for a whole scan is longer than the time scale of many biological phenomena of interest, resulting in a loss of information or, at best, in a distorted acquisition. From here it is clear how the need for simultaneous 3D acquisition techniques has arisen.

A possible answer to this troublesome demand is depicted in Figure v, where it is shown the working principle of Light Field Microscopy (LFM). In this technique, volumetric information is simultaneously acquired by shifting the image plane onto a micro-lens array, which operates differently on light coming from different depth of the sample. Once a 2D, depth encoded light field is acquired by a standard CCD camera, the original signal distribution is recovered after solving a fully determined inverse problem [27].

Being directly derived from wide field microscopy, LFM shares its main drawback: namely unnecessarily exposing part of the sample which are not imaged yields a weak rejection to out-of-focus background signal.

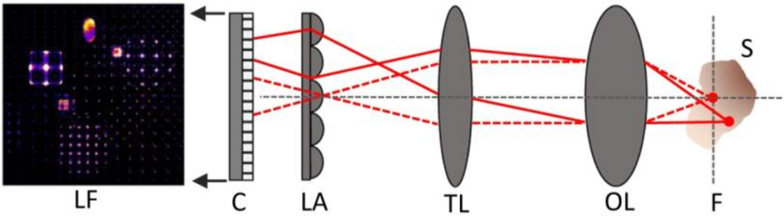

Figure v: Typical setup of Light Field Microscopy: a magnified image of the sample (S) from the focal plane (F) to the image plane (IP) using an objective lens (OL,) and tube lens (TL). In the image plane is placed a micro-lens array (LA), encoding 3D image information into a 2D light-field image (LF), which is captured by a planar detection camera (C) [26].

Analogously to what previously described for point scanning epifluorescence techniques, a possible way for reducing photodamage and efficiently harvest incoming fluorescence is that of illuminating orthogonally with respect to the sensor plane. The analogy in the approach, together with the presented benefits, grants SVIM a higher noise rejection, higher contrast, and intrinsic faster acquisition.

In the presented work, it is presented a technique which is similar to SVIM, but it is not aimed at synchronous acquisition of a whole volume. It is instead implemented so to exploit structured illumination. Such technique takes advantage from a set of different modulated illumination patterns to formulate an inverse imaging problem which enables optically sectioned reconstructions from non-sectioned acquisition. Furthermore, in the next sections it will be introduced a signal processing technique which can lower the amount of data needed for a lossless volumetric reconstruction, intrinsically reducing the light dose shining the sample. Lastly, the imaging approach discussed sets its capability of optically sectioning the sample by acquiring patterns with increasing spatial frequencies, resulting in an overall axial resolution inevitably limited by the maximum acquired spatial frequency.

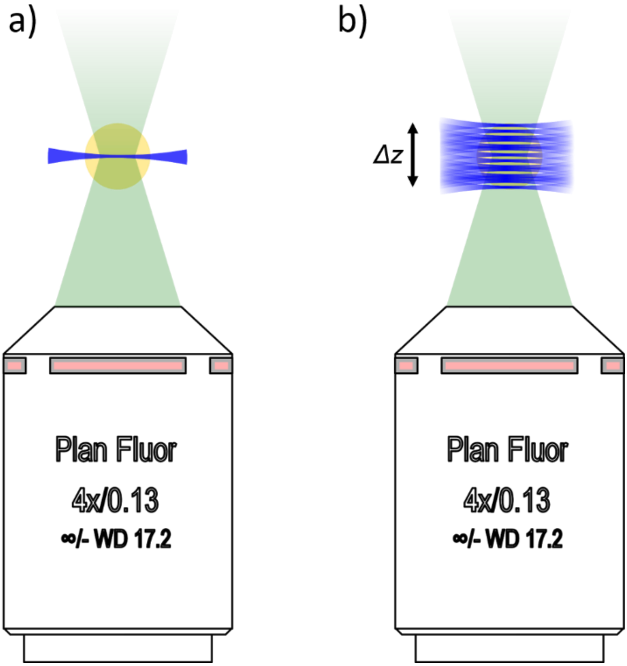

Figure vi: Schematic representation of the main operating difference between LSFM (a) and SVIM(b) [28].

The core of the idea is shown in Figure vi: instead of confining incoming excitation light only in a single plane as in LSFM, in SVIM a surface sensor acquires information coming from different planes at a given frame. Different depths are encoded in different frames in LSFM, while this is not true in SVIM. Here in fact the spatial distribution of the sample is reconstructed by mixing depth and time information during the acquisition. Such modulation has been proven to both increase axial [29] and lateral resolution [30]. Within the presented context, many possible modulation patterns have been proposed, each of which with its own pros and cons: this will be disserted in the next section together with their hardware implementation.

As presented for the first time by Truong et al. in [26], Selective Volume Illumination Microscopy finds its strength in its speed, which is twice as faster as that achieved by a custom LSFM setup, on a given $100\ \mu m$ sample volume. The improvement in speed however comes at a cost which is lower axial resolution compared to LSFM.

Even if the axial resolution can be greatly increased by reducing the volume of interest, as displayed in Figure vii, still SVIM is no match compared to LSFM; nonetheless selective illumination grants higher contrast and stronger resiliency to out of focus signal than those provided by LFM.

Despite being a valuable alternative for fast 4D imaging *in vivo,* SVIM is also well suited for further implementation which may take advantage for the custom spatial modulation obtained at the sample plane. As described in detail in the next section, said feature opens to a numbers of possible reconstruction protocols which can lead the acquisition to be even more compatible to photo sensible samples.

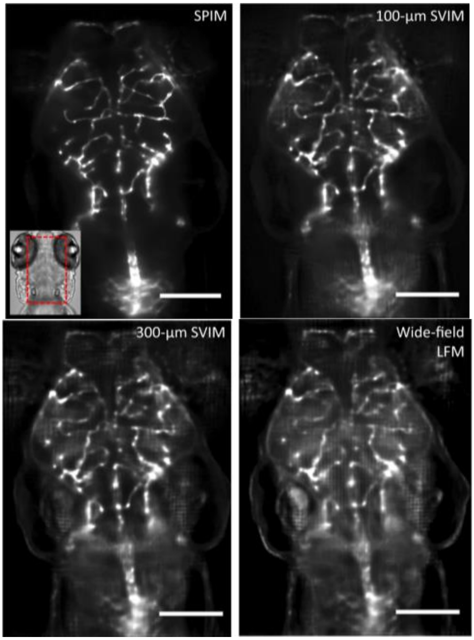

Figure vii: Qualitative comparison of the results obtained when imaging the head of a zebrafish with SPIM, SVIM with increasing volume thickness and LFM showing the degrading of the resolution and the increasing of the out-of-focus background [24].

1.4 THEORY OF COMPRESSING SENSING

In many fields, the concept of signal acquisition is often coupled with that of compression. For example, by acquiring an image with a cell phone camera, what is stored is a matrix of raw data, whose values correspond to those acquired by the sensor pixels. Such matrix might show up to millions of values, according to the characteristics of the sensor used and it might take megabytes of memory to store it. When storage is a scarce resource and it is limited, compression might come to help. The aim of compression in fact is that of reducing the number of resources needed to store information, without, ideally, losing any piece of it. Since 1992, with it was first published, one of the most widespread compression algorithms is the JPG or JPEG, in which an image is transformed by a Discrete Cosine Transform (DCT) or wavelet transform, and then is stored by discarding the non-zero coefficient, which do not carry information in the transformed domain.

In this sense, Compressed Sensing (CS) further generalises the concept of mathematical compression of a discretized sampled signal. CS aims at seizing only those pieces of signal which carry valuable information, by limiting the number of acquisitions involved in the process. Due to its general mathematical basis, CS has found applications in the years in many scientific and commercial fields such as x-ray computed tomography [31], magnetic resonance imaging [32], [33], THz spectroscopy [34], [35], electron microscopy [36], [37], radar imaging [38] and astronomy [39].

Each of said fields of application, has its own acquisition strategy, and their benefits from a compressed sampling strategy may vary with it. In fluorescence microscopy, a reduced number of measurements leads to a lower number of photons shining the sample, implying a major advantage when dealing with living, biological specimens. Along with photobleaching mechanism of fluorescent molecules and tissue damage, in developmental studies it is also crucial not to induce any photo-related shock to the sample [40]. To this extent, many works have been published on the use of CS to speed the acquisition up at a fixed SNR, and therefore increasing the temporal resolution of a fluorescent microscopy technique, making it a good candidate for 4D imaging as in the case of interest for developmental studies. As a final remark, CS has been reported to improve fluorescence lifetime and hyperspectral imaging.

For the sake of completeness, in this section it will be given an overview of the theoretical principles beyond Compressive Sensing and it will also be discussed how it might be implemented in different experimental conditions, with regards to one of its most known application: Single Pixel Camera (SPC). Nonetheless, in the next sections it will be described how CS was implemented in this thesis work, putting together ideas from different techniques.

1.4.1 Ill-posed problems

In the condition in which it is wanted to sample a quantity $\boldsymbol{\chi} \in \mathbb{R}^n$ through a measurement routine, this can be represented as a matrix $\Phi \in \mathbb{R}^{m \times n}$. The vector $\boldsymbol{\chi}$ might be intended as any signal, and in the latter, it will be referred to as an image vector, but for the moment it will be considered as a generic vector made by n components χ_i.

The matrix Φ represents the sampling process in the sense that any of its row vectors $\boldsymbol{\phi}_j \in \mathbb{R}^n$ represents a measurement in that given base. Conversely, the column vectors contain the encoding rule with which the information enclosed in $\boldsymbol{\chi}$ are translated in what is measured, namely the vector $\boldsymbol{\xi} \in \mathbb{R}^m$. Formally, the scalar product between the sampling vector $\boldsymbol{\phi}_j$ and the unknown signal $\boldsymbol{\chi}$ is equal to the measured j^{th} entry of the vector y:

$$\xi_j = \boldsymbol{\phi}_j \cdot \boldsymbol{\chi} = \sum_{i=1}^{n} \phi_{ij} \chi_i \qquad j = 1, \dots, m \qquad 1.13$$

In this form, Eq. 1.13 can be recast as $\boldsymbol{\xi} = \Phi\boldsymbol{\chi}$, which is a linear equation that considers all the m measurements. If the sampling matrix Φ is of the highest rank, namely it is made by linearly independent vectors (which therefore constitute an orthonormal basis of the sampling space) and the number of measurements m equals the number of components of the unknown signal vector $\boldsymbol{\chi}$, i.e., $m = n$, the problem $\boldsymbol{\xi} = \Phi\boldsymbol{\chi}$ is said to be fully determined and has only one unique solution. Said condition is named well-posedness. Experimentally, this condition is almost never achievable, since not every component of the signal $\boldsymbol{\chi}$ might be measurable due to noise or inaccuracies, or simply by experimental signal fluctuations.

Let it now be considered the case in which, differently from Eq. 1.13, an unknown, general noise term η is perturbing the experimental system. In this condition, the linear sampling problem shows an additive noise term $\boldsymbol{\xi} = \Phi\boldsymbol{\chi} + \eta$. If for example the noise term is such that $\eta \sim 0$, then, for continuity this also means $||\boldsymbol{\xi} - \Phi\boldsymbol{\chi}|| \sim 0$, meaning that in small noise regime, the distance between the measured vector $\boldsymbol{\xi}$ and the model $\Phi\boldsymbol{\chi}$ tends to be small. In practice, with the term “distance” it is meant the Euclidean distance, namely the l_2-norm, so that finally the wanted unknown signal $\boldsymbol{\chi}$ will such to optimize the following:

$$\min\left(\sum_{j=1}^{m}\left|\xi_j - (\Phi\boldsymbol{\chi})_j\right|^2\right) \quad \text{or} \quad \min\left(\|\boldsymbol{\xi} - \Phi\boldsymbol{\chi}\|_{l_2}^2\right). \qquad 1.14$$

A generic l_p-norm is defined by $\left(\sum|\chi_i|^p\right)^{1/p}$, hence easily giving meaning to the case $p = 2$, which was previously cited.

Having a well-posed problem simplistically means that to each unknown parameter corresponds a sampled value. Together with this correct sampling situation, it might occur to have either an over sampled or an under sampled problem which is also called ill-posed (Figure viii).

Undersampled problems will be largely presented in the next sections due to their importance in the CS theoretical framework. As a matter of completeness, oversampling an unknown signal $\boldsymbol{\chi}$ (meaning that more measurements are taken with respect to the signal parameters) could be of help when dealing non-idealities, i.e., putting more constraints to the linear problem $\boldsymbol{\xi} = \Phi\boldsymbol{\chi} + \eta$ than needed. However, despite mathematically speaking there is no downside in solving an oversampled problem, in a real-world scenario this might imply an overexposure of the sample to light as well as other unwanted situations. Thus, one might be willing to undersample an unknown signal more than oversampling it. That is the reason why here it is discussed the case in which $\boldsymbol{\chi}$ is sampled by an under-dimensioned measurement routine (i.e., $m < n$). It will also be discussed how and in what conditions the undersampled vector can be reconstructed and the entity of the reconstruction error.

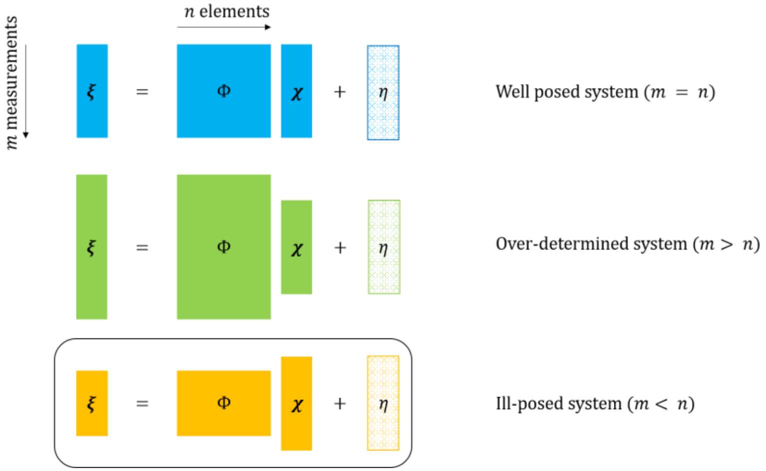

Figure viii: Schematics for a determined, over-determined and ill-posed problem.

1.4.2 Regularisation

Solving a linear problem with fewer constraints than those needed means that there is no mathematical guarantee about neither the existence nor about the uniqueness of the solution. A common strategy to overcome these problems is enforcing further constraints on the solution itself; for example, by assuming it to be of some analytical form or subject to a priori information. These assumptions result in a process called solution regularization. For the intrinsic nature of the problem, there is no such regularisation method that can be blindly applied to any problem. In the following, they will be briefly discussed the two most important regularisation strategies.

A possible approach when optimizing the residual of a least square term may be to enforce it to behave in a particular way: among many possible choices, it can be chosen that solution x so that its Euclidean norm is minimized, namely $\sum\|\chi_i\|^2 \equiv \|\boldsymbol{\chi}\|_{l_2}$. Said condition can be analytically constrained by adding a penalty term to Eq. 1.14:

$$\min\left(\|\boldsymbol{\xi} - \Phi\boldsymbol{\chi}\|_{l_2}^2 + \lambda\|\boldsymbol{\chi}\|_{l_2}^2\right), \qquad 1.15$$

where, λ is a tuneable parameter which can strengthen or weaken the regularisation effect, for example by reducing the formulation to a least-square minimisation if $\lambda = 0$. This approach, for historical reasons, has been given different names, among which the most widely used are Tikhonov regularization, ridge or l_2-norm regression.

In Eq. 1.15, both the data fidelity and the regularizer term are expressed as l_2-norms. Computationally speaking, this norm is calculated after a matrix inversion, which is also performed with means of optimisation algorithms, making this choice inconvenient. Linear least-square problems belong to the category of convex problems, i.e., those problems in which a local optimum is also a global optimum. This also holds for their l_2- and l_1-regularized formulations. Moreover, it can be shown that the l_1-norm, defined as $\sum\|\chi_i\| \equiv \|\boldsymbol{\chi}\|_{l_1}$, is the smallest order norm that implies convexity of the problem [41]. One may wonder what would happen then by replacing the l_2 with another convex norm, namely the l_1-norm in Eq. 1.15. This replacement would be formulated as:

$$\min\left(\|\boldsymbol{\xi} - \Phi\boldsymbol{\chi}\|_{l_2}^2 + \lambda\|\boldsymbol{\chi}\|_{l_1}\right). \qquad 1.16$$

Using as regularizer a norm which is the sum of absolute values is such that there is no closed-form solution to Eq. 1.16. Hence, to solve a l_1-regularized linear problem, one can follow many different computational approaches, out of this thesis reach, such as gradient-descent [42] or conjugate-gradient [43] methods.

A remarkable outcome of using l_1-norm is that the so obtained solution will be $\boldsymbol{\chi}$ which shows the smallest sum of its components χ_i absolute values. This last behaviour can be demonstrated to imply maximum sparsity of $\boldsymbol{\chi}$. In other words, a sum of absolute values regularizer enforces the solution to have only a few of its entries non-zero, thus selecting n_s components and dropping the remaining $n - n_s$. In literature, the l_1-norm is also known as lasso-regularization ("least absolute shrinkage and selection operator") or basis pursuit [44] [45]. Its convex formulation, due to its link to vector sparsity, has strongly encouraged signal compression strategies as Compressive Sensing.

As a final remark, the ideal regularisation to enforce sparsity, i.e., compressibility in the solution would be that regularisation which minimizes the number of non- zero parameters of the solution vector, which is mathematically expressed as $\sum\|\chi_i\|^0 \equiv \|\boldsymbol{\chi}\|_{l_0}$. By considering this regularisation term, together with the same data fidelity term based on the Euclidean distance between $\boldsymbol{\xi}$ and $\Phi\boldsymbol{\chi}$, the problem would be recast as:

$$\min\left(\|\boldsymbol{\xi} - \Phi\boldsymbol{\chi}\|_{l_2}^2 + \|\boldsymbol{\chi}\|_{l_0}\right). \qquad 1.17$$

As anticipated however, the smallest norm to show convexity of the solution is l_1 , meaning that l_0 -regularization would not grant for a global solution. Technically, l_0 is not even a norm since it lacks homogeneity. Nonetheless, the solution obtained after solving a signal recovery problem in the form as Eq. 1.16, i.e., with a l_1-regularizer, can be considered formally equivalent to those in principle obtainable with Eq. 1.17 [46]. From this section on, due to its easier formalism, a l_1 regularisation term will be considered, if not specified differently.

1.4.3 Sparsity, compressibility, and incoherence

As highlighted in the previous section, l_1-norm has been intensively studied for its capability of enforcing sparsity in the solution of an underdetermined problem. A signal is said to be sparse in a specified representation basis if its discretized form only shows few non-zero coefficients. However, in signal compression, there could be some threshold value below which a particular coefficient can be neglected, therefore introducing a loss, although small, of information. From what said, a signal can be compressed only if some of its parameters are needed for an accurate reconstruction. This means that, considering a linear map W which represents the unknown signal $\boldsymbol{\chi}$ in a new basis, as $\boldsymbol{\chi} = \mathrm{W}\boldsymbol{\psi}$, the curve of sorted coefficient of $\boldsymbol{\psi}$ decays rapidly

[47]. Trivially, a different transformation rule determines different degree of sparsity of the represented signal $\boldsymbol{\psi}$.

To this extent, a good representation basis to enforce sparsity in real world image has been of strong interest in the field of image processing: from this interest, the so called wavelet basis is an established standard in compression allowing the patent of JPEG-2000 algorithm [48]. JPEG, involving a discard in information, is a lossy reconstruction algorithm.

To this point, there has not been any distinction between compression and compressed reconstruction, but the two signal processing strategies differ. The first case holds when the signal of whatever nature is known, and one wants it to be encoded in the smallest amount of data $\boldsymbol{\psi}$. Conversely, the latter situation holds when an underdetermined set of sampled values is the starting point, and what is wanted is the unknown object of which the measurement has been taken. Hence, the signal is restored after taking less measurement than those needed in classic signal recovery procedures: this is Compressed Sensing.

Let it be considered for the sake of simplicity the situation in which the starting dataset is a picture taken of a night sky. Here, the signal of interest is the star distribution. Of course, the pointy light sources are well separated and can be easily acquired by the many pixels of the camera sensor. In this scenario, the signal is already sparse in its former space, there is no need to represent it through a transform matrix W, as depicted in Figure ix. W would be ideally an identity matrix I (or, more accurately identity matrix convolved with the PSF of the imaging system). Nonetheless, many natural

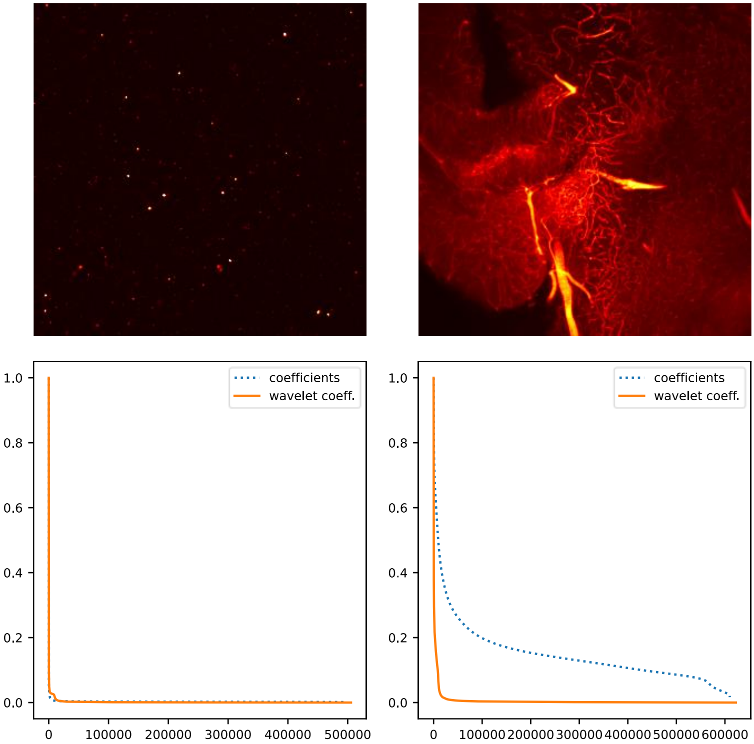

Figure ix: Image of a spatially sparse object (a) and corresponding coefficients in the real and wavelet space (b). Image of an object sparse in the wavelet space but not in the real space (c) and corresponding coefficients (d). Few wavelet coefficients are sufficient.

images if expanded in an appropriate basis (as wavelet basis in Figure ix) translates the problem of sparse signal recovery in another domain.

Compressed Sensing aims recovering the signal of interest $\boldsymbol{\chi}$ (or its sparse representation $\boldsymbol{\psi}$ if needed) from a limited number of samples. To this goal, the measurement matrix Φ has to be design so to show maximum incoherence with the signal representation system [47]. Incoherent sampling means that all the fundamental features are seized with the minimum number of acquisitions, thus implying that each measurement vector in Φ should be completely uncorrelated to those of W [49]. Along with wavelets, many other transforms have been tested for image reconstruction, the most remarkable of which will be discussed in detail in the following sections. As a final remark, the best way to incoherently sense the image shown in Figure ix b) would be that of using wavelets dual transform, which is named noiselet transform [50].

1.4.4 Solution of inverse problems with CS

Compressive Sensing usually recovers the solution of ill-posed linear problems, with l_1-regularization terms, in the form of a sparse solution. Or rephrased, CS is capable of reconstructing $m/\log n$ coefficients of a signal of n parameters from m measurements [51]. One of the main ingredients of the CS recipe is the sparsity of the involved vectors, since the found solution is the sparsest of those mathematically correct. As previously highlighted, to obtain a faithful recovered signal with the highest fidelity it is needed an incoherent measuring matrix. However, since the rank of the sampling matrix is lower than the number of parameters of the unknown signal, it is very unlikely to use a complete orthonormal sensing set. To help in the search of a sparse representation, CS uses l_1-norm regularization which performs intrinsic feature selection, selecting only few non-zero entries.

Finally altogether with sparsity, incoherent sampling and the correct regularization form a powerful set of tools to outperform the classic Nyquist-Shannon theorem [52]. For said reason, CS opened the way to a variety of applications, with remarkable results in the field of image processing.

1.5 IMPLEMENTATION OF COMPRESSED SENSING IN OPTICAL IMAGING

1.5.1 Compressed Sensing in imaging

Compressed Sensing finds application in many research fields such as signal processing, information theory, computational statistics, and imaging. Let it be considered the case in which the unknown sampled signal χ can be recast as 2D or 3D matrix. According to the notation introduced in the previous section, when considering imaging applications, N is the number of coefficients in which the object plane is discretized, while M counts the number of taken measurements. In the case of an ideal optical system used for imaging, $M = N$ hence is the number of pixels of the sensor. Ideally, the so determined measurement matrix Φ will faithfully reproduce the sampled object χ at the sensor plane, thus will be represented as an identity matrix I of rank N, yielding a one-to-one correspondence of each point at the object and at the image plane. However, this holds only in the case of an ideal imaging system. In the case of a real system, characterised by a well specific Point Spread Function, the overall sampling matrix Φ would be given by the convolution of the identity matrix with said function in a matrix form. A powerful tool to reject these non idealities induced by the limited frequency acceptance of a real system is image deconvolution: to this extent l_1 regularisation has been extensively used as shown in [53].

Nonetheless, when some information is known about the object, Compressed Sensing is used, to reconstruct the N pixels from $M < N$ measurements. A possible, useful *a priori* information could be that of spatial sparsity of the object, as in the case of single pointy emitters [54] (for example single molecules), and nanomaterials imaging [55][56]. It also might be the case for spatial and temporal sparsity, as it holds for neural activity recording [57]; sparsity only in a frequency domain, as in fluorescence or Raman spectroscopy [58],[59],[60].

They have been proposed many experimental setups through the years, an overview of compressed architecture is proposed in [61]. In this context, one of most successful architecture is that of single pixel camera [62], that for its importance in this thesis work, will be discussed in detail in the next section.

1.5.2 The single pixel camera

Imaging in the visible spectral range is usually performed using CCD or CMOS sensors. These detectors, made by millions of elements, come in different shapes and features, making them a valuable solution for visible range imaging applications. Due to their spectral response, imaging outside of said region is usually too expensive to be achieved in many conditions. Surface sensor outside of the visible range are orders of magnitude more expensive than commonly used CCD or CMOS cameras. When the cost per pixel is the limiting factor, a possible way to overcome this issue is that of critically diminish the number of active elements involved. The strongest option in this sense is that given by the Single Pixel Camera [62]-[63] (SPC), that, being a cheap alternative, altogether offers other different advantages. SPC architecture flexibility makes it a suitable candidate for many imaging applications, from fluorescence microscopy, multispectral and hyperspectral [64], polarimetric [65], terahertz [34], and ultrafast imaging [66].

SPC is also referred to as optical calculator as it measures the inner product between the object spatial feature and the used test functions instead of just measuring the incoming signal. The inner product operation can be mainly obtained in two ways: in the first, light is projected on the sample, which then emits, the incoming signal is spatio-temporally modulated by a programmable element, set to mimic a predetermined test function, so that the single element integrates the collected light, as shown in Figure x a); conversely a second option is that of modulating light before it reaches the sample as in Figure x b). In both ways, a set of

m masks is sequentially acquired an n discretized vector $\boldsymbol{\chi}$, outputs a vector made by its projection on the used test functions ϕ_m, that is $\xi[m] = \langle \boldsymbol{\chi}, \phi_m \rangle$. This architecture is mostly achieved thank to Spatial Light Modulators (SLM), that selectively modulate light on a plane (which might be in the illumination or in the detection path). However, spatial modulation can be also obtained by having different light sources as an array of Light Emitting Diodes (LED) [67], that can be similarly modulated to generate the needed binary mask.

For the sake of completeness, a Spatial Light Modulator is a device which can, according to its technology, modulate light intensity and/or its phase. These devices can work both in reflectance and in transmittance. The wide range of use of SLM have helped in the research and in the diffusion of Compressed Sensing. Among the many technologies available, one of the most used is Digital Micromirror Device (DMD), a matrix shaped mirror in which any matrix element is a singularly addressable micromirror, which can be tilted along its diagonal. The micromirrors can be programmed to sit in two states namely “on” and “off”, shaping the reflected light according to the programmed pattern. Together with the intuitive binary modulation provided, DMDs can also be programmed to encode light in different grey levels, which are obtained by letting the micromirrors oscillate back and forth over an acquisition cycle. The angular swing of the micrometric mirrors depends on the product, but it is usually smaller than -24 and +24 degrees. As previously specified, SLM can be either placed in the illumination or in the detection path, in a plane which is optically conjugated with that of the sample.

In a Single Pixel acquisition schema, the only active element acquires in sequence m frames which univocally correspond to m patterns.

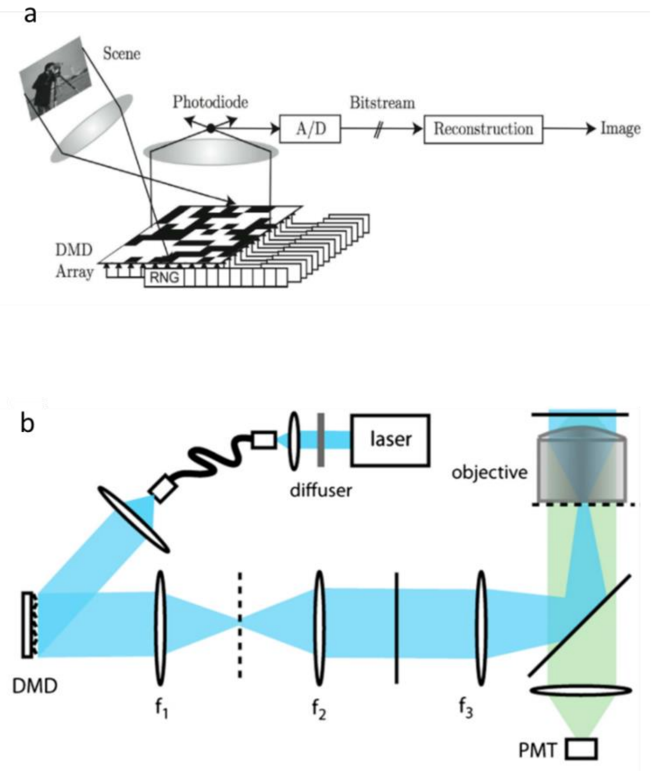

Figure x: Compressive imaging with a single pixel camera (a). Single pixel camera applied to fluorescence microscopy (b). Figures adapted from [67] and [62].

In a compressed context, $m < n$, i.e., the number of pixels of the SLM. The higher the incoherence of the sampling matrix rows ϕ_m with the object $\boldsymbol{\chi}$, the fewer the number of measurements.

As formalised in the previous introductory section, once the measurement vector $\boldsymbol{\xi}$ is obtained, an equation formally equivalent to Eq. 1.16 is optimized and a possible reconstruction of $\boldsymbol{\chi}$ is obtained. From the computational point of view, despite the compressed measurement routine intrinsically takes less time, the computational resources needed for the algorithm to properly converge might be such that the reconstruction overhead largely exceeds the frame acquisition time. On top of this, the time for the inversion strongly depends on the family of the optimisation algorithms implemented. Among them, the most frequently used are l_1 -norm minimisation [68], total variation or gradient projection methods [69], [70].

At this point, only one ingredient is missing in a Compressed Sensing strategy: the sensing matrix ϕ. A possible answer to what matrix should be used, without any tailoring procedure, is that of using random sensing basis. Anyway, despite random patterns well perform in most real-world scenes, compressibility can be greatly increased by using a different measurement matrix. The most used matrices belong to Hadamard, Wavelet, Fourier function sets.

A final remark is needed for tailored sensing approach, in which the sensing basis is not chosen *a priori*, but dynamically, as the experiments proceeds. Along with deep learning strategies [71], in literature they have been published work in which a measurement matrix was tailored to seize features similar to those in the adjacent frame [72], in which 2D VIS information from a coupled CCD device were used to have further spatial information [73] or articles in which low resolution measurements are exploited to predict parts of the field of view where higher spatial sampling is needed [74] [75].

1.5.3 Selection of the patterns

Spatial Light Modulators are capable of encoding information in a single, detectable point in space. These modulators are available to work both in reflection, as DMDs, and in transmission. Modulators that work in transmission are often limited by low efficiency, hence DMDs has been widely used as programmable reflective masks. The possibility of reproducing at the device plane any wanted pattern (also nonbinary, thanks to dithering), widens the choice of the usable sensing matrices.

A non-tailored solution could be that of using random sensing matrices, which show an high degree of incoherence with most natural signal representation basis. For their intrinsic behaviour, random sensing basis have been used in literature to mimic speckle pattern originated in turbid media [76], even though their strong correlation with random noise asks for a larger number of samples at a constant SNR [77]. A possible approach to tackle this problem could be that of performing differential measurements, in which a pattern and its logic negation are acquired. Nonetheless said solution would come at cost of either doubling the detection path, for a simultaneous acquisition, or to double the acquisition time, for a sequential acquisition.

Together with random basis, a suitable set of sensing basis could be Hadamard’s. This family of functions are in fact are easily programmable on a Spatial Light Modulator, since they only show binary entries, thus avoiding any decrease in contrast given by the dithering working mode. As widely discussed in [62], this family of functions can be recursively defined by:

$$H_n = \frac{1}{\sqrt{2}} \begin{bmatrix} H_{n-1} & H_{n-1} \\ H_{n-1} & -H_{n-1} \end{bmatrix} \qquad 1.18$$

Where H_0 = 1. Any Hadamard matrix only shows +1 or -1 entries, which can be programmed to correspond to the SLM “on” and “off” states. DMDs in fact are not capable of displaying negative values pixels, which must be encoded differently. A possible solution is to perform a differential measurement. Here, a single matrix is represented as the subtraction of two sub patterns, one which has only the positive entries, the other with the negatives. A second feasible approach is instead that of only acquiring positive valued Hadamard matrices and then to rescale the acquired pixel value according to a non-selectively illuminated acquisition i.e., by continuous illumination [78]. Nonetheless, what has been written about the differential acquisition in random sensing matrices holds also for differential Hadamard measurements [79]. Furthermore, for

Hadamard basis it holds an interesting property, in fact, for any n dimensional element of this set it is true that $H_n H_n^T = n\, I_n$, which implies no need for matrix inversion. On top of that, the heavy computational effort needed for dense matrix-vector product can be overcome by using the fast Walsh-Hadamard transform, whose computational complexity is of $nlog(n)$, instead of $O(n^2)$ [80]. Despite their mathematical properties and their easy implementation in pixelated, binary masks, Hadamard matrices might not be the best choice as they need large memory storage due to their non-sparse representation [81].

Differently from the other families of test functions presented to this point, Fourier patterns do not show binary entries, so that for their correct encoding on a two-state modulating device, dithering of the pixels is needed. Nonetheless Fourier patterns have been proven to be useful both in Single Pixel Imaging [82] and in imaging beyond diffraction limit [83], [84].

A n-dimensional Fourier complete set has a generic basis element formulated as $\psi_j(t) = \sqrt{n} e^{\frac{i2\pi jt}{n}}$ and is represented by:

$$\Psi_n = \frac{1}{\sqrt{n}} \begin{bmatrix} 1 & 1 & 1 & \cdots & 1 \\ 1 & e^{\frac{i2\pi jt}{n}} & e^{\frac{i4\pi jt}{n}} & \cdots & e^{\frac{i2\pi jt(n-1)}{n}} \\ 1 & e^{\frac{i4\pi jt}{n}} & e^{\frac{i8\pi jt}{n}} & \cdots & \vdots \\ \vdots & \vdots & \vdots & \ddots & \vdots \\ 1 & e^{\frac{i2\pi jt(n-1)}{n}} & e^{\frac{i4\pi jt(n-1)}{n}} & \cdots & e^{\frac{i2\pi jt(n-1)^2}{n}} \end{bmatrix}. \quad 1.19$$

An exhaustive comparison between Hadamard and Fourier sensing matrices is provided [85]. Here it is proven how, despite better concentrating energy, a Fourier measurement basis provides worse noise robustness. Hence, in single pixel imaging, since the light budget is a critical issue, Fourier matrices must be preferred; conversely, Hadamard's are more appropriate for imaging conditions that ask for an overall good quality.

Together with said pre-determined models, more sophisticated, dynamic approaches have been studied. Some strategies in fact, involve an adaptive change in the measurement mask, which tailors the scenery to best seize its features or to change patterns resolution [86], [88] or the pattern sequence is modified on fly according to the information carried in the low frequency patterns.

1.6 APPLICATIONS OF COMPRESSED SENSING

For its general application scheme, Compressive Sensing finds uncountable applications in many fields of signal acquisition. In this section, some of these applications will be briefly reviewed.

Starting from the smallest imageable samples, spatially separated fluorescence molecules can be distinguished at higher resolution compared to that given by the imaging system diffraction limit; in the case of sparse point emitters, for its formulation, CS has been successfully exploited to reconstruct their spatial distribution [89].

Super resolved imaging has found different implementations, most of which imply the stochastic activation of the emitting fluorophores. Among them, Photo-activated localization microscopy (PALM) [90] and Stochastic Optical Reconstruction Microscopy (STORM) [91] have been widely used on spatially sparse samples, therefore which are suitable for compressed imaging. To this extent STORM has been used paired with CS, obtaining faster under-sampled localisation routines [55]-[92]-[93]. In sub-diffraction microscopy, CS has been also successfully applied to frequency domain, it has been demonstrated in fact that compressed strategies can reconstruct a volume 3 orders of magnitude faster than spatial CS-STORM [94]. Furthermore, in STORM, CS has been also exploited to enhance three dimensional imaging, thanks to novel molecules localization algorithms [95], or thanks to the controlled introduction of aberrations [96].

Another well-established super resolution technique which suits compressed acquisitions is Structured Illumination Microscopy (SIM) [30]. SIM is a technique that, by modulating light at the back focal plane of the illumination objective, obtains an excitation pattern which has sub-diffraction fringes. To recover the final super-resolved image, to extend the system Optical Transfer Function and consequently go beyond Abbe’s limit, several raw images must be collected, corresponding to different patterns at the image plane. In this framework, CS has been used to reduce the number of spatial pixels to be sampled, decreasing the amount of collected data [97]. Furthermore, SIM schemes have been designed to include SLMs or DMDs to perform the cited light modulation, even by using LED excitation source [84]. Despite in the presented thesis, a similar strategy is applied to fluorescence microscopy, super resolution is not achieved.

Together with super resolved microscopy, CS has been successfully integrated in single element imaging, in a well-studied configuration named Single Pixel camera. SPC working principle has been described in the previous section and is one of the microscopy fields in which CS is more beneficial. Furthermore, this thesis might also be intended as one application of SPC to fluorescence imaging, as it will be clarified in the next chapters.

A more standard and widespread microscopy approach is that of confocal microscopy [98], [99], in which a point probe is used to scan the whole plane of interest. The excited fluorescence signal is consequently filtered by a pinhole, rejecting out of focus contributions, and then collected by a surface detector. A raster scan approach is intrinsically slower than others standard techniques like LSFM, hence Compressed sensing offers the possibility to reduce the number of points to acquire and their total acquisition time. To overcome the limit given by the design of a confocal microscope, many modifications have been adopted to include a spatial modulation of the excitation light, which is of importance when applying CS [100], [101]. For example, Ye et al. show in [102] how a random set of pinholes, which constitutes a random measurement basis, is exploited in CS-confocal microscopy. Here. the degree of optical sectioning is related to the degree of sparsity of the set of pinholes. However, this parameter is obtained at cost of photon budget efficiency, which might be crucial. Another remarkable example of CS in confocal design is given by [103], where a subsampling of the acquired data point is obtained. Said under sampling alone however is not sufficient to reconstruct the wanted signal: incoherence between measurement and representation matrices is not kept. This lack of incoherence strongly hinders the reconstruction process, which might be affected by artifacts [104]. However, said problem can be solved by considering the system Point Spread Function, so that any sampled value is a linear combination of the adjacent information content. The reported approaches both obtain a compression ratio higher than 90%, with an improved SNR.

Another possible strategy to achieve optically sectioned imaging is on Structured Illumination Microscopy (SIM). In SIM, the sample is illuminated by a tailored set of light patterns and is then acquired by a pixelated sensor. Light modulation enables the use of compressed reconstruction strategy as well depicted by Parot et al. in [105] where SIM combined with CS, achieves fast acquisition of neuronal activity in *Danio rerio* (zebrafish). As choice of measurement set, the authors here use Hadamard patterns, which well fits the specimen sparsity and the hardware involved. In fact, the small number of non-zero pixels implies that representation of neuronal activities has a low-rank matrix structure.

Despite their different applications and hardware implementations, compressed acquisition strategies based on CS all have a common paradigm, which is light modulation. Light modulation in fact, acts as information encoder which is exploited to optically perform inner product between vectors, that, if correctly represented, can be restored with a limited number of frames. In the next chapter of the thesis, it will be presented how light modulation has been obtained and the main motivation beyond the adopted system design.

2 DESIGN AND OPTIMIZATION OF THE OPTICAL SETUP

In this second section of the thesis, the concepts illustrated in the first chapter will be implemented in an optical setup to obtain optically sectioned volumetric imaging by selectively illuminating a volume. Furthermore, the controlled patterning of light enables the use of Compressed Sensing, a signal processing technique which makes it possible to reconstruct the spatial distribution of fluorophores in the field of view after a set of measurements which would be insufficient according to Nyquist-Shannon criterion. This makes the developed technique a gentle approach to investigate *in vivo* dynamics. On top of this it will be discussed the light source used in the presented setup: an LED. Incoherent sources are not usually chosen for microscopy due to the technical difficulties in focusing the incoming, high divergence, excitation beam. However, thanks to the spatial modulation provided by a Digital

Micromirror Device, it is possible to perform optically sectioned compressed imaging with an LED, in a technique called Spatially Modulated Selected Volume Illumination Microscopy (sm-SVIM). First, they will be described the optical performances of the developed setup, for then also giving an overlook of the optimisation procedure held to increase to light budget efficiency, namely the use of a light pipe and of a Total Internal Reflection (TIR) prism. Finally, it will also be described how the lateral modulation was extended, compared to the initially described version of the setup.

2.1 OPTICAL SETUP

In Figure xi, it is represented a sketched version of the first implemented optical setup. The light emitted from a LED (*Thorlabs* SOLIS-445C) is collected and refocused over a uniform, circular spot on the DMD (*Texas-Instruments* DLP LightCrafter 6500) by three lenses, which are set to be in a well-known Köhler configuration. The first collecting lens $f_1 = 200\,mm$ (*Thorlabs* AC508-200-A-ML) is directly attached to the LED, while the field or base lens is of focal $f_2 = 20\,mm$(*Thorlabs* AL2520-A) and the condenser, $f_3 = 50\,mm$ (*Thorlabs* LA1131-A).

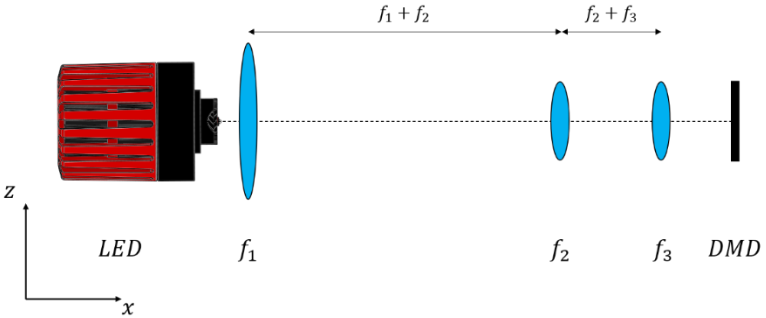

Figure xi: First SVIM implemented illumination schema.

Once illuminated, the DMD then reflects the light according to the programmed binary mask on the sample: the DMD plane is in fact optically conjugated with that of the specimen through a tube lens (Olympus SWTLU-C), of focal length $f_{TBL1} = 180\,mm$, and an objective lens. As also displayed in Figure xi, the modulation happens on yz direction, which is orthogonal to that of light propagation. The excited fluorescence signal is then collected and refocused by a detection objective and after being filtered its passes through a second tube lens of focal length $f_{TBL2} = 200\,mm$ (Nikon MXA20696) which focuses it on a CMOS camera (Hamamatsu Orca Flash 4.0).

In the previous description, it has been intentionally omitted the objective lens used both in illumination and in detection. For the setup implementation in fact the two lenses are easily changeable, making the microscope readily adaptable to any possible specimen dimension, up to 7 mm of field of view. To this thesis extent, they have been tested both in illumination and detection three different objectives: a 2X (Mitutoyo Plan Apo Infinity Corrected Long, 0.055NA 34mm WD), a 4X (Nikon CFI plan Fluor, 0,13 NA, 17,2 mm WD) and a 5x (Mitutoyo Plan Apochromat Objective 0.14 NA, $34\ mm$ WD). In any case, imaging the DMD plane with different magnification on the sample, consequently, changes the modulated volume extension, which must fit the Field of View. As described in the Light Sheet Engineering section in the previous chapter, this is determined by the detection magnification and sensor size.

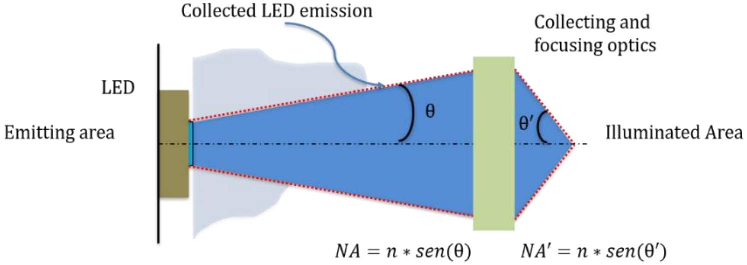

Figure xii: Analysis of the optical étendue of an LED

2.1.1 Incoherent Light Source

In a piece-by-piece description of the setup, the first, highlighted component is the light source. This is one of the notable points of the presented work: an LED is used in an optically sectioned imaging. The reason why incoherent light sources are not usually employed in such condition is described in [106] where a quantity named optical étendue is introduced: said quantity is related to the angular divergence of light emitted by a surface. Mathematically speaking, it is represented as:

$$dG = n^2 dS \cos(\theta)\, d\Omega\,. \qquad 2.1$$

Where n is the refractive index of the propagation medium, dS is the infinitesimal surface element and $d\Omega$ is the divergence solid angle. Eq. 2.1, in the case of a constant emission or focusing solid angle per infinitesimal surface element, can be rewritten as:

$$G = \pi \cdot S \cdot NA^2. \qquad 2.2$$

This optical parameter considers the angular light acceptance of an element with respect to its spatial extension. It can be evaluated at different points in the optical path to calculate the number of photons per unit's area lost in the propagation. A lossless system is in fact such that the étendue is a constant value. As depicted in Figure xii, another possible meaning of the étendue is that of quantifying the effort needed to focus an highly diverging light profile over a small area: the smaller the area at a given divergence, the higher the photon losses.

These losses are not usually an issue when using commercially available laser sources, since they provide a small divergence of the output beam (often $< 1.5\, mrad$), which is therefore easy to collect and easy to refocus over a diffraction limited spot. Nonetheless in this thesis work an LED was used instead of a conventional coherent source. An LED is such that photons are spread over a large angle (almost over a solid angle of 2π) and are emitted from a large area (⃠ $3mm$ for the LEDs sources used in this work) so that only a small fraction of them can be practically of use for imaging applications, even with collecting optics of large optical power. Furthermore, the low spatial coherence of the emitted photons implies a shorter persistence length of the illumination beam, compared to those presented in the previous chapter.

In a technique like LSFM, in which light is tightly focused along one dimension, it is impractical to use low coherence source. However, in SVIM, since light is focused over larger, modulated volumes, it is possible to obtain a sufficient power density at the sample plane to perform fluorescence imaging, especially with new commercially available high power LED sources.

Along with the cited drawbacks, an incoherent source brings together also some advantages compared to conventional lasers. The most remarkable of these is the removal of shadowing artifacts, which are typical of LSFM. Shadowing artifacts, an example of which is shown in Figure xiii a), are given due to the presence of scattering and absorbing centres in the sample. These centres may hinder light propagation, thus resulting in shadowing stripes parallel to the light sheet. That might be the case for pigment on the skin of a biological sample. Since the absorbing process of such centres depends on the spatial frequency of the incoming photons, having a source with a broad frequency support prevent the formation of these artifacts[28].

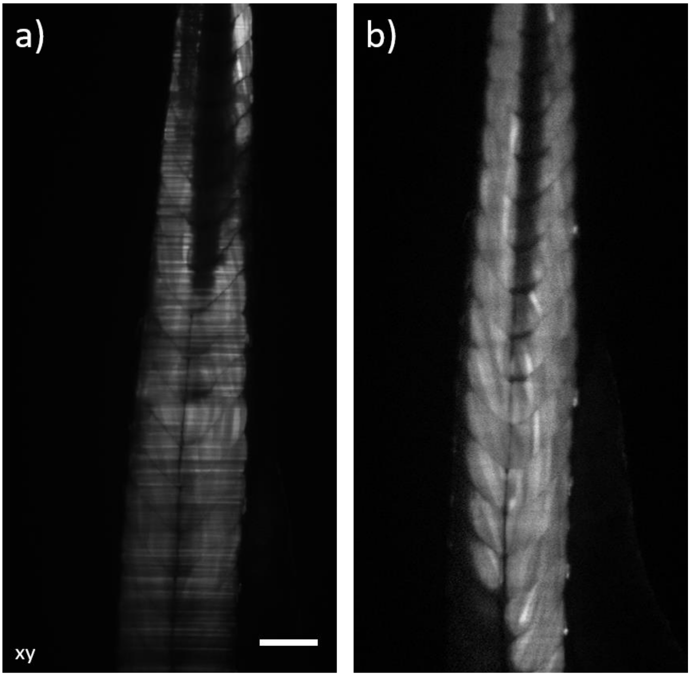

Figure xiii: a) Shadowing artifacts in LSFM due to absorbing centres and coherent source, (b) same part of the sample reconstructed with sm-SVIM with LED [26].

In Figure xiii it is presented a comparison of the same plane of the sample acquired both with a LSFM illumination, and with sm-SVIM. As anticipated, panel a) clearly shows the presence of the typical shadowing artifacts, which are not present in b) due to LED illumination. The presented solution to avoid striping artifacts anyway is not unique, it has in fact been proposed in [107] a strategy called *pivoting* where the light sheet is tilted with respect to the optical propagation axis, to illuminate beyond the absorbing centres. Once many frames are taken at different angle of view, they are merged into one single frame which contains information otherwise not accessible. Anyway, *pivoting* requires the acquisition of multiple views, overexposing the sample and therefore it might result in unwanted light damage and photobleaching of fluorophores.

As a final remark, using an LED also brings together more advantages in terms of cost, colour availability and stability of the source. In fact, the manufacturing process of a light emitting diode is cheaper compared to that of laser and comes with a easier tunability of the emission process. This last point is particularly useful when designing a setup for fluorescence microscopy: here it is crucial that the source emission and excitation spectra overlap. Furthermore, light source power emission must be constant along the measurement routine, to prevent the reconstruction to suffer from so induced artefacts, which is the case for LEDs.

The presented points altogether justify the use of an incoherent light source. Nonetheless a possible way to overcome to the limited persistence length of the obtained illumination profile will be illustrated in the lateral extension section.

2.1.2 Köhler Illumination

The benefits brought by an incoherent light source have been widely discussed in the previous section of the thesis, together with the technical difficulties in using a light source as such. Nonetheless in this paragraph it will be explained how the incoming light from a LED was collected and then refocused to perform fluorescence microscopy.

Since the volumetric acquisition encodes the spatial distribution of fluorophores thanks to different light patterns, it is crucial that the fluorescence signal variation is only given by two factors: different modulation mask and fluorophores distribution. If by any chance, further modulating factors are present, as it might be the case for striping artefacts or non-uniform illumination spot over the Spatial Light Modulator, these will most likely induce error in the reconstruction obtained by problem inversion. To this extent, it is crucial that the power distribution over the modulating pixel of the DMD is constant over a uniform pattern.

As shown in Figure xiv a possible solution to avoid inhomogeneities with a LED is that of using a condensing optical apparatus which is called Köhler illuminator. This system aims at evenly illuminating the sample (in this case, the DMD pixel matrix) and has been widely used in many different fluorescent microscopy implementations. Starting from the light source, the first element encountered is a collector lens (also referred to as field lens), whose goal is that of collecting the incoming high diverging light, and to refocus it over a plane in which a diaphragm is placed (named field stop). A variation in said diaphragm aperture implies a magnified variation at the sample plane, i.e., a change in the spot size at the SLM reflective surface. Then, a $4f$ system made by a base and a condenser lens images the field stop plane, magnifying said plane by a factor of $M = -\frac{f_{cond}}{f_{base}}$, in which the two values are the focal length of the condenser and of the base lens, respectively. Finally, an aperture stop is placed in the optical centre of the $4f$

system, to manually control the light intensity shining over the DMD [108].

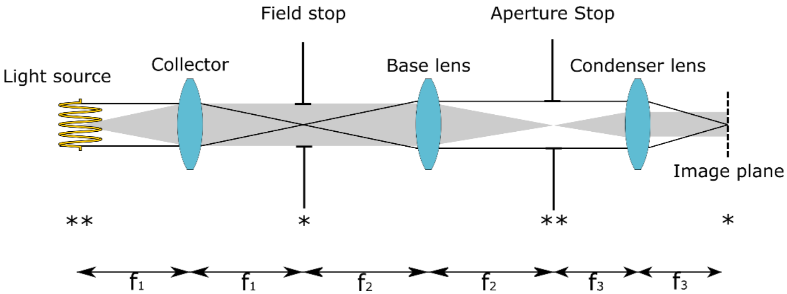

Figure xiv: Scheme of a possible Köhler implementation. The grey area and the black lines highlight different paths travelled by the illumination photons.

Thanks to a Köhler illuminator design, a uniform light spot is obtained to illuminate the spatial light modulator, despite using a non-uniform light source, avoiding the presence of error in the recovered fluorescence signal. Finally, the introduction of two diaphragm to control both light intensity and spot size of the produced light spot, is fundamental in experimental condition to maximize the signal contrast. In this thesis work, the illumination was designed so that on the DMD a uniform spot of 1.2 cm diameter was obtained, thus determining together with the illumination objective, the illuminated volume dimensionality.

2.1.3 Light Modulation

Köhler illuminators are widely used to illuminate the sample, which is thus set to be in the focal plane of the condenser lens. In this thesis work, however, a Köhler subsystem is set to illuminate a Digital Micromirror Device, which enables light shaping. While the main feature of a DMD have been discussed in the first chapter, in the next section it will be discussed the specific device used in this thesis, namely a Texas-Instrument DLP LightCrafter 6500. This product is designed to have the ON and OFF state, respectively corresponding to a tilt of $+12°$ and $-12°$, as shown in Figure xv. The DMD used consists of $1920 * 1080$ squared mirrors, whose pitch is $7.56\ \mu m$. Finally, the device maximum transition frequency between the ON-OFF states is $9{,}523\ Hz$. However for fluorescence imaging and common exposure times, said frequency is not a limiting factor for the final frame rate of the technique.

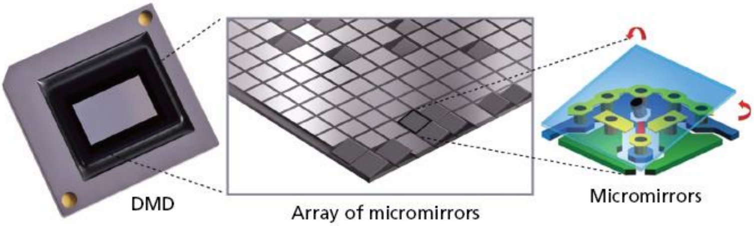

Figure xv: Detail of a DMD matrix (DLP products, Texas Instruments).

As previously pointed out, the DMD is positioned so that the reflected light is directed along the illumination axis, as displayed in Figure xi. Furthermore, for its design, DMDs are made so that the pixel rotation happens around its diagonal: for this reason, in the implemented setup, the whole DMD mount was rotated by a 45° angle. On top of this, this peculiar custom-made mount granted for in-plane light propagation, with no need of tilted prisms or strong modification in a standard LSFM design.

After being reflected by the DMD, light travels through two optical elements (a tube lens and an objective lens) which optically couples the modulation plane with that of the sample enabling the axial patterning used in sm-SVIM. More in detail, the light modulation provided by the SLM happens along a yz plane, whereas along its propagation axis x, the beam follows a divergence profile dictated by the objective lens used. Furthermore, this last objective lens will have a limited depth, which will hence result in a limited persistence length of the illumination profile. This spatial divergence strongly hinders imaging of volumes of high extension along the x axis.

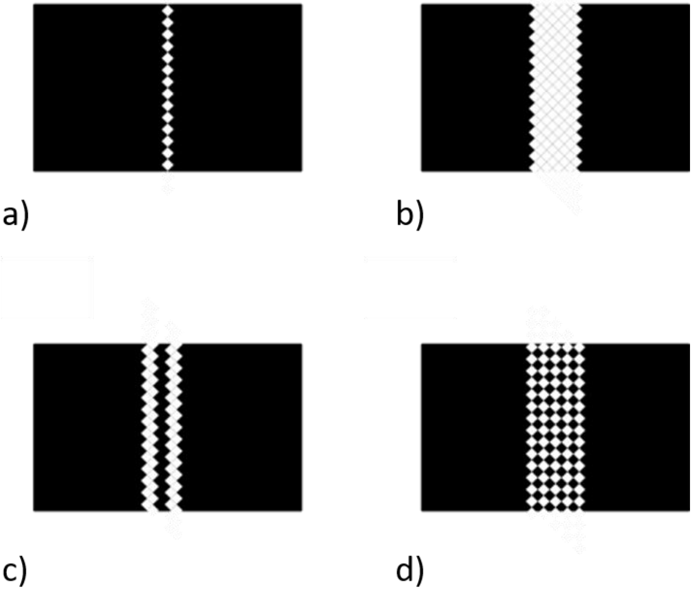

Figure xvi: Different illumination patterns. (a). line modulation for light sheet behaviour; (b) constant, "on" pattern over a thick region; (c) and (d) patterns at higher spatial modulation.

To assess for the modulation capability of the system, the spatial mount of the DMD is so that a single, vertical line of “on” pixel shows a diamond shaped profile, as highlighted in Figure xvi. Said $45°$ rotation of the single active element is also present in patterns with different shapes and dimensions. For the sake of clarity, since the DMD plane is conjugated to that of the sample, the thickness of the modulation pattern corresponds to the axial extension of the modulation, which must be contained in the depth of field of the detection objective. Hence, the capability at which details of the sample can be axially distinguished is determined by smallest degree with which is possible to axially modulate light, which is therefore related to the DMD pixel diagonal.

More in details, the lateral resolution of the imaging system is determined by the numerical aperture of the objective lens, as formulated in Eq. 1.1, and can be easily estimated.

Abbe’s formula, when imaging a GFP ($\lambda_{exc} = 450\ nm, \lambda_{em} = 532\ nm$) with a 5X detection objective ($NA_{det} = 0.14$, widely used in this thesis), is equivalent to:

$$\Delta\rho = \frac{\lambda_{em}}{2 \cdot NA_{det}} = \frac{532\ nm}{2\ \cdot 0.14} = 1.9\ \mu m. \tag{2.3}$$

Conversely, axial resolution is given by the illumination optics angular acceptance, as specified in the previous chapter and in Appendix A. In the case in which a 4X illumination objective is used ($NA_{ill} = 0.13$), this would give diffraction limited illumination spot of

$$\Delta\rho = \frac{\lambda_{exc}}{2 \cdot NA_{ill}} = \frac{450\ nm}{2\ \cdot 0.13} = 1.7\ \mu m. \qquad 2.4$$

Anyway, in the presented setup, a single active pixel of the DMD would result in a bright spot at the image plane whose dimension would be given by:

$$d_{DMD}^{image} = \frac{d_{DMD}}{M} = \frac{7.56\ \mu m}{4} = 1.89\ \mu m, \qquad 2.5$$

which is bigger than the result of Eq. 2.5. This mismatch in DMD single pixel imaged dimension and illumination lens diffraction limit is such that the ultimate axial resolution achievable is proportional to the first term rather than the second.

On top of that, the diamond vertical modulation presented in Figure xvi implies that, to correctly evaluate the axial resolution of the technique, it must be considered the effective distance between two adjacent pixel lines. This leads to an effective thickness of a single line patterns of

$$e = \frac{d_{DMD}^{image} \cdot \sqrt{2}}{2} = 1.34\ \mu m. \qquad 2.6$$

To correctly evaluate the lateral resolution of sm-SVIM however, it must be considered that diffraction limited performances are achievable only at the centre of the detection DOF. Therefore, when dealing with thicker samples, the volume which can be correctly reconstructed is that confined within said DOF.

Due to the fact the axial modulation happens simultaneously, the sensor will detect signal contribution both from in focus and out of focus planes. Hence it is of interest to estimate the biggest volume achievable for a given detection objective, for which, the largest axial extent will be achieved when then modulation fully covers the DOF. As presented, considering the same detection objective as in the previous considerations, this will lead to:

$$DOF_z = \frac{n \cdot \lambda_{em}}{NA_{det}^2} + \frac{n \cdot \delta_{pixel}}{M \cdot NA_{det}} \approx 27\ \mu m. \qquad 2.7$$

Here, the first term is given by the optics constraint, while the second arises from the limited dimension of the sensor pixels, as illustrated in chapter 1. Nonetheless, a total thickness of about double the value obtained can be considered as acceptable. By considering an axial extension of a single line at the DMD of $e = 1.34\ \mu m$, it results that said thickness can be entirely illuminated by about 40 adjacent SLM lines, thus determining the maximum modulation extension.

One last limiting factor to the imaging volume extension is that given by the small persistence length implied using an LED. To overgo this limitation, the illumination objective lens has been mounted on a fast-translating stage (*Physik Instrumente,* C-413 PIMag Motion Controller), which moved along the acquisition of a single pattern. Said movement, together with its synchronisation with the camera sensor readout, resulted in an effective pattern with an enhanced persistence length, thus covering not only its central part, but the whole sensor. This means that the lateral profile of the modulation will ultimately be limited not by the patterning lateral extent, but by the sensor dimension reported at the sample plane instead.

Considering the sensor used in the work presented in this thesis, a $2048 * 2048$ CMOS, the lateral extension of the modulated volume by considering the same detection lens is:

$$\Delta X = 2048 \cdot \delta_{pixel} = 2.67\,mm \tag{2.8}$$

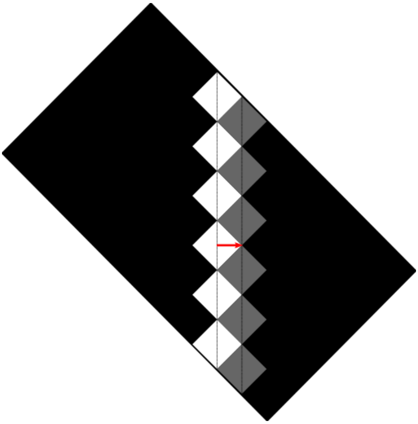

Figure xvii: Effective distance of two adjacent lines, their centres are half of the diameters separated.

Nonetheless the system is prone to an easy modification of the imaging volume by changing the illumination and detection objectives. This is done according to the sample size and features of interest. In this thesis, they have been extensively used and tested three long working air objectives, which have been employed both for refocusing the incoming excitation pattern and for fluorescence signal collection. Of course, by modifying NA_{ill} and NA_{det}, they are consequently modified the pixel size reported at the sample chamber and the detection depth of field. These two changes can be easily seen from Eq. 2.5 and Eq. 2.7.

For example, by interchanging the 4X (presented as illumination lens) and the 5X (previously considered as detection lens), this would give a slightly bigger Field Of View and depth of field, namely $\Delta X = 3.33\,mm$ and $DOF_z \approx 32\,\mu m$, and a smaller DMD pixel size, $e = 1.07\,\mu m$. Furthermore, imaging in these experimental conditions would be limited laterally by a resolution of $\Delta\rho = 2.05\,\mu m$. Conversely, in the case of imaging samples whose size is several mms, a larger FOV is achievable by using a 2X, long working objective of $0.055\,NA$, both as illumination and detection lens. Smaller magnification would together lead to a reported DMD pixel size of $e = 2.67\,\mu m$, a $DOF_z \approx 176\,\mu m$ and a lateral resolution given by Abbe's limit of $\Delta\rho = 4.83\,\mu m$. Said conditions altogether also results in a extended FOV of $\Delta X = 6.66\,mm$.

On top to the experimental imaging conditions described, the uniform spot obtained on the DMD thanks to the Köhler illuminator is consequently magnified and imaged onto the sample. The luminous spot of $1.2\,cm$, and yet the illumination magnification, must be such to completely illuminate the FOV, pointed as ΔX in the previous descriptions. The magnification factors of $M = 2, 4\ , 5$, respectively leads to a modulated volume which extends on $\Delta X_{ill} = \ 6\ mm\ , \Delta X_{ill} = \ 3\ mm$ and$\Delta X_{ill} = \ 2.4\ mm$, hence almost completely shining light over the maximum detectable FOV.

As a final remark, in the evaluation of the optical parameters given in the previous part of this section, a refractive index $n = n_{water}$ has been considered. However, for cleared samples immersed in denser media, the last consideration may lead to an underestimation of those values. In particular, in the cases of Benzyl Alcohol Benzyl Benzoate (BABB) and Ethyl Cinnamate, used as imaging media in the experimental validation, their refractive indexes are $n_{BABB} = 1.568$ and $n_{ETC} = 1.558$, respectively (see Appendix C for more details). For this reason, they have been chosen modulation patterns whose axial extension extends well beyond the presented DOF_z, so to seize any imageable, modulated, information about the fluorophore distribution. Further details on how this has been practically achieved will be given in the next chapter, together will the whole measurement and reconstruction routine.

2.2 OPTIMIZATION OF THE OPTICAL SETUP

In this section it will be discussed how the performances of the designed setup have been optimized.

Firstly, it will be given an overall description of the lateral field extension, obtained as previously written, thanks to synchronisation between objective lens movement and sensor reading mode. This description will have a particular regard to light propagation in media when moving the stage: from this analysis in fact, they can be derived the experimental parameters needed for the best synchronisation of the hardware components involved.

Secondly, it will be reported how the illumination efficiency has been optimised. Maximizing photon collection after the SLM reflection and refocusing it at the sample plane is in fact critical. As suggested by the DMD constructor, in this thesis two possible implementations have been investigated to solve such issue: using a Total Internal Reflection (TIR) prism, and/or a light pipe.

2.2.1 Lateral Volume Extension

The total span of the illumination beam waist is limited by the dimensionality of the sensor, which, in the case of a $NA_{det} = 0.14$, led to an overall lateral extension of the Field Of View of $\Delta X = 2.67\,mm$. Anyway, this displacement at the sample plane was not linearly connected to the translation of the illumination lens. It is hence necessary to calculate the effect of the objective lens translation and on the refraction given by the different media encountered by the excitation beam before reaching the sample.

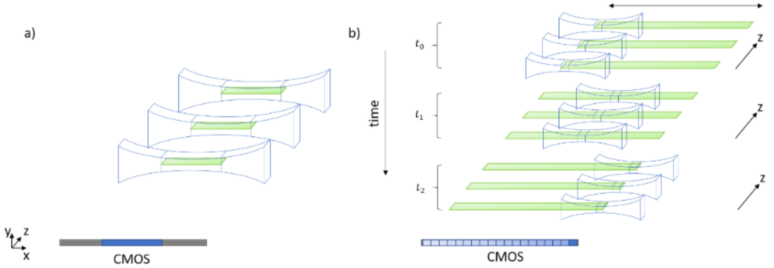

Figure xviii: Working principle of lateral field extension. In (a) a static situation is represented, here, only a small central part of the volume is modulated so to obtain a good reconstruction whereas in (b), the modulated field is extended through synchronisation of illumination lens motion and CMOS reading.

The schematics of the illumination axis is depicted in Figure xix, representing how light is propagating after being reflected by the DMD. Let a be the distance between the DMD and the tube lens which collects the incoming modulated radiation, and let b be the distance from this last element to the objective lens, b can be also expressed as the sum of tube and objective lens focal range: $b = f_{tube} + f_{objective} = f_0 + f_1$. Finally, let c be the output image distance from the last element. By writing the law of the thin lenses:

$$q = \frac{p \cdot f}{p - f} \qquad 2.9$$

where p and q are the object and the image plane distance from the principal axis of the system, respectively, the tube lens will form a virtual image of the DMD display at a distance which is given by:

$$q_0 = \frac{a \cdot f_0}{a - f_0}. \qquad 2.10$$

Said virtual image will be place $p_i = b - q_0$ away from the objective lens. By considering again Eq. 2.9 to evaluate the final position of the DMD image, one obtains:

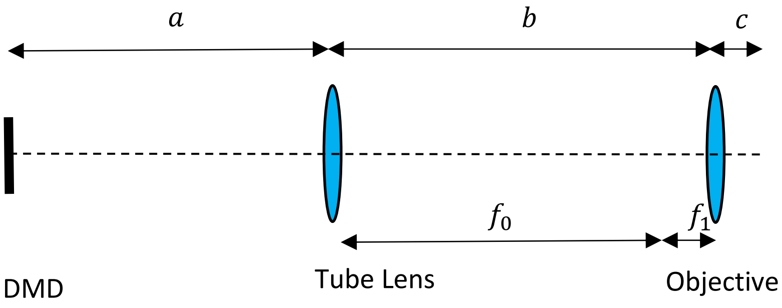

Figure xix: Schematics of the two-lens system illumination path.

$$c = \frac{p_1 f_1}{p_1 - f_1} = \frac{(q_0 - b) f_1}{(q_0 - b - f_1)} = \frac{\left(-\frac{a f_0}{a - f_0} + b\right) f_1}{-\frac{a f_0}{a - f_0} - f_1 + b} \qquad 2.11$$

To consider the translation of the objective lens, it means to evaluate how a variation in b affects the image formation i.e., c. From the presented analysis, a shift Δb implies a Δc of two orders of magnitude lower, thus not justifying strong non linearities between objective and DMD image shifts.

When propagating, light encounters different media, which to this extent may induce a discrepancy between these two quantities. Starting from the DMD, which is in air, light in fact travel through three different layers and therefore two interfaces between different refractive indices, as shown in Figure xx. The three media are, starting from the closest to the DMD: air, whose index is $n_{air} = 1$; optical glass, which contains the imaging medium and is $2\,mm$ thick, with $n_{glass} = n_1 = 1{,}51$; and lastly the immersion medium, n_2, which depends on the clearing procedure the sample has been subjected to.

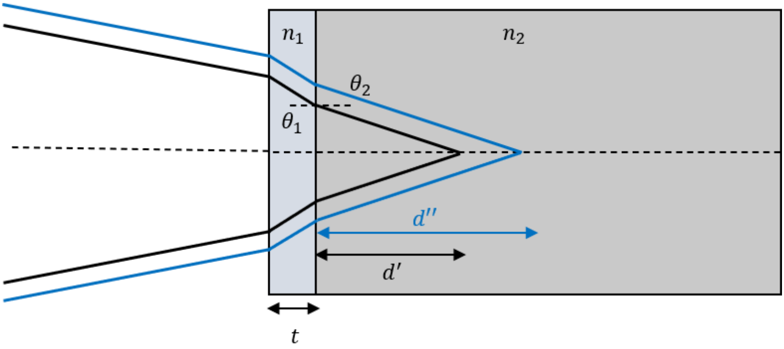

Figure xx: Refraction at different media interfaces.

The mathematical relation that exists between refractive index and refraction angle is the so-called Snell law:

$$n_0 \cdot \sin\theta_0 = n_1 \cdot \sin\theta_1 = n_2 \cdot \sin\theta_2\,, \qquad 2.12$$

with θ_1 and θ_2, being the angle of divergence of light propagating in optical glass and in the imaging medium, respectively. Given that the n_{air} as well as the other refractive indices are known, so is θ_0 which is given by the illumination objective numerical aperture, the following equalities hold:

$$\theta_1 = \sin^{-1}\left(\frac{\sin\theta_0}{n_1}\right)$$
$$\theta_2 = \sin^{-1}\left(\frac{\sin\theta_0}{n_2}\right). \qquad 2.13$$

Once known the divergence angles in the different media and the input beam spot at the different interfaces (namely h' and h'' from the optical axis), from geometry, one can obtain that:

$$h' = d' \cdot \tan\theta_2 + t \cdot \tan\theta_1$$
$$h'' = d'' \cdot \tan\theta_2 + t \cdot \tan\theta_1. \qquad 2.14$$

Hence, the final displacement along of the image plane on the horizontal axes can be evaluated as:

$$\Delta x_0 = \frac{h'' - h'}{\tan\theta_0}, \qquad 2.15$$

that, together with Eq. 2.14, finally result in:

$$\Delta x_0 = \frac{(d'' \cdot \tan\theta_2 + t \cdot \tan\theta_1) - (d' \cdot \tan\theta_2 + t \cdot \tan\theta_1)}{\tan\theta_0}$$
$$= \frac{(d'' - d') \cdot \tan\theta_2}{\tan\theta_0} = \frac{\Delta x_1 \cdot \tan\theta_2}{\tan\theta_0}. \qquad 2.16$$

Thus, knowing the optical properties of the imaging medium, it is possible to predetermine the overall displacement of the illumination lens to cover the FOV which is given by both the sample size and magnification of the detection lens. Experimental demonstration and assessment of the technique will be given in the next chapter.

2.2.2 Total Internal Refraction Prism

The construction principle of the DMD is so that a non-tailored solution to collect the light reflected from it is such that the collection axis itself is tilted with respect to the light propagation axis. This is also the case for the presented Köhler illumination schema. In brief, to have a reflected beam orthogonal to that of the DMD, which is in the “on” state, and considering the geometry of the device, incident and reflected beams must be tilted by a mutual angle of $24°$, as it is shown in detail in Figure xxi.

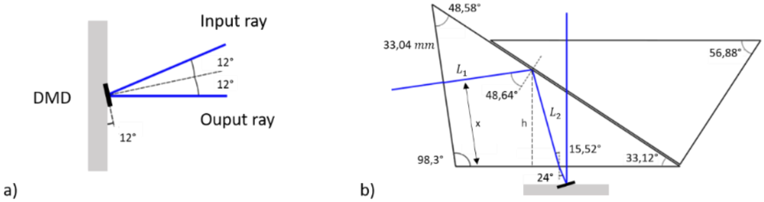

Figure xxi: (a) Schematic of the light path after being reflected by a DMD “on” pixel (b) Geometrical propagation of light in the TIR prism are relative dimensions.

In practice, this configuration proved to be not very practical to be aligned. Furthermore, being photon harvesting from the DMD a critical parameter, another approach to optically couple spatial modulation and illumination optics was needed. Moreover, for the technique to be successfully applied, the light modulation must be exploited so to be orthogonal to the detection sensor, or, rephrased, a single active line at the DMD plane must result in a excitation profile which sections the sample orthogonally to the detection axis.

A possible solution to the tedious problem of optical alignment is that presented in literature [109][110], where a Total Internal Reflection prism is specifically designed the collect and redirect the incoming and the modulated light respectively in a proper way. To the end of this thesis, a TIR prism was custom-tailored and produced in N-BK7, a widespread material in optical elements.

For the sake of completeness, the designed TIR prism is that displayed in Figure xxi, it is made by two prisms of triangular surface, with two of their lateral surfaces fixed one on the other. In this design, a relatively small incidence angle is reflected orthogonally to the DMD surface, so that the Köhler illuminator can be positioned almost parallel to this surface.

The light path geometry in the TIR prism can be easily calculated by considering the basic Snell Law of refraction, together with the dimensions of the system. From the assumption of an incidence angle of $24°$ on the DMD plane, it can be retrieved that the Köhler illuminator should have its optical axis tilted by $\theta = 0{,}093°$ with respect to the prism input surface. Being this angle particularly small, in practice the Köhler subsystems can be put perpendicularly to this surface.

For the TIR prism to perform correctly, total internal reflection must take place at the glass-air interface between the two glass prisms. From the definition of total internal reflection, the critical angle at which this can take place is:

$$\theta_{critical} = \sin^{-1}\left(\frac{n_{air}}{n_{glass}}\right) = \sin^{-1}\left(\frac{1}{1.52}\right) = 41.13° \qquad 2.17$$

From Figure xxi, the system was designed so that the incidence angle on the input prism surface was slightly greater than $\theta_{critical}$, namely $\theta_{incidence} = 48.64°$, ensuring total internal reflection. Conversely, after being modulated and reflected by the DMD, light travels through the air gap in between the two glass triangles: by doing so, refraction happens both in travelling from glass to air and from air to glass. The symmetry of the travelled path is such that said double refraction results in a lateral shift of the image which is therefore proportional to the in-air path. Being the gap as small as possible by construction, said lateral shift can be neglected.

A final remark must be made on how the presence of the prism affects the systems. The refraction induced by the prism might in fact modify the overall optical power of the illumination so that it must be considered to obtain a uniform, circular spot on the DMD, of the correct size. The first step in this consideration is evaluating the total path travelled by the light in glass. To this extent, let it be x the position at which light enters the prism. From geometrical reasoning, it follows that:

$$L_1 = (33{,}04 - x) \cdot \tan(48{,}58°), \qquad 2.18$$

which is related to the path travelled after reflection by:

$$h = x \cdot \cos(8{,}3°) + L_1 \cdot \sin(8{,}3°)$$
$$L_2 = \frac{h}{\cos(15{,}52°)}. \qquad 2.19$$

With a total path in glass of:

$$L = L_1 + L_2. \qquad 2.20$$

Eq. 2.20, with the prism parameters, gives as result $L = 38{,}50\,mm$, by using $x = 16{,}52\,mm$. Furthermore, by considering θ_0 as the numerical aperture of the last lens of the Köhler illuminator, it follows that:

$$\Delta h = L \cdot (\tan\theta_0 - \tan\theta_1), \qquad 2.21$$

where $\theta_1 = \sin^{-1}\left(\frac{\sin\theta_0}{n_{glass}}\right)$. Altogether, the previous equations, makes it possible to evaluate the optical shift of the system working distance induced by the presence of the prism, which is finally calculated as:

$$\Delta_{WD} = \frac{\Delta h}{\tan\theta_0} = \frac{L \cdot (\tan\theta_0 - \tan\theta_1)}{\tan\theta_0} = L \cdot \left(1 - \frac{\tan\theta_1}{\tan\theta_0}\right), \qquad 2.22$$

which has considered in the system alignment. As a final remark, being n_{glass} greater than one, it holds that $\Delta_{WD} > 0$.

In this paragraph it has been proven how the light coupling between a Köhler illuminator and a DMD can be increased by introducing a glass prism in the setup, without incurring in major side-effects. Moreover, by making the optical paths before and after the SLM almost orthogonal, the use of a TIR prism enables to simultaneously house a second light source in the system (*Thorlabs* SOLIS-623C), peaked at $623\,nm$ which can hence perform multicolour imaging. In the first presented sketch of the setup, this feature was not achievable due to the small tilt angle between the optical axis before and after the DMD.

2.2.3 Final setup implementation

As depicted in the previous sections, the use of an incoherent light source is strongly limited by its high divergence. Furthermore, for most LED, the high divergence also comes with a relatively large emitting surface (mm of side), which makes it even more difficult to tightly confine incoherent light over a small volume. To this aim, the well-studied Köhler configuration has been used, to efficiently harvest the incoming excitation photons. Nonetheless, different options have been taken in consideration and tested before considering the presented setup optimized.

The first option was using a flexible fibre optic light guide (*Edmund Optics*), which is basically made by a bundle of smaller glass guides which transmit light in the visible region of the spectrum. By illuminating the input surface of the bundle with an high numerical aperture source (the LED), light is so transmitted through the guide and then imaged on the DMD reflective surface. However, said approach was not feasible since the output light spot was not uniform but it instead showed a strong modulation, present in form of black spot over the output plane of the fibre itself. Said modulation was given by the disordered structure of the bundle: a non-illuminated single fibre at the input surface was not linked to a fibre at the same position at the output plane. Thus, by non-completely illuminating the first, a non-predictable mask of black dots was then reported at the DMD surface.

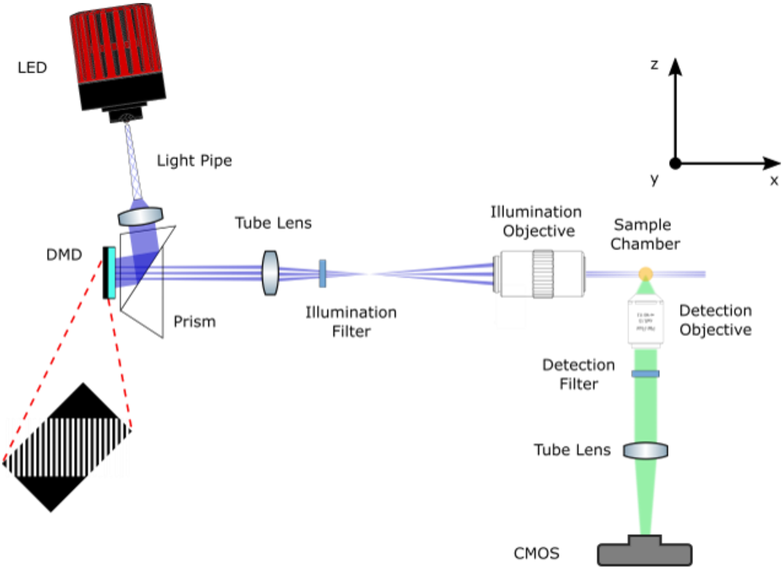

Figure xxii: Scheme of setup for sm-SVIM with a light pipe.

A second alternative was in principle similar to that of the fibre bundle: homogenizing light thanks to guided transmission to perform uniform illumination. It was hence used an homogenizing rod, as displayed in Figure xxii, with an hexagonal input surface. The rod, also called light pipe, is a glass prism, mostly found in elongated shapes, which transmits light thanks to total internal reflection. The massive number of internal reflections in fact, redirects light to uniformly fill the output surface. The output angular divergence is directly linked to the input numerical aperture and the ratio between the two access: it is constant the term $NA \cdot surface$, which follows from étendue conservation (Eq. 2.2). The light pipe was put as close as possible to the emitting surface and then its output plane was imaged by a compact lens module on the DMD. Differently from the fibre bundle, the glass rod proved to successfully uniform light. However, the induced photon losses were larger than those given by the Köhler configuration or the fibre bundle. The best-case scenario gave an overall power at the modulator which was a factor of two smaller than that given by the Köhler subsystem.

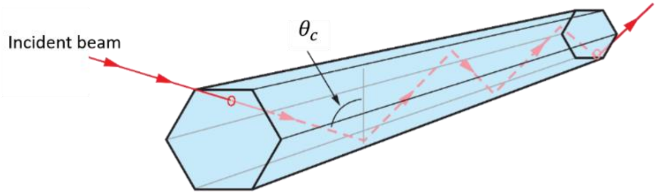

Figure xxiii: Working principle of an homogenizer rod.

Finally, other lenses arrangements were tested, in the end they all showed transmission and/or uniformity properties which were not comparable to the solution adopted. For this reason, the final system is that depicted in Figure xxiv, where a double colour illumination is introduced.

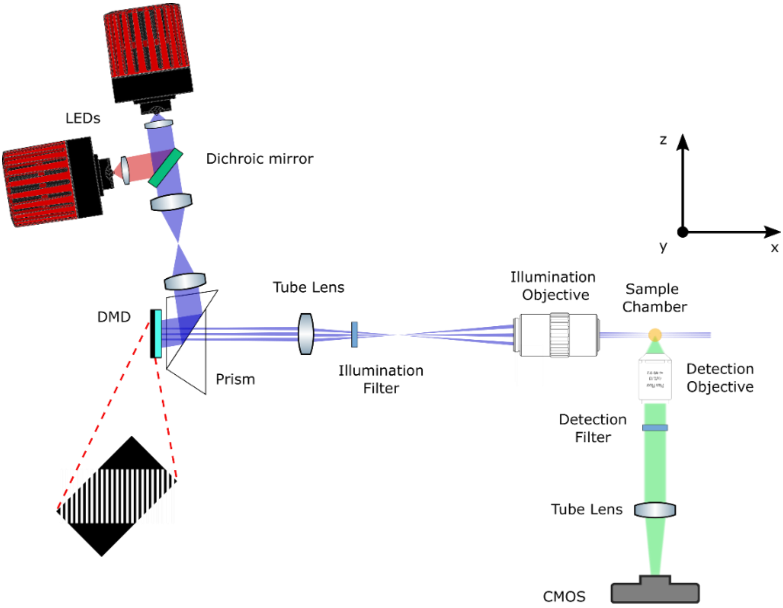

Figure xxiv: Scheme of the final, optimized setup for sm-SVIM. Dimensions are not in scale. Dimensions are not in scale.

3 SM-SVIM: TECHNIQUE CHARACTERISATION

Once obtained an optimized illumination path in terms of photon budget, a characterisation of the sm-SVIM overall acquisition protocol is needed, both in terms of optical properties and compression capability. As stated in the previous chapter, lateral extension of the Field Of View has been obtained thanks to a translation in the illumination lens, which is synchronized with the line-by-line acquisition of the CMOS sensor. Conversely in this chapter, it will be discussed how a deconvolution algorithm is implemented to enhance image quality along the axial direction.

Both CS and deconvolution have proven to be effective and beneficial to sm-SVIM, obtaining a reduced effective light dose at the sample, and an axial sharpening of the volume information, respectively.

3.1 SM-SVIM IMPLEMENTATION

3.1.1 SVIM with an LED

The photons emitted by an incoherent source as an LED are spread over a large angle of divergence, making it difficult to collect and refocus them without significant losses. To even worsen this scenario, one must also consider that most incoherent light sources have active areas which are orders of magnitude bigger than the usual dimensions of a light sheet. For example, with respect to the LEDs used in this thesis project, the emitting surface are of $3\,mm * 3\,mm$. Considering the typical dimensions of a light sheet in LSFM, which is about $10\,\mu m$, their mismatch hinders the possibility of tightly focus photon on a narrow plane. For said reason, LEDs are normally discarded as sources for LSFM set ups. However, by increasing the dimension of the illumination spot, these can provide the necessary power density to excite fluorescence.

As a further remark, excitation light is propagating along the x axis, whereas the detection path is built parallel to z, therefore denoted as lateral and axial dimensions, respectively. Illumination and detection paths have thus been designed to be mutually orthogonal, as in LSFM. Consequently, the spatial modulation is parallel to yz. After light is condensed and uniformly refocused by the Köhler illuminator, the DMD selectively reflects a pattern which is reported at the sample plane. This is obtained thanks to a tube lens conjugated with a long working air objective, whose magnification is M_{ill} numerical aperture is NA_{ill}. Said parameter puts a constraint on the depth of illumination and determines the modulated volume extension along the x axis without volume extension.

The spatial arrangement of modulation plane, sample chamber and detection path, results in an intensity profile at each sensor pixel, which is the weighted sum of each voxel contribution from the line Δz in front of said pixel. Thus, each camera pixel senses the result of a line integral over the axial direction of the emitted light, modulated by the DMD. The technique yields an acquisition and reconstruction procedures similar to those involved in SPC: the acquired signal is in fact a scalar product between line pattern and fluorophores distribution.

The total LED power of $3.5\ W$, was reported at the sample obtaining an intensity of about $500\ mW/cm^2$. This yields a value one order of magnitude smaller than those implied in a typical LSFM [1], [17]. Nonetheless the illuminated volume in sm-SVIM has an axial extension much bigger than LSFM, typically $100 - 150\ \mu m$ thick, 10 times that of a common light sheet.

The z extension of the pattern i.e., the thickness of corresponding modulated volume, must be such to completely fill the Depth of Field of the detection objective. Because of the used DMD, said thickness will be determined by the number of active pixels and their magnified dimensions, which has been discussed in the previous chapter, so that $\Delta z = N \cdot e$. Given NA_{det}, this determines both the DOF and the sensor size, so N and e are accordingly chosen. Considering a generic detection objective whose magnification M_{det} and characteristic NA_{det}, this leads to a detectable volume with sides $\Delta X = \Delta Y = n_{pixels} \cdot \delta_{pixel} = 2048 \cdot \frac{6.5\mu m}{M_{det}}$, after lateral modulation extension. Moreover, with a DOF_z by considering the tiniest degree of axial modulation $e = \frac{\frac{d_{DMD}}{M_{ill}} \cdot \sqrt{2}}{2}$, a volume thickness in the orders of 60 pixels lines is obtained. So that $N = 64$ and 128 care appropriate choices for the expansion of Walsh-Hadamard patterns. Nonetheless, with some experimental procedures that will be given in the section Pattern Binning, the number of modulating pixels can be further extended by a factor of 2.

Once the incoming signal is collected, a problem must be solved to retrieve the fluorophores volume concentration $\boldsymbol{\chi}(x, y, z)$. The problem is formulated upon the acquisition of N images $\xi_i(x, y)$, with $i = 1 \ldots N$, one for each basis element of the sampling set. After the measurement is performed, a pixelwise equation is set, in a form analogous to that presented in the first chapter:

$$\boldsymbol{\xi}(\bar{x}, \bar{y}) = \Phi \cdot \boldsymbol{\chi}(\bar{x}, \bar{y}), \qquad 3.1$$

where $(\bar{x}, \bar{y})$ is the position of the considered pixel, $\xi(\bar{x}, \bar{y})$ is the measured vector, Φ is the measurement matrix of shape $N \times N$ and $\chi(\bar{x}, \bar{y})$ is the fluorophores distribution on the line facing said pixel.

3.1.2 Optical features

The reconstruction method has been tested to quantify both its experimental lateral and axial resolutions, which are theoretically determined by the detection objective and DMD pixel dimension, respectively. It is hereby reported a quantitative analysis of the optical characteristics of the techniques, with the 4X objective being used as detection and an effective $M_{ill} = 2.5$. This experimental configuration results in an effective DMD pixel of $e = 2.14\,\mu m$ which, considering N = 64 patterns, leads to a modulated volume thickness of $\Delta z = N \cdot e = 134\,\mu m$.

The reconstruction procedure was carried after measuring a sub diffraction sample, namely fluorescent beads, embedded in a transparent, solid gel matrix (1.5% phytagel in distilled water). The beads were of average diameter of $500\,nm$, with peak emission at $\lambda_{em} = 582\,nm$ and central excitation peak at $\lambda_{exc} = 480\,nm$. Being the last illumination lens of $NA_{ill} = 0.14$ and that of detection with $NA_{det} = 0.13$, these two altogether grants a lateral resolution (i.e., on the xy plane) of $\Delta\rho = \frac{\lambda_{em}}{2 \cdot NA_{det}} = 2\,\mu m$ and an axial profile dominated by the imaged pixel size e.

After a complete measurement set, an inversion problem is solved, aimed at retrieving the fluorophores spatial distribution over a volume $\Delta X * \Delta Y * \Delta Z$. It is hereby denoted as effective volume depth ΔZ, which is different compared to the modulation thickness Δz, due to the defocus given by the detection PSF. An example of complete reconstruction is shown in Figure xxv.

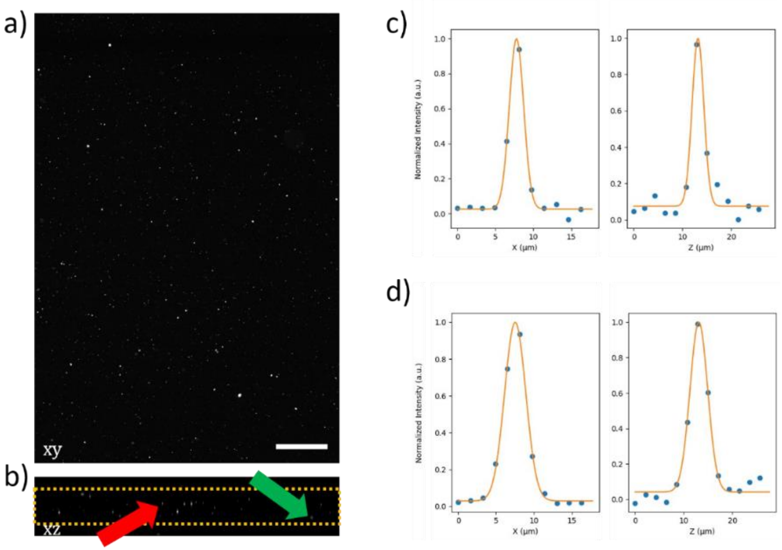

Figure xxv: Reconstruction on fluorescent beads. Scale bar is 100 µm. (a) Reconstructed single plane (xy). (b) Transverse view (xz). The volume with resolution of $\pm\sqrt{2}\,\delta r$ *laterally and* $\pm\sqrt{2}\delta z$ *axially, is highlighted in the yellow box. (c) Diffraction limited intensity profile along x and z (red arrow). (d) Same profiles for a bead at the border of the imaging region (green arrow).*

Here, diffraction limited lateral resolution is obtained on the entire extension of the sensor (*xy* in Figure xxv). Conversely, a diffraction limited axial profile is only obtained in the central region of the detection DOF, represented as a yellow box. A gaussian fit has been performed to retrieve the experimental feature of the reconstruction of the central part of the volume, leading to a measured, lateral resolution of $\delta\rho = 2.3 \pm 0.2\ \mu m$ and an axial resolution of $\delta z = 2.9 \pm$

$0.2\,\mu m$. This parameters are in agreement with the presented theoretical values. However, by considering a bead which is not perfectly in focus with respect to the detection lens, this last parameter worsen, as anticipated. Nonetheless, by considering a region in which the transverse resolution is $\sqrt{2}\,\delta z$, this holds an overall imaging volume of $\Delta X = \Delta Y = 3.3\,mm$, limited by the sensor size and $\Delta Z = 120\,\mu m$.

In the case where no translating stage is considered, the reconstruction volume would be further constraint by the illumination divergence profile. This would limit ΔX to be about one tenth of its final extension. Moreover, this situation would thus result in an elongated image region, with a mms extension only along *y.* Accordingly, with no illumination objective translation, narrow samples have been studied: to well fit the elongated reconstruction region. To this aim *Danio rerio* embryos have been extensively used for the characterisation of the technique, without lateral extension. Nevertheless, the results obtained and the conclusions inferred are not dependent upon such extension and have to be intended as generic.

A comparison between the two situations, with and without lateral extension, is presented in Figure xxvi. Here, it is clear by comparing Figure xxvi a) and b), how in the latter, the whole sensor perceives the fluorescence signal from the plane of interest. Orthogonal reslices of the two situations are also displayed in panels c) and d), with the region of correct reconstruction highlighted in the green box: the whole volume is populated by fluorescent beads that, with no extension, would have been almost impossible to be correctly reconstructed. Nonetheless some peripherical nanosphere can still be sensed in panels a) and c), due to the tails of high diverging illumination beam exciting some brighter emitters. The results yielded by the two procedure are equivalent in the central region.

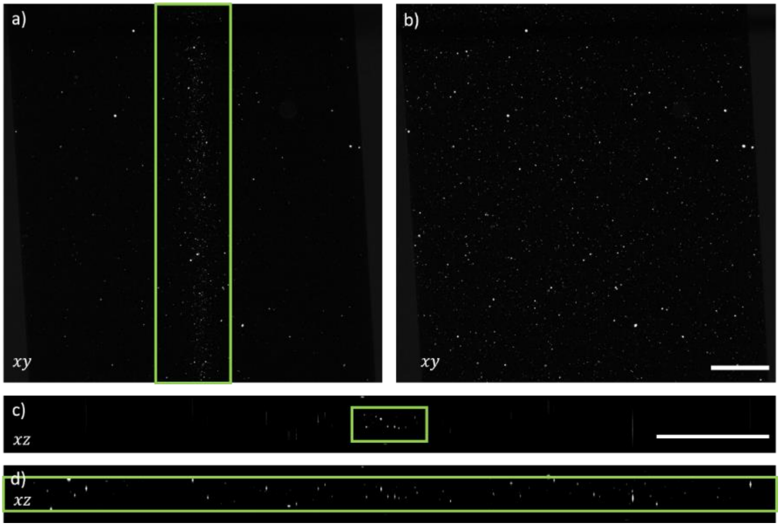

Figure xxvi: Reconstruction provided by the technique with and without lateral extension, a) and b) respectively and their related reslices. Scale bars are 500 µm.

3.1.3 Measurement design

The previous sections presented both the different possible choices of measurement functions and the importance of said choice. This in fact may imply the success of the under sampled reconstruction, as well as the SNR of the retrieved solution. A "good" set of sampling function is that which maximizes the incoherence with the signal (or its representation) (see Appendix D for further details). By considering spatially sparse fluorophores distribution, the representation basis W can be considered as the identity matrix. This means that for fluorescent beads the canonical spatial basis is the basis with which Φ must show an high degree of incoherence.

Due to the hardware components involved in the presented setup, a good candidate is the so-called Walsh-Hadamard (WH) basis, previously introduced in chapter 1. Each element of this set only shows either +1 or -1 entries, which can be easily encoded on a Spatial Light Modulator working in binary mode. However, DMDs can produce only positive entries. Thus, it is needed a workaround to show the -1 entries. To this aim, in [79] it is presented a possible solution, which consists in splitting each of the WH element into two matrices, starting from the formulation presented in the first chapter:

$$H_n = \begin{bmatrix} H_{n-1} & H_{n-1} \\ H_{n-1} & -H_{n-1} \end{bmatrix}$$

$$H_n = H_{P_n} - H_{N_n} = \begin{bmatrix} H_{n-1} & H_{n-1} \\ H_{n-1} & 0 \end{bmatrix} - \begin{bmatrix} 0 & 0 \\ 0 & H_{n-1} \end{bmatrix}, \qquad 3.2$$

where it has been considered a n-dimensional space of measurement for simplicity. Thus, problem Eq. 3.1 can be generally recast as:

$$\boldsymbol{\xi} = H \cdot \boldsymbol{\chi} = (H_P - H_N) \cdot \boldsymbol{\chi} = \boldsymbol{\xi}_p - \boldsymbol{\xi}_N. \qquad 3.3$$

Therefore, a single WH matrix measurement can be represented equivalently by two consequent measurements. The first, corresponding to the matrix H_P, which outputs the measured vector ξ_p, the second, related to H_N, which determines the vector ξ_N. Finally, to retrieve the total measured vector ξ, ξ_N is subtracted to ξ_p to mimic the negative entries of the DMD.

Considering N modulation pixels, which is calculated according to the illumination and detection features, the dimensionality of the measurement set is determined. Furthermore, this also leads to a total number of patterns to be acquired of $2N$.

3.1.4 Compressed Sensing in sm-SVIM

LSFM and sm-SVIM are formally equivalent as imaging problem. The two measurements routines have a characteristic sampling matrix which in the first case, provides a one-to-one correspondence between imaged plane and acquired frame, while in the second, it mixes the depth information according to the modulation pattern. Therefore, in sm-SVIM the acquired signal is the weighted sum of different contributions collected from different planes.

In LSFM, to sample a volume of N planes, N frames must be acquired, thus the corresponding matrix can be represented as an identity matrix. Conversely, sm-SVIM encodes information through a measurement process which has also nonzero off diagonal elements in its matrix form, according to the family of pattern chosen (as presented in the first chapter). Nonetheless, volumetric light modulation enables the use of Compressive Sensing. CS might further improve the technique performances in terms of acquisition time and induced photodamage.

The so formulated reconstruction problem takes the form (where the pixelwise dependence has been omitted for simplicity):

$$\boldsymbol{\psi} = \operatorname{argmin}\left(\frac{1}{2}\|\boldsymbol{\xi} - \Phi \mathrm{W}\boldsymbol{\psi}\|_{l_2}^2 + \lambda \mathrm{R}(\boldsymbol{\psi})\right) \ s.t. \boldsymbol{\chi} = W\boldsymbol{\psi}, \quad 3.4$$

where $\boldsymbol{\psi}$ is the signal transformed in the domain pointed by the linear map W, λ is an hyperparameter for regularisation of the solution, already discussed, and $\mathrm{R}(\boldsymbol{\psi})$ is a term which can enforce some features in the solution. This penalty term is of great use and variability, since it can enforce sparsity in the signal itself, as in the case of $\mathrm{R}(\boldsymbol{\psi}) = \|\boldsymbol{\psi}\|_{l_1}$, or it can provide for sparsity in the image gradient, $\mathrm{R}(\boldsymbol{\psi}) = \|TV(x)\|$, considering its l_1 or l_2 norm [37].

In this context, being the unknown fluorophores distribution $\boldsymbol{\chi}$ sparse in a domain mapped by the linear transform W, it holds that said signal recovery might happen without consistent loss of information if the measurement matrix Φ and the representation matrix are mutually incoherent [36]. Therefore, the choice of these matrices is crucial for both compression and reconstruction capability. To this extent, an evaluation of the compression capability can be given by defining a compression factor, which is commonly define both as $CR = 1 - M/N$, given in percentual units, or as

$CR = N/M$. This means that the fewer the measurements, the higher the compression ratio.

Analogously to what have been done for optical features of the complete reconstruction procedure, also the compression capability of the technique has been tested of sub diffraction beads, as displayed in Figure xxvii. Here, different compression ratios have been tested and are reported results both in lateral xy and axial xz reslices. Comparable results with respect to the non-compressed reconstruction are obtained for CR of 50% and 75%, which are degraded in terms of overall SNR. At higher ratios, namely 87.5%, the undersampled problem fails at recovering spatial information over the entire volume of interest. This might result in either a wrong position along the z axis or in a false duplicate in the point emitter, as highlighted by the arrows in figure.

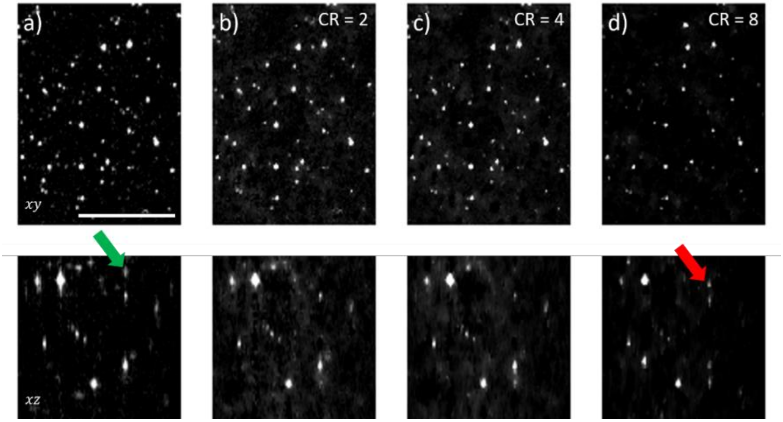

Figure xxvii: Compressed volumetric reconstruction quality in a fluorescent beads sample at different under sampling ratio, namely 2, 4 and 8 or equivalently 50%, 75% and 87.5%. Scale bar is 100 µm [28].

Nonetheless these latter results demonstrate how CS can be beneficial to imaging in microscopy and more in particular to sm-SVIM, potentially decreasing the light dose shining the sample (and therefore the phototoxicity of the technique) and the overall acquisition time, at cost of a limited loss of information.

3.2 AXIAL VOLUME EXTENSION

3.2.1 Pattern Binning

A possible experimental trick can be performed to enlarge to reconstructed volume along the axial direction. When measuring a sample with N acquisition patterns, this results in $2N$ effectively stored patterns in the DMD volatile memory. Given a limited $2 * 48 \text{ MB}$ of memory storage for firmware and patterns in fact, it follows that only a limited number of these can be of use. Once decoded, the DMD memory stores about 400 frames, which limits the sampling set to be at maximum $N = 128$ and the modulated volume to be $\Delta z = N \cdot e$.

To overcome this issue, they also have been tested a set of measurement patterns in which the tiniest degree of modulation are two lines of pixels, instead of just one. This intrinsically doubles the modulated volume since $\Delta z = N \cdot 2e$, at cost of also doubling the axial resolution of the reconstruction. This approach has proven to be very effective in situation in which the detection depth of field is strongly elongated, as in the case for the presented 2X objective. Furthermore, it has also been tested a binning of 4, which conversely has shown weak modulation capability.

Despite this happened in a region well beyond the DOF. Therefore, mainly binning by a factor of two has been considered and exploited.

3.2.2 Deconvolution

Whenever one wants to apply a deconvolution algorithm, a fundamental step is the Point Spread Function evaluation procedure: a correct estimate of this function strongly affects the resulting reconstruction. In Light Sheet Fluorescence Microscopy, the overall PSF of the technique is given by two contributions, the illumination, and the detection PSF. The final function is thus given by the spatial contribution of these two, having an axial profile which is limited by the light sheet thickness, as illustrated in Figure xxviii. Furthermore, in LSFM, the illuminated sample and the sensor plane are mutually static, meaning that the acquired frames are always in focus with respect to the detection.

Conversely, in the technique presented in this thesis, the overall PSF shows some differences with respect to said features. In sm-SVIM in fact light is modulated according to a well determined pattern, which results in different incoming light profiles, which are of different thickness and axial position. In the case of Walsh-Hadamard modulation, said thickness varies from the minimum value of the DMD pixel dimension, to its maximum for the first basis component of the measurement set, i.e., a continuous light profile which extends over the N pixels of modulation. As displayed in Figure xxix the incoming modulated profile overlaps with the detection PSF at different depth on the z axis, resulting in imaged regions with different defocus contribution. From a practical point of view, the farther away the fluorophore from the DOF centre, the more blurred its acquisition.

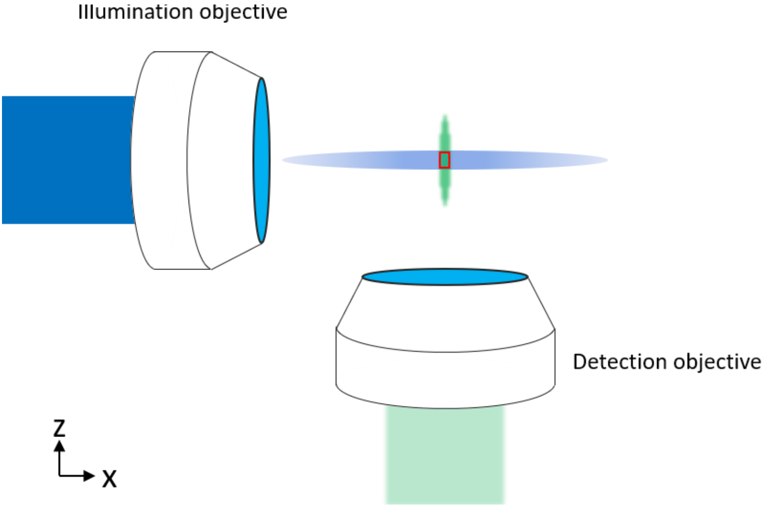

Figure xxviii: Schematics of imaging a light-sheet setup. The highlighted region is the resulting PSF, which is the convolution between the illumination and the detection PSFs.

Given the modulation of the illumination profile, it follows then for each pattern, an effective illumination PSF must be considered.

Then, it is possible to mathematically formulate the process of image formation in sm-SVIM, to finally be able to solve for a diffraction limited object distribution over the entire volume of imaging. To ease said task, the detection PSF has been considered to be constant at any given plane. To rephrase, each of the camera active elements senses a contribution of light which only depends upon the object volume distribution.

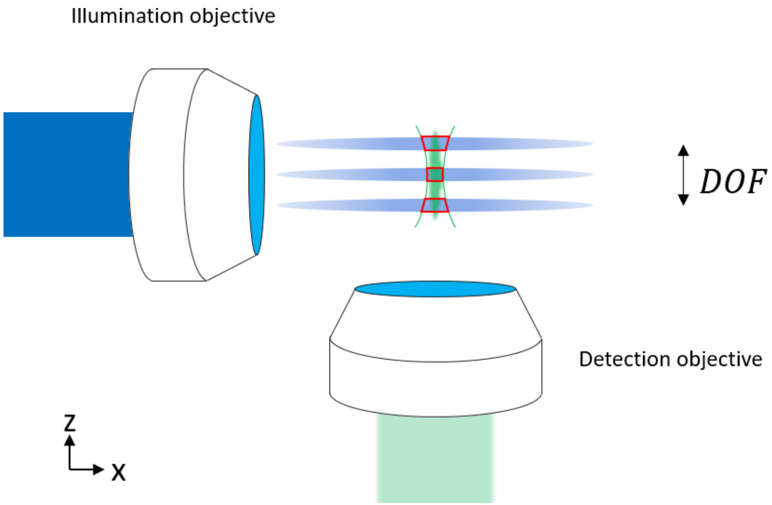

Figure xxix: Schematics of imaging a sm-SVIM. The highlighted region is the resulting, modulated PSF, which is the convolution between the patterned illumination profile and the detection PSFs. Different axial position corresponds to different defocus contribution.

In the illumination path, the axial light distribution depends on the illumination pattern projected at the DMD plane, which is one row of the measurement matrix, i.e., $\boldsymbol{\phi}_j(z)$. As previously mentioned, it is hereby considered a sampling set of Walsh-Hadamard functions, so that $\boldsymbol{\phi}_j(z)$ is its j^{th} vector row. Said vector, only shows binary entries which result in a binary axial illumination which selectively illuminates the volumetric sample at different depths. Thus, by knowing $\boldsymbol{\phi}_j(z)$, the overall collected signal $\boldsymbol{\Omega}(x,y,z)$ will depend on both the excited volume, and on the fluorophores volumetric distribution, by a simple dot product:

$$\boldsymbol{\Omega}(x,y,z) = \boldsymbol{\phi}_j(z) \cdot \boldsymbol{\chi}(x,y,z). \tag{3.5}$$

From Eq. 3.5, it can be calculated a mathematical formulation of the imaging of $\boldsymbol{\Omega}(x,y,z)$ performed by an optical system with detection Point Spread Function PSF_D:

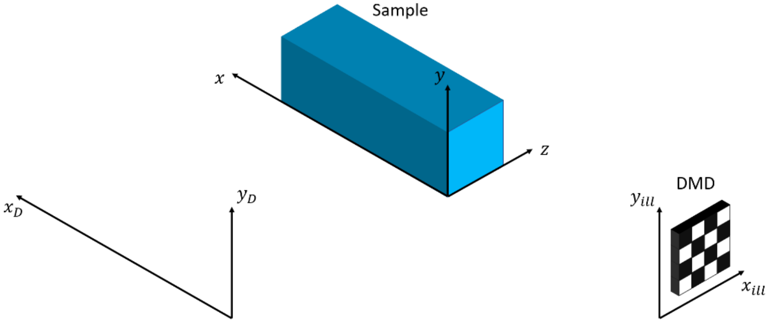

Figure xxx: Modulation scheme in 3 dimensions.

$$\begin{aligned} \mathbf{I}(x_D,\, y_D) &= \iiint \boldsymbol{\Omega}(x,y,z) \cdot PSF_D(x-x_D, y-y_D, z)\, dxdydz \\ &= \int \boldsymbol{\Omega}(x_D,y_D,z) \otimes_{x_D,y_D} PSF_D(x_D,y_D,z)\, dz \end{aligned} \tag{3.6}$$

And consequently, the final formulation for the detected image is:

$$\mathbf{I}(x_D,\, y_D) = \int \Big(\boldsymbol{\phi}_{\mathrm{j}}(z) \cdot \boldsymbol{\chi}(x_D,y_D,z)\Big) \otimes_{x_D,y_D} PSF_D(x_D,y_D,z)\, dz. \tag{3.7}$$

By considering a symmetric PSF with respect to z, it is possible to consider its effective representation. Furthermore, the binary entries of $\boldsymbol{\phi}_j(z)$ are such that the pointwise product $\boldsymbol{\phi}_j(z).\boldsymbol{\phi}_j(z)$ is equal to $\boldsymbol{\phi}_j(z)$. Altogether these two considerations lead to:

$$\mathbf{I}(x_D,\, y_D) = \int \left(\boldsymbol{\phi}_j(z)\cdot\boldsymbol{\phi}_j(z)\cdot\boldsymbol{\chi}(x_D,y_D,z)\right) \otimes_{x_D,y_D} PSF_D(x_D,y_D,z)\, dz =$$

$$= \int \left(\boldsymbol{\phi}_j(z)\cdot\boldsymbol{\chi}(x_D,y_D,z)\right) \otimes_{x_D,y_D} \left(PSF_D(x_D,y_D,z)\cdot\boldsymbol{\phi}_j(z)\right) dz = \qquad 3.8$$

$$= \int \left(\boldsymbol{\phi}_j(z)\cdot\boldsymbol{\chi}(x_D,y_D,z)\right) dz \,\otimes \left(\int PSF_D(x_D,y_D,z)\cdot\boldsymbol{\phi}_j(z) dz\right),$$

where the spatial dependency of the convolution has been neglected. Every acquired frame is in fact given by a line integral of the PSF, which is plane wise considered to be isoplanatic. Finally, the image formation in sm-SVIM can be modelled as:

$$\mathbf{I}(x_D,\, y_D) = \int \left(\boldsymbol{\phi}_j(z)\cdot\boldsymbol{\chi}(x_D,y_D,z)\right) dz \,\otimes PSF_{D_{Eff}} \qquad 3.9$$

To retrieve the modulated image, i.e., before that the measurement inversion takes place, a Richardson-Lucy [8] deconvolution algorithm is applied, whose step is represented as:

$$\widehat{\boldsymbol{\Omega}}^{(t+1)} = \widehat{\boldsymbol{\Omega}}^{(t)}\left(\frac{\mathbf{I}(x_D,\, y_D)}{\widehat{\boldsymbol{\Omega}}^{(t)} \otimes PSF_{D_{Eff}}} \otimes PSF_{D_{Eff}}{}^{*}\right). \qquad 3.10$$

To perform deconvolution before inversion makes the problem more resilient with respect to the noise induced by the two inversions.

As a final remark, to deconvolve a $2048 * 2048 * 128$ volume with a $128 * 128$ $PSF_{D_{Eff}}$, over 30 iterations of the algorithm, it takes about $2\ min$. The code was run in parallel on a TITAN RTX.

4 RESULTS AND CONCLUSIONS

The goal of this final chapter is to show the results obtained by the developed technique in terms of imaging capability and optical sectioning, compressibility and image quality achieved through deconvolution. The imaged specimens were biological samples, *in vivo* and *ex vivo*, of different sizes and fluorescent labels.

In the first part they are presented results obtained with a complete measurement set, to assess for optical sectioning capability of sm-SVIM to establish a comparison with LSFM.

Then, they are described the compression results in samples of different spatial features, with a particular regard to experimental artefacts induced by photobleaching, which might affect the final reconstruction.

Moreover, a discussion on the deconvolution algorithm is proposed. Also, multicolour reconstructions are reported, even though this strategy has not been extensively studied and tested.

Finally, the conclusions of the thesis work are drawn, also highlighting possible future implementation for sm-SVIM.

4.1 RESULTS

4.1.1 Volume Reconstruction

Different samples imply different volume of interest. Thus, in the next sections they are presented results obtained with different illumination and detection lenses, according to the wanted reconstruction volume. In this section nonetheless, just non-compressed reconstructions are examined.

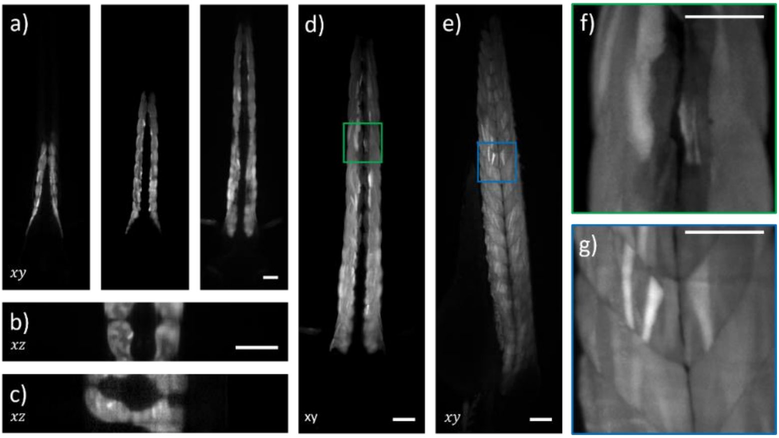

Figure xxxi: Reconstruction of a Tg (α-actin: GFP) zebrafish embryos. Scale bars are 100μm. (a) Plane by plane reconstruction at different depth: z = 0, z = 67μm, z = 134μm, from left to right. (b, c) Transverse sections of the sample acquired in frontal and sagittal positions. (d) Frontal Maximum Intensity Projections (e) Sagittal Maximum Intensity projection. (f, g) Details of the regions shown in the green and blue boxes. [28]

The first test bench for the technique and its capability to perform *in vivo* volumetric imaging have been 4-day post fertilisation living *Danio rerio* embryos, with two different tags: Tg (α-actin: GFP) and Tg (kdrl: GFP). These two genetic labels were so that GFP is expressed in the skeletal muscles and endothelial cells, respectively. For samples highly elongated along one direction as zebrafishes embryos, the same configuration as that presented for the bead's characterisation is used, providing a reconstructed volume of $\Delta X * \Delta Y * \Delta Z = 200\,\mu m * 3.2\,mm * \ 120\,\mu m$, with no need for lateral extension. A complete Walsh-Hadamard measurement set of $N = 64$ was exploited. The reconstructed anatomy of an entire zebrafish embryo is shown in Figure xxxi. The sample of interest expresses fluorescence in the muscle's fibres, which can be clearly distinguished over the entire specimen, both in lateral and transversal projections. A measurement routine with the same parameters has been also tested on Tg (kdrl: GFP) embryos, where the fluorescent signal shows different spatial features: here in fact, the blood vessels are genetically labelled. The reconstruction of such samples is shown in Figure xxxii: sm-SVIM acquisition protocol leads to an imaged volume where the vascular network is almost everywhere isotropically, from the brain to its trunk-tail region. The presented reconstructions were carried after a single frame exposure of $50\,ms$, $100\,ms$ for equivalent Walsh-Hadamard pattern, leading to an overall acquisition of $6.4\,s$.

As anticipated, one major requirement of the technique is having a motionless sample, not to further modulate the incoming fluorescent signal. To this end, the presented zebrafish embryos were anesthetized in tricaine 0.1% and were kept in a Fluorinated Ethylene Propylene (FEP) tubes [111]. In regions in which motion of the sample tissue is necessary, as for the beating heart, blurring artifacts are produced. Nonetheless such movement-related artefacts did not affect the overall quality of the reconstruction (Figure xxxii).

Despite the two volumetric distributions of signal are different in Tg (α-actin: GFP) and Tg (kdrl GFP) embryos, it holds for both that sm-SVIM is a suitable tool for the volumetric acquisition, without incurring in shadowing artifacts or motion of these samples.

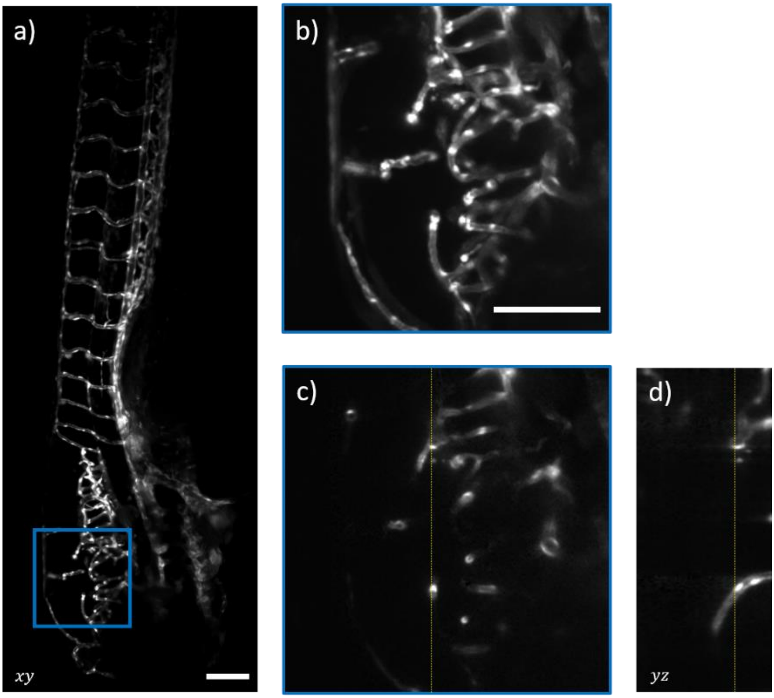

Figure xxxii: sm-SVI acquisition of a Tg (kdrl: GFP) zebrafish embryos. Scale bars are 100µm. (a) Maximum Intensity Projection of 3D reconstruction of the trunk and head region. (b) Detail of the blue box. (c) Single sagittal plane (d) Single frontal plane. The yellow lines indicate the corresponding position in the sagittal and frontal planes. [28]

To evaluate the quality of complete reconstruction, the technique has also been tested over larger volumes. As previously described, this has been obtained thanks to the motion of the illumination lens. Moreover, the DMD modulating surface must illuminate the whole volume of interest. This implies a lower magnification objective in illumination.

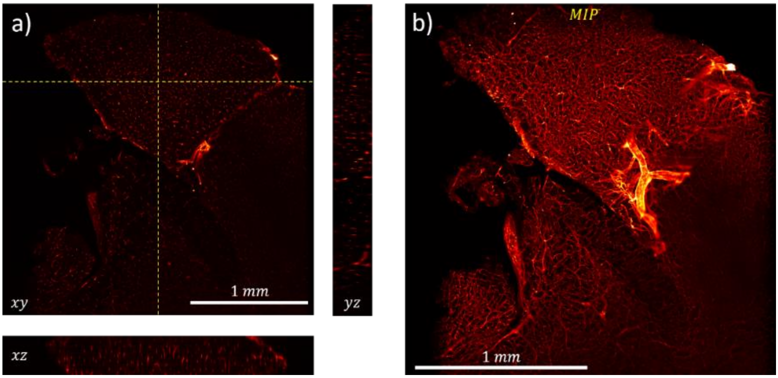

Figure xxxiii: Reconstruction of part of a mouse brain. In a) a single restored plane is shown together with its sagittal and frontal projection, whose location is highlighted by the yellow, dashed lines. b) Maximum Intensity Projection of the recovered volume.

In Figure xxxiii it is reported a portion of a mouse brain, in which the blood vessels were tagged with CY5, a fluorescent molecule that emits fluorescence at around 670 nm upon being excited at 630 nm. The brain tissue was cleared in BABB. The sample was acquired with a measurement set consisting of 128 Walsh-Hadamard patterns, with M_{ill} = 4X and NA_{ill} = 0.13 and M_{det} = 5X and NA_{det} = 0.14, respectively. This result in a reconstructed volume of $\Delta X * \Delta Y * \Delta Z = 2.67\ mm * 2.67\ mm * \ 120\ \mu m$. The brain vasculature is successfully retrieved (Figure xxxiii, Maximum

Intensity Projection on the rightmost panel), displaying an almost isotropic resolution over lateral and transversal planes.

A trial for binned acquisition patterns has also been performed, as shown in Figure xxxiv. Here, brain slices of mice were imaged in Ethyl Cinnamate, after being labelled with a fluorescent probe called TOPRO ($\lambda_{exc} = 630\,nm$, $\lambda_{em} = 660\,nm$). Imaging was performed with M_{ill} = 4X and NA_{ill} = 0.13 and M_{det} = 5X and NA_{det} = 0.14, respectively, resulting in a lateral view of $\Delta X = \Delta \mathrm{Y} = 2.67\ \mathrm{mm}$ and a modulation axial extension $\Delta z = N * 2 * e = 343\,\mu m$, which extends well beyond the detection Depth Of Focus as shown in the transverse detail of Figure xxxiv: the pointy signal can be perceived only in the central modulated region.

As a final example, the maximum detectable volume was imaged, in a brain tissue with the same label and imaging medium as the sample in Figure xxxiv. The imaging was obtained with M_{ill} = 2X and NA_{ill} = 0.055 and same characteristics detection lens, resulting in a lateral view of $\mathit{\Delta X} = \mathit{\Delta Y} = 6.67\,mm$ and a modulation axial extension $\Delta z = N * 2 * e = 687\,\mu m$, Figure xxxiv.

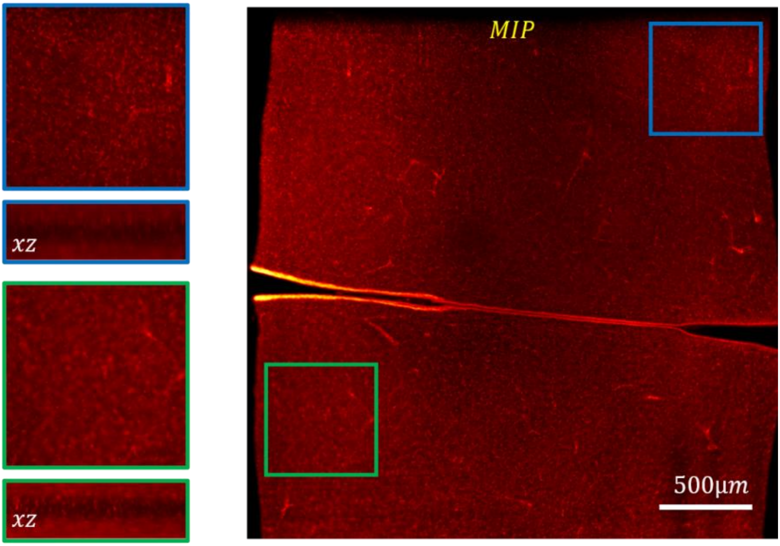

Figure xxxiv: Reconstruction of part of mouse brain. Maximum Intensity Projection of the Imaged volume. The two boxes point two regions which are displayed in the leftmost panels together with their orthogonal reslice: here the defocus effect is clear.

These last presented cases of interest were acquired with a single frame acquisition time of $300\,ms$, yielding an effective exposure time per pattern of $600\,ms$, and an overall measurement time of $38.4\ s$.

Finally, thanks to final spatial arrangement implemented, a second LED source was used for multicolour imaging: results are reported in Figure xxxvi. This assesses for the capability of performing sm-SVIM measurements on a variety of differently labelled samples without need for modification in the microscope. The lenses used are M_{ill} = 4X and NA_{ill} = 0.13 and M_{det} = 5X and NA_{det} = 0.14, with Ethyl Cinnamate as immersion medium.

However, the analysis of this approach is limited to fully sampled reconstruction routines.

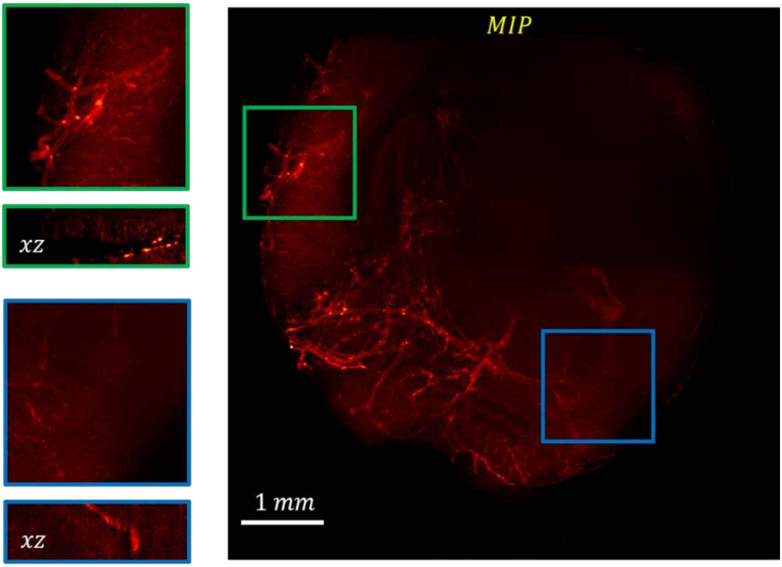

Figure xxxv: Reconstruction of part of mouse brain. Maximum Intensity Projection of the Imaged volume. The two boxes point two regions which are displayed in the leftmost panels together with their orthogonal reslice.

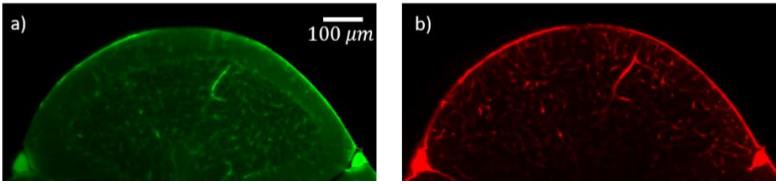

Figure xxxvi: Multicolour reconstruction of the same plane in a multilabel sample.

4.1.2 Compression

Once the optical sectioning of sm-SVIM has been proven, the same had to be done for the compression capability of the technique. For this reason, both zebrafish embryos and mouse brain portions were acquired and reconstructed by solving an undersampled problems at different compression ratios. Due to the spatial sparsity of the fluorophores distribution in the investigated samples, the ill-posed problem of Eq. 3.4 can be recast as:

$$\operatorname{argmin}\left(\frac{1}{2}\|\boldsymbol{\xi}-\Phi\boldsymbol{\psi}\|_{l_2}^2+\lambda\|\mathrm{TV}(\boldsymbol{\psi})\|_{l_1}\right). \qquad 4.1$$

In Eq. 4.1, the representation matrix W has been considered as the identity matrix, I. Furthermore, problem 4.1 is suitable in recovering signals with smooth transitions and a small number of few sharp edges, as a blood vessels net.

Firstly, a CS reconstruction has been carried on Tg (kdrl: GFP) zebrafish embryos, with increasing CR of 2, 4 and 8, respectively. As displayed in Figure xxxvii, at lower CRs the differences in the overall reconstruction are negligible. Nonetheless, as the starting measurement set shows fewer entries, loss of volumetric information occurs, as highlighted in the details panel: the reconstructed blood vessels, despite being fully visible, appear to be more blurred, as their fluorescent signal comes from a less axially localized region. This confirms what was also remarked by compressed reconstructions on beads. The loss of information becomes clearly visible at CR = 8, were the vessels crossing highlighted is almost not perceivable. Due to loss of different axial components, this results in a mixed contribution of different modulation planes. Nevertheless, most of the embryo vasculature is well preserved over the imaged volume, at cost of losing axial sectioning. Furthermore, the rightmost panel of Figure xxxvii shows a reconstruction obtained using only one eighth of the starting measurement set, yielding a remarkable reduction both for light dose and total acquisition time. Furthermore, an analogous reconstruction procedure was performed on a sample equivalent to that presented in Figure xxxiii: the compressed reconstructions of a limited portion are shown in Figure xxxviii.

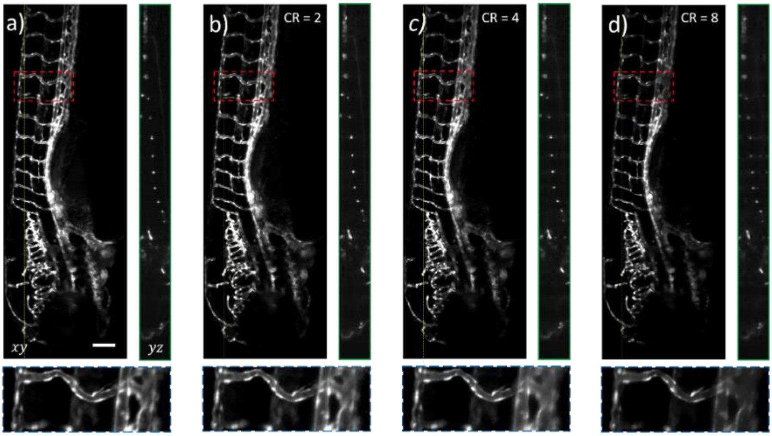

Figure xxxvii: Compressed volumetric reconstruction in a Tg (kdrl: GFP) zebrafish embryo at different under sampling ratio C. Scale bars are 100μm. Maximum intensity projection (left hand side of each panel) and single frontal plane (right hand side). The yellow line highlights the plane shown on the right-hand side. The red box is a detail of the Maximum Intensity Projection, for each panel. From left to right: reconstruction from complete Scrambled Hadamard measurement set and for compressing ratio of 2, 4, 8. [28]

Once again, the obtained results confirm what achieved in synthetic beads and zebrafish embryos: the higher the compression, the bigger the loss of information along the axial direction, which is the modulation axis. In the transverse sections, f) g) and h), the loss of information as CR increases is clear, as pointed by the arrow: vessels which were axially resolved at CR = 2 and 4, are immersed in background noise at CR = 8. Moreover, also the defocus effect induced by the detection DOF seems to be worsened: a good reconstruction is reported over thinner volumes for increasing CR.

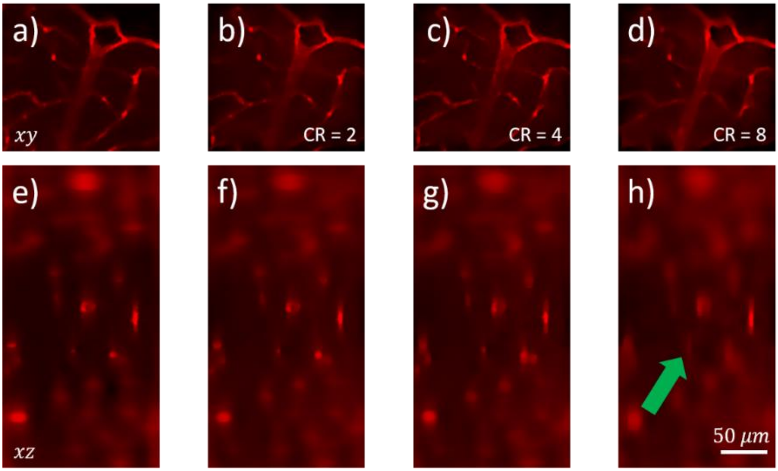

Figure xxxviii: Compressed reconstructions at increasing CRs. a) and e) are non-compressed reconstruction of a plane and its orthogonal projection; b) and f) are the same planes recovered with CR = 2. Same holds for the pairs c) g) and d) h), but at CR = 4 and CR = 8, respectively. Increasing the compression ration correspond to an higher probability of failing at axially relocating the signal, as pointed by the green arrow.

As explained, the undersampled sets were obtained by extracting at random the frame entries used for the ill-posed reconstructions. In these situations, there is no preference on the selected axial frequencies. However, by choosing the frames for the CS problem in a non-random extraction, the recovery might happen with lower information losses on the fluorophores axial distribution. It is in fact true that, for the presented samples, an higher amount of information hides in the lower frequency components.

Nonetheless, the two reported cases of interest show how CS can be beneficial in an axially modulated setup with incoherent illumination, by critically reducing the number of images to be acquired for a volumetric reconstruction. Altogether, they demonstrate how the technique yields a gentle imaging approach, reducing the caused photodamage and equivalently shortening the total measurement time.

4.1.3 Photobleaching Artefacts

An unwanted signal modulation perceived by the sensor might result in an unwanted reconstruction artefact. That might be the case for a non-uniform illumination spot of the DMD plane or, as of interest for this paragraph, for photobleaching. As presented in Appendix B, photobleaching is a phenomenon which may occur when overexposing the fluorescent probe to light. Photobleaching causes a permanent transition of the molecules from a fluorescent state to a non-emitting one also referred to dark state. Photobleaching in an extended sample may result in an exponential decrease of the fluorescent signal over time.

The described exponential modulation has ben also measured in some sm-SVIM measurements, where, together with patterned modulation, it is introduced a further modulation factor as an exponential decay (Figure xxxix b)). Said modulation makes the inversion problem time dependant, since it links higher modulation frequencies (i.e., the tiniest degree of axial information) to frames of lower intensity. As the measurement with a Walsh-Hadamard set proceeds, the finest degree of modulation decreases as a power of two, down to $2^0 = 1$, which corresponds to a single line or down to two lines for binned patterns. By coupling patterned modulation with an exponential decay, this results in a volume reconstruction which is axially affected by this coupling. In Figure xxxix c) it is shown a transverse reslice in which line artifacts arise, denoting different intensities on regions which were acquired at different time, i.e., at different bleaching levels. The strongest of these artifacts is highlighted by the yellow arrow in the figure and corresponds to the centre of axial modulation.

To correct for this factor, two strategies may be taken. The first is modulating the sample with random or scrambled Walsh-Hadamard basis, so to distribute over the reconstructed volume randomly and evenly, the exponential decrease of the detected signal. The second, which is the one reported in this thesis, consists of compensating for the known exponential modulation and to rescale the acquired frames by a factor $\frac{I(t)}{\exp{(-kt)}}$, with time being discretized by the patterning. The corrected result is reported Figure xxxix d). Here, no axial modulation of the reconstruction is reported, proving the efficacy of the correction.

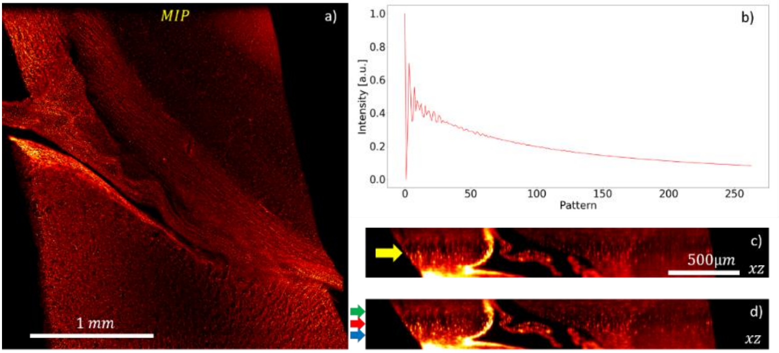

Figure xxxix: a) Maximum Intensity Projection of a deconvolved, reconstructed volume. b) Intensity profile along the time i.e., patterned acquisitions. c) Reslice of the reconstruction in which photobleaching has not been considered; d) Same reslice but where a correcting factor has been used. Here artifacts are successfully removed.

Finally, this demonstrates how it is critical to have collected raw frames which differ only due to the different illumination patterns, without no other modulation induced. This could critically affect the final reconstruction, to the same extent as a moving sample or a non-uniform illumination profile, either in space or time.

4.1.4 Deconvolution

Similarly to what it has been proposed for optical sectioning and compressed routines, also deconvolution has been tested on biological samples, namely on cleared mouse brain slices, imaged in Ethyl Cinnamate. The data on which deconvolution has been applied are those shown in Figure xxxix. A sample with pointy features has been chosen to ease the evaluation of the algorithm performances.

By using a 4X illumination objective with modulation patterns binned by a factor of 2, this led to an overall modulation extension of $\Delta z = 343\ \mu m$. The signal was then acquired by a 5X objective, whose DOF had an extension much smaller compared to Δz, as displayed in the orthogonal reslice details panel of Figure xxxix.

As described in 1.1.3, deconvolution approaches need a PSF, experimentally or computationally obtained, to infer information about the sample spatial distribution, or in this case, about the modulated sample distribution. In this thesis, the detection PSF was obtained by theoretical simulation, without considering aberrations. The output of said simulation was a volume with the same axial extension as those given by the experiments. Because of the symmetry of the problem, this has been decoupled as formulated in Eq. 3.7, in which the rightmost term is given by considering an effective PSF. Said effective function arises from the symmetry of the family of patterns used, the Walsh-Hadamard set, and their illumination profile $\boldsymbol{\phi}_j(z)$.

A plane wise Richardson-Lucy algorithm has been then applied, in an entire acquired modulated volume: the results are reported in Figure xl. The planes displayed are those at the depths indicated by the arrows in the orthogonal reslice of Figure xxxix d). Three planes of interest have been chosen symmetrically with respect to the centre of the Depth Of Focus, at $z = -100\ \mu m, 0\ \mu m, 100\ \mu m$, respectively .

The comparison between the two intensity profiles evaluated on the straight lines of panel a) b) and c), both of the deconvolved inversion and the simple inversion, are plotted in Figure xl d) e) and f), respectively. In the three planes of interest, deconvolution has proven to be effective in increasing the image contrast altogether with a sharpening of the pointy emitters, which is evident in central volume of reconstruction. However, the farther away from the focus, the more the deconvolved profile look like being processed more by a denoise algorithm, rather than a deconvolution. This might be caused by errors in the simulated PSF which does not consider real factor as refraction as well as aberrations which might arise from the optical glass-imaging medium interface. Furthermore, restored images might include artifacts which are strongly related to the PSF used and the algorithm applied. To this extent, PSF is critical to the performance of iterative approach, as for this Richardson-Lucy algorithm of interest.

Nonetheless deconvolution has proven to be beneficial to the imaging quality, improving contrast and increasing SNR in region well beyond the DOF of the detection objective.

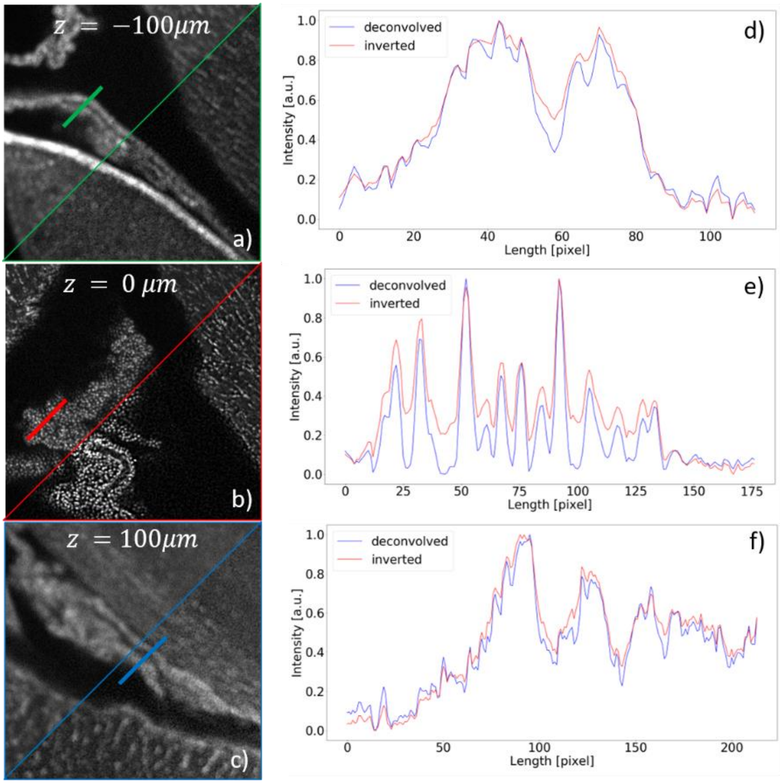

Figure xl: Deconvolution performances in a reconstructed volume: the top left corner image in a), b) and c) comes from reconstructed planes at z = -100 μm, 0 and 100 μm respectively, while the lower right corner is the deconvolved counterpart. d), e) and f) are the line plot of the intensity along the paths in a), b) and c). The contour colours represent the depth with respect to Figure xxxix.

4.2 CONCLUSIONS

In this work it has been investigated how to implement a compressed acquisition protocol in a LSFM context. This led to the development of sm-SVIM, which obtains volume information about the three-dimensional distribution of fluorescent samples by selective axial modulation.

The optical scheme of the proposed technique involves two hardware components to obtain modulated, incoherent illumination, namely a Spatial Light Modulator (DMD) and an LED, which, by efficiently collecting its high diverging radiation, provides a strong reduction of the shadowing artefacts, which are a fingerprint of LSFM. Together with reduced artefacts, incoherent sources are beneficial in terms of lower cost, wide colour availability and output power stability.

Furthermore, the use of a Spatial Light Modulator opens the possibility to exploit compressed acquisition protocols as Compressed Sensing. In the presented work, compressed reconstructions of both synthetic and biological samples have been demonstrated to preserve high anatomical details, even at considerable compressing ratios. Undersampled reconstruction, brings together a lower phototoxicity of the technique and a shorter time required to volumetrically acquire signal. Nonetheless, this comes with an higher complexity of the matrix formulation of the imaging activity, which needs heavy computations to output a 3D volume reconstruction.

The technique has been extensively tested in different configuration of illumination and detection lenses, implying different Field of View and illuminated regions. Each of the configurations presented was suited for the imaging of a particular sample, which had the constraint of being motionless all along the measurement routine, to prevent the formation of moving artefacts. To this extent, it has been shown how further signal modulation as in the case of a single exponential photobleaching, might be detrimental for the inversion of the problem. However, it has also been demonstrated how to easily remove the so induced artifacts. Nonetheless further hardware implementation aimed at a more efficient LED radiation harvesting might reduce the exposure time, making the technique suitable to investigate fast biological processes. The technique is thus suited for large, fixed or anesthetized cleared or transparent samples up to mms sizes thanks to the lateral volume extension performed with the illumination lens movement synchronized with the sensor reading.

A deconvolution algorithm has also been developed and investigated, to improve image quality over the sampled volume. This has been implemented after simulation of the detection PSF. Nonetheless the algorithm efficacy in both SNR improvement and defocus is limited only to a small axially extended volume. Yet, no aberrations have been considered in the imaging model, which could lead to a further improvement in the reconstruction quality. To this extent, elements with tunable optical power like electrically tunable lenses inserted in the detection could further improve the axial extension of the reconstructed volume.

Altogether, the designed microscopy setup and the presented reconstruction technique, make a powerful tool for imaging over a large volume, without any sample translation or probe induced artifacts and with a relevant reduction in phototoxicity and total acquisition time.

5 APPENDICES

APPENDIX A: DEPTH OF FIELD

The axial resolution of an imaging system is a expressed in different terms if compared to its lateral resolution. Due to terminology, one may think that an image plane corresponds to a geometrical plane with no extension along the optical axis but, even in the condition of ideal optical elements (therefore with no aberrations), each point of the image gives rise to a diffraction pattern which extends around the source point itself. Furthermore, axial resolution is not simply defined by the wave optics, but it is also determined by the detector extension. These two components are respectively predominant at high and low numerical aperture, and their overall contribution is given by the formula:

$$DOF = \frac{n \cdot \lambda}{NA^2} + \frac{n}{M \cdot NA} \cdot e \qquad \text{A.1}$$

with DOF being the system depth of field, λ the light wavelength, NA the objective numerical aperture, M its lateral magnification and e the pixel lateral dimension.

As described in the main body of the thesis. It is possible to experimentally evaluate the PSF by imaging ideal point emitters. In practice they are used samples of fluorescent beads which are embedded in a transparent gel, namely agarose or phytagel. These gels have the goal to hold a bead still in the object plane, being surrounded in a homogeneous medium. In real systems calibration experiments, a point source can be considered as such if it is much smaller than the system resolution described in Eq. 1.1: for example, considering a situation in which an objective lens of $NA = 0.14$ is used to image a point emitting at $580\ nm$, a bead smaller than $\approx 2070\ \mu m$ must be used. Nevertheless, imaging complex biological samples and tissues might introduce unpredictable deviation of the PSF from its theoretical form, which arise from media as well as index inhomogeneities and scattering or absorbing centres.

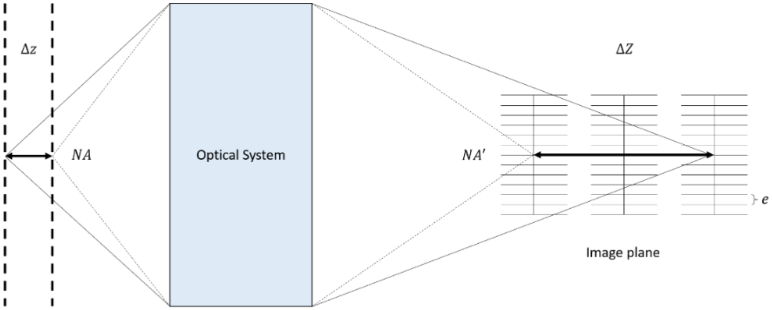

Figure xli: Depth of field and depth of focus variation. Here Δz is the depth of field, ΔZ is the depth of focus, NA the numerical aperture of the objective lens, NA' the numerical aperture of the tube lens, M the magnification and e the detector pixel length.

APPENDIX B: FLUORESCENCE

Fluorescence is that physical phenomena in which a molecule emits light after having absorbed electromagnetic radiation. It holds that in most cases, the fluorescence photon has a lower energy that that absorbed by the molecule; equivalently, fluorescence emission is at a longer wavelength compared to that of the excitation.

To describe this process in the simplest way, we first consider a two-level fluorescent molecule. When a wave is impinging on the system, the energy absorption rate is determined by a cross-section with the following relation:

$$W_{abs} = \sigma_{abs}\, I_i \qquad \text{B.1}$$

where I_i is the light intensity and σ_{abs} depends upon the radiation wavelength. Once the incoming energy is absorbed it might then be reemitted as fluorescence, the likelihood of this to happen is given by the radiative quantum yield q_r, which is defined as ration between the number of emitted (fluorescence photon) and the total number of absorbed photons. As for absorption, so for fluorescence, it can be written a similar relation as that in Eq. A.1:

$$W_f = \sigma_f\, I_i = q_r\, \sigma_{abs}\, I_i, \qquad \text{B.2}$$

with σ_f being the fluorescence cross section.

The easiest way to model the fluorescence emission is that in which only a two-level system is considered: here, the two levels are mostly referred to as ground and excited state and are such that their energy difference, $E(e) - E(g) = \Delta E$ is greatly larger than the thermal energy of the environment,

$k_B T_{room}$ so that the state transition is very unlikely to happen spontaneously. However, considering a real molecule a two level, closed system is an oversimplification which does not consider the many vibrational or rotation sublevels of the molecule orbitals, thus being inadequate to describe the fluorescence emission.

To better described real molecule dynamics, they must be introduced also non radiative paths, which result in a system relaxation, without photon emission, together with the presence of a third energy level, namely the triplet state, as shown in Figure xlii. On top of that, intersystem crossing might take place, in which the molecule relaxes non radiatively, from an excited state toward a state of lower energy which is not the ground state (denoted with the isc subscript). With these physical conditions, the temporal evolution of the population of the three states, g, e and t can be described by the following matrix equation:

$$\frac{d}{dt}\begin{pmatrix} g \\ e \\ t \end{pmatrix} = \begin{pmatrix} -\alpha & k_r + k_{nr} & k_t \\ \alpha & -(k_r + k_{nr} + k_{isc}) & 0 \\ 0 & k_{isc} & -k_t \end{pmatrix} \begin{pmatrix} g \\ e \\ t \end{pmatrix} = M \begin{pmatrix} g \\ e \\ t \end{pmatrix}, \quad \text{B.3}$$

where k denotes the rate of a certain transition (r and nr for radiative and non-radiative, isc for inter system crossing, t for triplet state) and α is the excitation rate. Since eq. A.3 only considers closed system in which the overall electron population is a constant, $\det(M) = 0$.

The mathematical representation of a real molecule, however, still lacks something. When in fact a molecule exits its singlet state due to intersystem crossing, it does not emit any photon. This transition is not permanent, and it lasts on average a time which is determined by the triplet state lifetime $\tau_t = \frac{1}{k_t}$. In fluorescence imaging, it must be considered also that physical phenomenon which permanently removes the molecule from its singlet state, which then enters a dark non emitting state: photobleaching. Photobleaching may be induced by overexposing the molecule to light and it negatively affect *in vivo* imaging possibilities. This tedious problem is differently explained in different molecules and media, but it can be mathematically formulated by introducing another, dark state b, with rates respectively k_{eb} and k_{tb}, as depicted in Figure xlii.

$$\frac{d}{dt}\begin{pmatrix} g \\ e \\ t \end{pmatrix} = \begin{pmatrix} -\alpha & k_r + k_{nr} & k_t \\ \alpha & -(k_r + k_{nr} + k_{isc} + k_{eb}) & 0 \\ 0 & k_{isc} & -(k_t + k_{tb}) \end{pmatrix}\begin{pmatrix} g \\ e \\ t \end{pmatrix} = \qquad \text{B.4}$$

$$= M\begin{pmatrix} g \\ e \\ t \end{pmatrix},$$

Since the photobleached state is not accessible, the system now becomes open, i.e., $\det(M) \neq 0$.

In science, many natural mechanisms affecting the light emission capabilities of a luminous molecule have been intensively studied, since such mechanism are more likely to decrease the quantum yield of a molecule, rather than increasing. Have presented before, intersystem crossing or resonant energy transfer are two of these mechanisms and are relatively well understood. Conversely, photobleaching has still many questions unanswered, however, from experimental observations it is clear how it is strongly related to the molecule energy levels, rate coefficients and external environment. With the term environment it is also meant an eventual over exposition of the molecule to incoming light radiation which may end up in a permanent, dark molecule state. In literature, many strategies of reducing photobleaching have been presented, such as two photons excitation or incoherent sources. Anyway, microscopy techniques as LSFM or SVIM offers smart solutions to overcome, or at least decrease photobleaching by optimizing the acquisition process, as explained in 1.

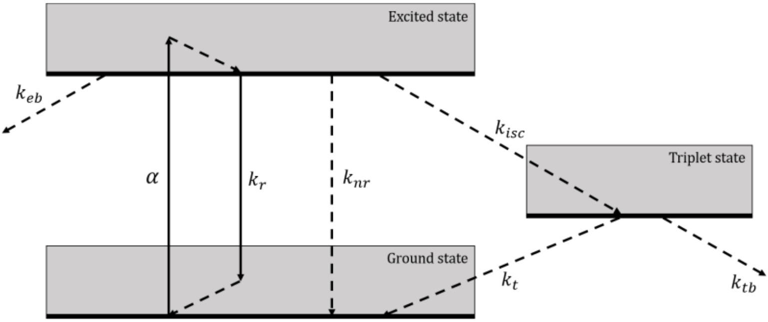

Figure xlii: Schematic representation of the possible transition between states of a fluorophore. The molecule absorbs a photon transitioning from the ground state to the excited state. Then, it relaxes down to the lower vibrational level of the excited state.

APPENDIX C: SAMPLE PREPARATION AND CLEARING METHODS

One of the main assumptions in fluorescence imaging is that of having a transparent sample, which is only detectable through its emitting molecules. This condition also implies that the specimen under study has an optically homogeneous structure, whose refraction index is perfectly matched by the imaging medium. Any unwanted media interface or inhomogeneity would in fact inevitably cause a degradation in imaging performances, both with regards to the quality of the illumination shape and to the detected signal. To this extent, in fluorescence imaging is of crucial importance the way in which the fluorophores are labelled i.e., are set to emit fluorescence, and the resulting optical properties of the tagged sample.

To this extent, one of the most widespread protocol is immunostaining, with which thanks to the use of specific antibodies, fluorescent protein are expressed in different region of the tissue [112]. The expressed proteins determine with their characteristic spectra the excitation and emitted photon frequencies. Many of them have been synthetized in recent years, one of the most famous family of is that of fluorescent proteins. The Green Fluorescent Protein (GFP) is one of its members which emits green fluorescence (peaked at $532\,nm$) upon blue excitation. Cyanine (CY5), which is used in this work, is excited at $630\,nm$ and consequently emits at around $670\,nm$.

In immunostaining, antibodies detect and bind with a specific protein, so that the wanted fluorophores is chemically bound to the site. By doing so, fluorescent molecules will give light signal from the region of interest.

Furthermore, as previously highlighted, a transparent specimen is needed to correctly image the stained luminous proteins: unluckily in nature there are only a limited number, such as embryos of *Danio rerio* (presented in this thesis) and a few other biological tissues like cornea and retina. A possible way to overcome this problem is Optical tissue clearing (OTC) [113]. However, fluorescent staining and OTC must not mutually hinder, i.e., the chemical solution needed for clearing must not modify the fluorescence quantum yield of the labelled tissue.

Clearing Methods

A fast transition between low and high refractive index strongly affects good fluorescence imaging. In biological samples it is common to have high index portion of the sample embedded in parts at higher aqueous content (i.e., with lower n) as it is the case for membranes, collagen or fibres which are contained in cytosol or interstitial fluid. To avoid such condition, OTC has been developed to obtain an imaged sample as optically transparent as possible, so to increase illumination and detection quality in fluorescence microscopy.

Among the techniques which benefitted the most from OTC, LSFM and SVIM have to demonstrated to image large volumes [24], [25], and it similarly did sm-SVIM proposed in this thesis. The clearing process can be pursued in several ways, all of them imply either a removal, replacement or modification of the former, scattering tissue [114]. Nonetheless, tissue clearing is divided into two main categories: the first based on tissue dehydration and lipid solvation, while the second involves modern protocols with aqueous solutions. In solvent based protocols, the sample must go through two major steps [115], namely sample dehydration and lipid solvation.

Solvent engineering and testing have proceeded along the years, at the current state of art the most widely used to remove water are methanol or tetrahydrofuran (THF). Altogether, the chemical action of such solvents also affects the protein and lipid composition of the former tissue leading to a high index sample ($n > 1.5$). After dehydration, a second step aimed at lipid removal and tissue infiltration is taken. Two of the most common solvents used at this point in the protocol are benzyl alcohol with benzyl benzoate (BABB) and dibenzyl (DBE), which have been also used in the clearing of the presented samples. Nonetheless, the presented protocol may incur in two major drawbacks. The chemical action of the used solvents, which dehydrates the tissue, may in fact decrease the fluorescent quantum yield of the fluorophores, by changing them environment. Furthermore, such solvents are mostly toxic for human and may also induce a tissue shrinkage in time.

A possible cheaper clearing approach is given by hydrophobic solvents, which are based on aqueous solutions. In these techniques, the sample it is firstly kept in an high index aqueous solution (such as thiodiethanol, TDE) with dissolved molecules. The composition of the solvents results in a penetration depth in tissue which is shorter that that given by more chemically aggressive procedures, making this last more suitable for smaller samples.

A more complicated clearing strategy is Hyperhydration. Here, the tissue is put in a detergent for a period which may even last months. Little by little, different solvents (like urea) are gradually introduced in the same solution as the sample, gradually infiltrating among the tissues components and changing the overall refractive index. Nonetheless hyperhydration might induce a remarkable expansion of the sample volume and it might also remove its proteins content up to 40%, strongly affecting fluorescence.

The last clearing process that will be briefly described takes the name of hydrogel embedding. In this technique, to avoid the unwanted protein removal given by other approaches, the sample is firstly embedded in an hydrogel. Then, the lipids are removed by electrophoresis, which speeds up the process that otherwise would take weeks to be effective. As final step, the sample is immersed in a clearing solution. A summary of the cited protocols is given in Figure xliii.

Appendix C: Sample preparation and clearing methods

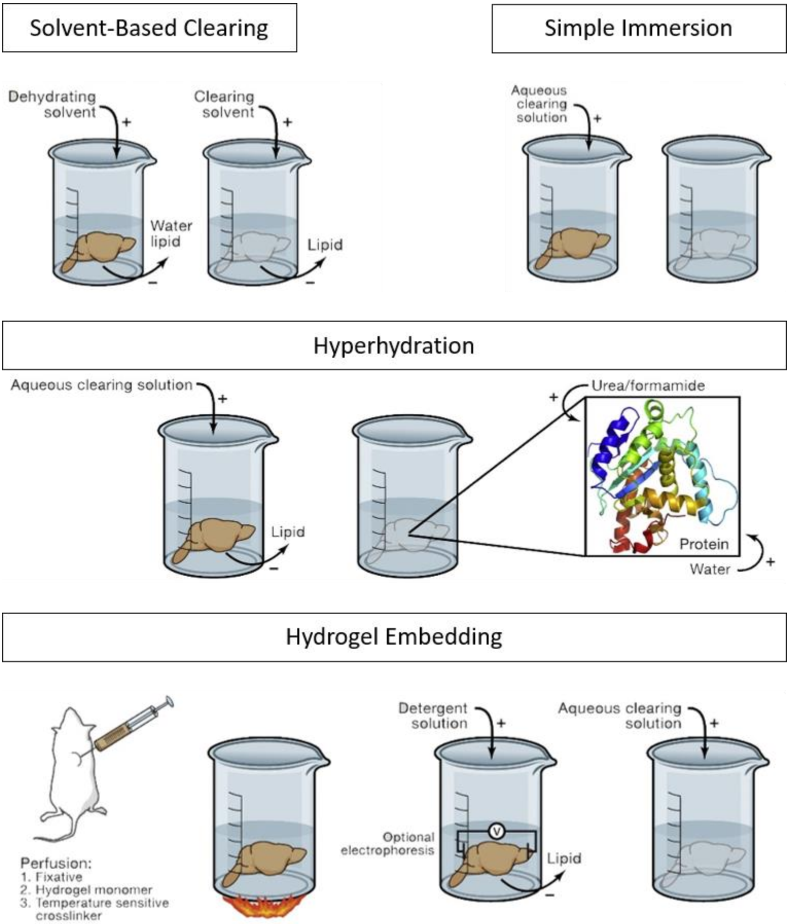

Figure xliii: Schematic classification of the different clearing methods [118].

To correctly perform a measurement in sm-SVIM, the sample needs to keep a constant volume and of course it needs to keep a sufficient fluorescence signal intensity.

Different samples cleared with different protocols have been imaged and are presented in this thesis work.

APPENDIX D: SPARSITY AND COHERENCE

A signal is compressible if its information is distributed over few nonzero entries of its vectorial representation, thus implying that the null entries can be easily discarded at a small cost in terms of signal representation accuracy or even without any loss. The property of being compressible can be mathematically described, evaluated and quantified. In fact, a signal $\boldsymbol{\chi}$ is said to be K-sparse if the number of its non-zero components is K. The latter condition can be formulated as:

$$\|\boldsymbol{\chi}\|_0 < K, \qquad \text{D.1}$$

where with $\|\cdot\|_0$ is represented the l_0 norm of a vector, which numbers its non-null components. With said definition, it is easy to state that an highest signal sparsity implies a small K.

It is reported in [47], and it has also been demonstrated in this thesis work, that many real world signals can be represented only by their most important entries, thus can be compressed. Said n the number of the signal entries, this means that $K \ll n.$ With this being said, it follows that those signals which may have a concise representation in a certain domain, in their complete representation carry redundant information, in form of zero element or periodic features. To this extent, Compressive Sensing aims at solving an ill-posed problem by enforcing a sparsity constraint on the retrieved solution. Said ill-posedness comes from a fewer measurement set, conditions that is of benefits in many applications, as described in the main body of the text.

Mathematically speaking, enforcing sparsity on a signal feature (its spatial representation, its gradient etc.) does not grant for the uniqueness of the solution: there might be a whole family of false signals satisfying said enforced features. To further decrease the population of the solution ensemble, it is of help the tailored designed of the sampling matrix Φ, which must encode information in the most efficient way possible: the better the sampling strategy, the higher the degree of compression obtained.

It holds that the capability of efficiently seizing the representation feature of a vector, can be mathematically described by a matrix operation between the sampling and the representation basis. Considering Φ and W as sampling and representation maps, respectively, it holds that their coherence is represented by:

$$\mu(\Phi, W) = \sqrt{n} \cdot \max_{1 \leq k,j \leq n} |\langle \phi_{\mathrm{k}}, w_k \rangle|, \qquad \text{D.2}$$

where each of the two basis sets is assumed to be a complete orthonormal set. The highest possible coherence can be obtained by considering $\Phi = W$, thus implying a maximum degree of coherence which is $\sqrt{n}$, conversely, it can be demonstrated that coherence is lower bound by 1. Therefore, it is true that $1 \leq \mu(\Phi, W) \leq \sqrt{n}$.

Sampling a represented signal with a measurement set which is highly incoherent with the former, guarantees that at each measurement step, only the key signal information is seized, thus yielding high compression capability. Considering a K-sparse signal $\boldsymbol{\chi} \epsilon \mathbb{R}^n$, represented by the linear rule W into a sparse representation, and yet exploiting a measurement orthonormal set Φ, with basis elements $\phi_k \epsilon \mathbb{R}^n$, the minimum number of measurements m [47] that are theoretically needed for a lossless reconstruction is:

$$m \geq C \cdot \mu^2(\Phi, W) \cdot K \cdot \log(n), \tag{D.3}$$

with C being a positive constant.

In the light of this, the higher the sparsity of the signal, the fewer the measurement needed. Furthermore, m is also affected by the square of the mutual coherence of representation and sampling matrices. Finally, in the case of maximum coherence (worst case scenario in a compressed schema), $\mu(\Phi, W) = 1$, $m \sim \log(n)$, which for big n follows the conventional inversion procedures.

BIBLIOGRAPHY

[1] J. Mertz, *Introduction to Optical Microscopy*. 2019.

[2] P. Shaw, "Deconvolution in 3-D optical microscopy," *The Histochemical Journal*. 1994, doi: 10.1007/BF00158201.

[3] D. S. C. Biggs, "A Practical Guide to Deconvolution of Fluorescence Microscope Imagery," *Micros. Today*, 2010, doi: 10.1017/s1551929510991311.

[4] J. B. Sibarita, "Deconvolution microscopy," *Advances in Biochemical Engineering/Biotechnology*. 2005, doi: 10.1007/b102215.

[5] P. Sarder and A. Nehorai, "Deconvolution methods for 3-D fluorescence microscopy images," *IEEE Signal Processing Magazine*. 2006, doi: 10.1109/MSP.2006.1628876.

[6] M. B. Cannell, A. McMorland, and C. Soeller, "Image enhancement by deconvolution," in *Handbook of Biological Confocal Microscopy: Third Edition*, 2006.

[7] C. M. Lo and A. A. Sawchuk, "Nonlinear Restoration Of Filtered Images With Poisson Noise," in *Applications of digital image proceesing III*, Dec. 1979, pp. 84–95, doi: 10.1117/12.958229.

[8] C. Preza and J.-A. Conchello, "Depth-variant

maximum-likelihood restoration for three-dimensional fluorescence microscopy," *J. Opt. Soc. Am. A*, 2004, doi: 10.1364/josaa.21.001593.

[9] D. S. C. Biggs, "3D deconvolution microscopy," *Current Protocols in Cytometry*. 2010, doi: 10.1002/0471142956.cy1219s52.

[10] J. Huisken, J. Swoger, F. Del Bene, J. Wittbrodt, and E. H. K. Stelzer, "Optical sectioning deep inside live embryos by selective plane illumination microscopy," *Science (80-.).*, vol. 305, no. 5686, pp. 1007–1009, Aug. 2004, doi: 10.1126/science.1100035.

[11] P. P. Laissue, L. Roberson, Y. Gu, C. Qian, and D. J. Smith, "Long-term imaging of the photosensitive, reef-building coral Acropora muricata using light-sheet illumination," *Sci. Rep.*, vol. 10, no. 1, p. 10369, Dec. 2020, doi: 10.1038/s41598-020-67144-w.

[12] M. Weber and J. Huisken, "Light sheet microscopy for real-time developmental biology," *Curr. Opin. Genet. Dev.*, vol. 21, no. 5, pp. 566–572, Oct. 2011, doi: 10.1016/j.gde.2011.09.009.

[13] T. A. Planchon *et al.*, "Rapid three-dimensional isotropic imaging of living cells using Bessel beam plane illumination," *Nat. Methods*, 2011, doi: 10.1038/nmeth.1586.

[14] A. Costa, A. Candeo, L. Fieramonti, G. Valentini, and A. Bassi, "Calcium Dynamics in Root Cells of Arabidopsis thaliana Visualized with Selective Plane Illumination Microscopy," *PLoS One*, 2013, doi: 10.1371/journal.pone.0075646.

[15] F. O. Fahrbach, F. F. Voigt, B. Schmid, F. Helmchen, and J. Huisken, “Rapid 3D light-sheet microscopy with a tunable lens,” *Opt. Express*, 2013, doi: 10.1364/oe.21.021010.

[16] R. Tomer *et al.*, “SPED Light Sheet Microscopy: Fast Mapping of Biological System Structure and Function,” *Cell*, vol. 163, no. 7, pp. 1796–1806, Dec. 2015, doi: 10.1016/j.cell.2015.11.061.

[17] J. B. Pawley, *Handbook of biological confocal microscopy: Third edition*. 2006.

[18] J. Huisken and D. Y. R. Stainier, “Selective plane illumination microscopy techniques in developmental biology,” *Development*. 2009, doi: 10.1242/dev.022426.

[19] O. E. Olarte, J. Andilla, E. J. Gualda, and P. Loza-Alvarez, “Light-sheet microscopy: a tutorial,” *Adv. Opt. Photonics*, vol. 10, no. 1, p. 111, Mar. 2018, doi: 10.1364/AOP.10.000111.

[20] S. Mori, “Side lobe suppression of a Bessel beam for high aspect ratio laser processing,” *Precis. Eng.*, vol. 39, pp. 79–85, Jan. 2015, doi: 10.1016/j.precisioneng.2014.07.008.

[21] T. Vettenburg *et al.*, “Light-sheet microscopy using an Airy beam,” *Nat. Methods*, vol. 11, no. 5, pp. 541–544, May 2014, doi: 10.1038/nmeth.2922.

[22] P. Hoyer *et al.*, “Breaking the diffraction limit of light-sheet fluorescence microscopy by RESOLFT,” *Proc. Natl. Acad. Sci.*, vol. 113, no. 13, pp. 3442–3446, Mar. 2016, doi: 10.1073/pnas.1522292113.

[23] M. Friedrich, Q. Gan, V. Ermolayev, and G. S. Harms, “STED-SPIM: Stimulated Emission Depletion Improves Sheet Illumination Microscopy Resolution,” *Biophys. J.*, vol. 100, no. 8, pp. L43–L45, Apr. 2011, doi: 10.1016/j.bpj.2010.12.3748.

[24] R. M. Power and J. Huisken, “Adaptable, illumination patterning light sheet microscopy,” *Sci. Rep.*, vol. 8, no. 1, p. 9615, Dec. 2018, doi: 10.1038/s41598-018-28036-2.

[25] B.-J. Chang, V. D. Perez Meza, and E. H. K. Stelzer, “The mesoSPIM initiative: open-source light-sheet microscopes for imaging cleared tissue,” *Proc. Natl. Acad. Sci.*, vol. 114, no. 19, pp. 4869–4874, May 2017, doi: 10.1038/s41592-019-0554-0.

[26] T. V. Truong *et al.*, “High-contrast, synchronous volumetric imaging with selective volume illumination microscopy,” *Commun. Biol.*, 2020, doi: 10.1038/s42003-020-0787-6.

[27] M. Levoy, R. Ng, A. Adams, M. Footer, and M. Horowitz, “Light field microscopy,” 2006, doi: 10.1145/1179352.1141976.

[28] G. Calisesi *et al.*, “Spatially modulated illumination allows for light sheet fluorescence microscopy with an incoherent source and compressive sensing,” *Biomed. Opt. Express*, vol. 10, no. 11, p. 5776, Nov. 2019, doi: 10.1364/BOE.10.005776.

[29] M. A. A. Neil, R. Juškaitis, and T. Wilson, “Method of obtaining optical sectioning by using structured light in a conventional microscope,” *Opt. Lett.*, vol. 22, no. 24,

p. 1905, Dec. 1997, doi: 10.1364/OL.22.001905.

[30] M. G. L. Gustafsson, “Nonlinear structured-illumination microscopy: Wide-field fluorescence imaging with theoretically unlimited resolution,” *Proc. Natl. Acad. Sci.*, vol. 102, no. 37, pp. 13081–13086, Sep. 2005, doi: 10.1073/pnas.0406877102.

[31] G.-H. Chen, J. Tang, and S. Leng, “Prior image constrained compressed sensing (PICCS): A method to accurately reconstruct dynamic CT images from highly undersampled projection data sets,” *Med. Phys.*, vol. 35, no. 2, pp. 660–663, Jan. 2008, doi: 10.1118/1.2836423.

[32] M. Lustig, D. L. Donoho, J. M. Santos, and J. M. Pauly, “Compressed Sensing MRI,” *IEEE Signal Process. Mag.*, vol. 25, no. 2, pp. 72–82, Mar. 2008, doi: 10.1109/MSP.2007.914728.

[33] L. Feng, T. Benkert, K. T. Block, D. K. Sodickson, R. Otazo, and H. Chandarana, “Compressed sensing for body MRI,” *J. Magn. Reson. Imaging*, vol. 45, no. 4, pp. 966–987, Apr. 2017, doi: 10.1002/jmri.25547.

[34] C. M. Watts *et al.*, “Terahertz compressive imaging with metamaterial spatial light modulators,” *Nat. Photonics*, vol. 8, no. 8, pp. 605–609, Aug. 2014, doi: 10.1038/nphoton.2014.139.

[35] W. L. Chan, K. Charan, D. Takhar, K. F. Kelly, R. G. Baraniuk, and D. M. Mittleman, “A single-pixel terahertz imaging system based on compressed sensing,” *Appl. Phys. Lett.*, vol. 93, no. 12, p. 121105, Sep. 2008, doi: 10.1063/1.2989126.

[36] X. Li, O. Dyck, S. V. Kalinin, and S. Jesse, “Compressed Sensing of Scanning Transmission Electron Microscopy (STEM) With Nonrectangular Scans,” *Microsc. Microanal.*, vol. 24, no. 6, pp. 623–633, Dec. 2018, doi: 10.1017/S143192761801543X.

[37] A. Stevens, H. Yang, L. Carin, I. Arslan, and N. D. Browning, “The potential for Bayesian compressive sensing to significantly reduce electron dose in high-resolution STEM images,” *Microscopy*, vol. 63, no. 1, pp. 41–51, Feb. 2014, doi: 10.1093/jmicro/dft042.

[38] R. Baraniuk and P. Steeghs, “Compressive radar imaging,” 2007, doi: 10.1109/RADAR.2007.374203.

[39] J.-L. Starck and J. Bobin, “Astronomical Data Analysis and Sparsity: From Wavelets to Compressed Sensing,” *Proc. IEEE*, vol. 98, no. 6, pp. 1021–1030, Jun. 2010, doi: 10.1109/JPROC.2009.2025663.

[40] S. Wäldchen, J. Lehmann, T. Klein, S. van de Linde, and M. Sauer, “Light-induced cell damage in live-cell super-resolution microscopy,” *Sci. Rep.*, vol. 5, no. 1, p. 15348, Dec. 2015, doi: 10.1038/srep15348.

[41] T. Hastie, M. R. Tibshirani, and H. Wainwright, *Statistical Learning with Sparsity: The Lasso and Generalizations*. CRC press, 2015.

[42] S. Ruder, “An overview of gradient descent optimization algorithms *,” *arXiv*, vol. 1609.04747, 2017.

[43] W. W. W. W. Hager and H. Zhang, “A Survey of Nonlinear Conjugate Gradient Methods,” *Pacific J. Optim.*, vol. 2, no. 1, pp. 35–58, 2006.

[44] S. S. Chen, D. L. Donoho, and M. A. Saunders, “Atomic Decomposition by Basis Pursuit,” 2001.

[45] J. Romberg, “Imaging via compressive sampling: Introduction to compressive sampling and recovery via convex programming,” *IEEE Signal Process. Mag.*, vol. 25, no. 2, pp. 14–20, 2008, doi: 10.1109/MSP.2007.914729.

[46] D. Donoho and J. Tanner, “Observed universality of phase transitions in high-dimensional geometry, with implications for modern data analysis and signal processing,” *Philos. Trans. R. Soc. A Math. Phys. Eng. Sci.*, vol. 367, no. 1906, pp. 4273–4293, Nov. 2009, doi: 10.1098/rsta.2009.0152.

[47] E. J. Candes and M. B. Wakin, “An introduction to compressive sampling: A sensing/sampling paradigm that goes against the common knowledge in data acquisition,” *IEEE Signal Process. Mag.*, vol. 25, no. 2, pp. 21–30, 2008, doi: 10.1109/MSP.2007.914731.

[48] A. Skodras, C. Christopoulos, and T. Ebrahimi, “The JPEG 2000 still image compression standard,” *IEEE Signal Process. Mag.*, vol. 18, no. 5, pp. 36–58, 2001, doi: 10.1109/79.952804.

[49] D. L. Donoho and X. Huo, “Uncertainty Principles and Ideal Atomic Decomposition,” 2001.

[50] R. Coifman, F. Geshwind, and Y. Meyer, “Noiselets,” *Appl. Comput. Harmon. Anal.*, vol. 10, no. 1, pp. 27–44, 2001, doi: 10.1006/acha.2000.0313.

[51] E. J. Candes and T. Tao, “Near-optimal signal recovery from random projections: Universal encoding

strategies?," *IEEE Trans. Inf. Theory*, vol. 52, no. 12, pp. 5406–5425, Dec. 2006, doi: 10.1109/TIT.2006.885507.

[52] D. L. Donoho, "Compressed sensing," *IEEE Trans. Inf. Theory*, vol. 52, no. 4, pp. 1289–1306, Apr. 2006, doi: 10.1109/TIT.2006.871582.

[53] D. Krishnan, T. Tay, and R. Fergus, "Blind deconvolution using a normalized sparsity measure," in *CVPR 2011*, Jun. 2011, pp. 233–240, doi: 10.1109/CVPR.2011.5995521.

[54] A. O. Waheb Bishara, Ting-Wei Su, Ahmet F Coskun, "Lensfree on-chip microscopy over a wide field-of-view using pixel super-resolution," *Opt. Express*, vol. 18, no. 11, pp. 11181–11191, 2010.

[55] L. Zhu, W. Zhang, D. Elnatan, and B. Huang, "Faster STORM using compressed sensing," *Nat. Methods*, vol. 9, no. 7, pp. 721–723, Jul. 2012, doi: 10.1038/nmeth.1978.

[56] Y. Xu, J. Chen, L. Liyang, and K. F. Kelly, "Compressive hyperspectral microscopy of nanomaterials," *RAPID 2018 - 2018 IEEE Res. Appl. Photonics Def. Conf.*, no. Figure 1, pp. 367–369, 2018, doi: 10.1109/RAPID.2018.8509015.

[57] N. C. Pégard, H.-Y. Liu, N. Antipa, M. Gerlock, H. Adesnik, and L. Waller, "Compressive light-field microscopy for 3D neural activity recording," *Optica*, vol. 3, no. 5, p. 517, May 2016, doi: 10.1364/OPTICA.3.000517.

[58] C. Wang *et al.*, "Computational Spectral Imaging Based

on Compressive Sensing," *Chinese Phys. Lett.*, vol. 34, no. 10, p. 104203, Oct. 2017, doi: 10.1088/0256-307X/34/10/104203.

[59] D. N. Wadduwage *et al.*, "Near-common-path interferometer for imaging Fourier-transform spectroscopy in wide-field microscopy," *Optica*, vol. 4, no. 5, p. 546, May 2017, doi: 10.1364/OPTICA.4.000546.

[60] D. S. Wilcox, G. T. Buzzard, B. J. Lucier, O. G. Rehrauer, P. Wang, and D. Ben-Amotz, "Digital compressive chemical quantitation and hyperspectral imaging," *Analyst*, vol. 138, no. 17, pp. 4982–4990, 2013, doi: 10.1039/c3an00309d.

[61] M. A. Neifeld and J. Ke, "Optical architectures for compressive imaging," *Appl. Opt.*, vol. 46, no. 22, p. 5293, Aug. 2007, doi: 10.1364/AO.46.005293.

[62] M. F. Duarte *et al.*, "Single-pixel imaging via compressive sampling," *IEEE Signal Process. Mag.*, vol. 25, no. 2, pp. 83–91, Mar. 2008, doi: 10.1109/MSP.2007.914730.

[63] M.-J. Sun and J.-M. Zhang, "Single-Pixel Imaging and Its Application in Three-Dimensional Reconstruction: A Brief Review," *Sensors*, vol. 19, no. 3, p. 732, Feb. 2019, doi: 10.3390/s19030732.

[64] V. Studer, J. Bobin, M. Chahid, H. S. Mousavi, E. Candes, and M. Dahan, "Compressive fluorescence microscopy for biological and hyperspectral imaging," *Proc. Natl. Acad. Sci.*, vol. 109, no. 26, pp. E1679–E1687, Jun. 2012, doi: 10.1073/pnas.1119511109.

[65] F. Soldevila *et al.*, “Single-pixel polarimetric imaging spectrometer by compressive sensing,” *Appl. Phys. B*, vol. 113, no. 4, pp. 551–558, Dec. 2013, doi: 10.1007/s00340-013-5506-2.

[66] Q. Guo, H. Chen, Z. Weng, M. Chen, S. Yang, and S. Xie, “Compressive sensing based high-speed time-stretch optical microscopy for two-dimensional image acquisition,” *Opt. Express*, 2015, doi: 10.1364/oe.23.029639.

[67] E. Salvador-Balaguer, P. Latorre-Carmona, C. Chabert, F. Pla, J. Lancis, and E. Tajahuerce, “Low-cost single-pixel 3D imaging by using an LED array,” *Opt. Express*, 2018, doi: 10.1364/oe.26.015623.

[68] D. L. Donoho and P. B. Stark, “Uncertainty Principles and Signal Recovery,” *SIAM J. Appl. Math.*, 1989, doi: 10.1137/0149053.

[69] M. A. T. Figueiredo, R. D. Nowak, and S. J. Wright, “Gradient projection for sparse reconstruction: Application to compressed sensing and other inverse problems,” *IEEE J. Sel. Top. Signal Process.*, 2007, doi: 10.1109/JSTSP.2007.910281.

[70] D. E. N. Van Ewout Berg and M. P. Friedlander, “Probing the pareto frontier for basis pursuit solutions,” *SIAM J. Sci. Comput.*, 2008, doi: 10.1137/080714488.

[71] Y. Wu, M. Rosca, and T. Lillicrap, “Deep Compressed Sensing,” *36th Int. Conf. Mach. Learn. ICML 2019*, May 2019, [Online]. Available: http://arxiv.org/abs/1905.06723.

[72] N. Radwell, K. J. Mitchell, G. M. Gibson, M. P. Edgar, R. Bowman, and M. J. Padgett, “Single-pixel infrared and visible microscope,” *Optica*, vol. 1, no. 5, p. 285, Nov. 2014, doi: 10.1364/OPTICA.1.000285.

[73] M. P. Edgar, M.-J. Sun, G. M. Gibson, G. C. Spalding, D. B. Phillips, and M. J. Padgett, “Real-time 3D video utilizing a compressed sensing time-of-flight single-pixel camera,” 2016, doi: 10.1117/12.2239113.

[74] F. Rousset, N. Ducros, A. Farina, G. Valentini, C. D’Andrea, and F. Peyrin, “Adaptive Basis Scan by Wavelet Prediction for Single-Pixel Imaging,” *IEEE Trans. Comput. Imaging*, vol. 3, no. 1, pp. 36–46, Mar. 2017, doi: 10.1109/TCI.2016.2637079.

[75] F. Soldevila, E. Salvador-Balaguer, P. Clemente, E. Tajahuerce, and J. Lancis, “High-resolution adaptive imaging with a single photodiode,” *Sci. Rep.*, 2015, doi: 10.1038/srep14300.

[76] B. Sun, S. S. Welsh, M. P. Edgar, J. H. Shapiro, and M. J. Padgett, “Normalized ghost imaging,” *Opt. Express*, vol. 20, no. 15, p. 16892, Jul. 2012, doi: 10.1364/OE.20.016892.

[77] B. Sun *et al.*, “3D Computational Imaging with Single-Pixel Detectors,” *Science (80-.).*, vol. 340, no. 6134, pp. 844–847, May 2013, doi: 10.1126/science.1234454.

[78] N. Huynh, E. Zhang, M. Betcke, S. Arridge, P. Beard, and B. Cox, “Single-pixel optical camera for video rate ultrasonic imaging,” *Optica*, vol. 3, no. 1, p. 26, Jan. 2016, doi: 10.1364/OPTICA.3.000026.

[79] Martin Harwit and Neil J.A. Sloane, *Hadamard*

Transform Optics. Elsevier, 1979.

[80] Geadah and Corinthios, “Natural, Dyadic, and Sequency Order Algorithms and Processors for the Walsh-Hadamard Transform,” *IEEE Trans. Comput.*, vol. C–26, no. 5, pp. 435–442, May 1977, doi: 10.1109/TC.1977.1674860.

[81] M. J. Sun, L. T. Meng, M. P. Edgar, M. J. Padgett, and N. Radwell, “A Russian Dolls ordering of the Hadamard basis for compressive single-pixel imaging,” *Sci. Rep.*, 2017, doi: 10.1038/s41598-017-03725-6.

[82] Z. Zhang, X. Ma, and J. Zhong, “Single-pixel imaging by means of Fourier spectrum acquisition,” *Nat. Commun.*, 2015, doi: 10.1038/ncomms7225.

[83] M. G. L. Gustafsson, “Surpassing the lateral resolution limit by a factor of two using structured illumination microscopy. SHORT COMMUNICATION,” *J. Microsc.*, vol. 198, no. 2, pp. 82–87, May 2000, doi: 10.1046/j.1365-2818.2000.00710.x.

[84] D. Dan *et al.*, “DMD-based LED-illumination Super-resolution and optical sectioning microscopy,” *Sci. Rep.*, 2013, doi: 10.1038/srep01116.

[85] Z. Zhang, X. Wang, G. Zheng, and J. Zhong, “Hadamard single-pixel imaging versus Fourier single-pixel imaging,” *Opt. Express*, vol. 25, no. 16, p. 19619, Aug. 2017, doi: 10.1364/OE.25.019619.

[86] F. Rousset, N. Ducros, F. Peyrin, G. Valentini, C. D’Andrea, and A. Farina, “Time-resolved multispectral imaging based on an adaptive single-pixel camera,” *Opt. Express*, vol. 26, no. 8, p. 10550, Apr. 2018, doi:

10.1364/OE.26.010550.

[87] M. P. Edgar *et al.*, “Simultaneous real-time visible and infrared video with single-pixel detectors,” *Sci. Rep.*, vol. 5, no. 1, p. 10669, Sep. 2015, doi: 10.1038/srep10669.

[88] C. F. Higham, R. Murray-Smith, M. J. Padgett, and M. P. Edgar, “Deep learning for real-time single-pixel video,” *Sci. Rep.*, 2018, doi: 10.1038/s41598-018-20521-y.

[89] S. Gazit, A. Szameit, Y. C. Eldar, and M. Segev, “Super-resolution and reconstruction of sparse sub-wavelength images: erratum,” *Opt. Express*, vol. 18, no. 25, p. 26631, 2010, doi: 10.1364/oe.18.026631.

[90] E. Betzig *et al.*, “Imaging intracellular fluorescent proteins at nanometer resolution,” *Science (80-.).*, vol. 313, no. 5793, pp. 1642–1645, 2006, doi: 10.1126/science.1127344.

[91] M. J. Rust, M. Bates, and X. Zhuang, “Sub-diffraction-limit imaging by stochastic optical reconstruction microscopy (STORM),” *Nat. Methods*, vol. 3, no. 10, pp. 793–795, 2006, doi: 10.1038/nmeth929.

[92] H. P. Babcock, J. R. Moffitt, Y. Cao, and X. Zhuang, “Fast compressed sensing analysis for superresolution imaging using L1-homotopy,” *Opt. Express*, vol. 21, no. 23, pp. 28583–28596, 2013, doi: 10.1364/OE.21.028583.

[93] T. Cheng, D. Chen, B. Yu, and H. Niu, “Reconstruction of super-resolution STORM images using compressed sensing based on low-resolution raw images and

interpolation," *Biomed. Opt. Express*, vol. 8, no. 5, p. 2445, May 2017, doi: 10.1364/BOE.8.002445.

[94] S. Zhang, J. Wu, D. Chen, S. Li, B. Yu, and J. Qu, "Fast Frequency-Domain Compressed Sensing Analysis for High-Density Super-Resolution Imaging Using Orthogonal Matching Pursuit," *IEEE Photonics J.*, vol. 11, no. 1, pp. 1–8, Feb. 2019, doi: 10.1109/JPHOT.2018.2884730.

[95] L. Gu *et al.*, "High-Density 3D Single Molecular Analysis Based on Compressed Sensing," *Biophys. J.*, vol. 106, no. 11, pp. 2443–2449, Jun. 2014, doi: 10.1016/j.bpj.2014.04.021.

[96] J. Huang, M. Sun, K. Gumpper, Y. Chi, and J. Ma, "3D multifocus astigmatism and compressed sensing (3D MACS) based superresolution reconstruction," *Biomed. Opt. Express*, vol. 6, no. 3, p. 902, Mar. 2015, doi: 10.1364/BOE.6.000902.

[97] W. Meiniel *et al.*, "Reducing data acquisition for fast Structured Illumination Microscopy using Compressed Sensing," in *2017 IEEE 14th International Symposium on Biomedical Imaging (ISBI 2017)*, Apr. 2017, pp. 32–35, doi: 10.1109/ISBI.2017.7950461.

[98] J.-A. Conchello and J. W. Lichtman, "Optical sectioning microscopy," *Nat. Methods*, vol. 2, no. 12, pp. 920–931, 2005, doi: 10.1038/nmeth815.

[99] J. Mertz, "Optical sectioning microscopy with planar or structured illumination," *Nat. Methods*, vol. 8, no. 10, pp. 811–819, 2011, doi: 10.1038/nmeth.1709.

[100] K. Kelly, T. Takhar, DharmpalSun, J. Laska, M. Duarte,

and R. Baraniuk, “Abstract: D19.00007 : Compressed Sensing for Multispectral and Confocal Microscopy,” 2007, doi: BAPS.2007.MAR.D19.7.

[101] T. Sun *et al.*, “Abstract: U36.00008 : Realization of Confocal and Hyperspectral Microscopy via Compressive Sensing,” 2008, [Online]. Available: http://meetings.aps.org/link/BAPS.2008.MAR.U36.8.

[102] P. Ye, J. L. Paredes, G. R. Arce, Y. Wu, C. Chen, and D. W. Prather, “Compressive confocal microscopy,” in *2009 IEEE International Conference on Acoustics, Speech and Signal Processing*, Apr. 2009, pp. 429–432, doi: 10.1109/ICASSP.2009.4959612.

[103] N. Pavillon and N. I. Smith, “Compressed sensing laser scanning microscopy,” *Opt. Express*, vol. 24, no. 26, p. 30038, Dec. 2016, doi: 10.1364/OE.24.030038.

[104] B. Francis, M. Mathew, and M. Arigovindan, “Image reconstruction from undersampled confocal microscopy data using multiresolution based maximum entropy regularization,” *J. Instrum.*, vol. 14, no. 07, pp. P07015–P07015, Jul. 2019, doi: 10.1088/1748-0221/14/07/P07015.

[105] V. J. Parot *et al.*, “Compressed Hadamard microscopy for high-speed optically sectioned neuronal activity recordings,” *J. Phys. D. Appl. Phys.*, vol. 52, no. 14, p. 144001, Apr. 2019, doi: 10.1088/1361-6463/aafe88.

[106] M. Born, E. Wolf, and E. Hecht, “ Principles of Optics: Electromagnetic Theory of Propagation, Interference and Diffraction of Light ,” *Phys. Today*, 2000, doi: 10.1063/1.1325200.

[107] R. Itoh, J. R. Landry, S. S. Hamann, and O. Solgaard, "Light sheet fluorescence microscopy using high-speed structured and pivoting illumination," *Opt. Lett.*, 2016, doi: 10.1364/ol.41.005015.

[108] Y. Li, M. Knöchelmann, and R. Lachmayer, "Beam pre-shaping methods using lenslet arrays for area-based high-resolution vehicle headlamp systems," *Appl. Sci.*, 2020, doi: 10.3390/app10134569.

[109] W.-S. Sun, C.-L. Tien, C.-H. Ma, and J.-W. Pan, "Compact LED projector design with high uniformity and efficiency," *Appl. Opt.*, 2014, doi: 10.1364/ao.53.00h227.

[110] J. W. Pan and H. H. Wang, "High contrast ratio prism design in a mini projector," *Appl. Opt.*, 2013, doi: 10.1364/AO.52.008347.

[111] A. Bassi, L. Fieramonti, C. D'Andrea, M. Mione, and G. Valentini, "In vivo label-free three-dimensional imaging of zebrafish vasculature with optical projection tomography," *J. Biomed. Opt.*, vol. 16, no. 10, p. 100502, 2011, doi: 10.1117/1.3640808.

[112] I. Laevsky, "Immunostaining," in *Atlas of Human Pluripotent Stem Cells*, 2012.

[113] A. Azaripour, T. Lagerweij, C. Scharfbillig, A. E. Jadczak, B. Willershausen, and C. J. F. Van Noorden, "A survey of clearing techniques for 3D imaging of tissues with special reference to connective tissue," *Progress in Histochemistry and Cytochemistry*. 2016, doi: 10.1016/j.proghi.2016.04.001.

[114] P. Ariel, "A beginner's guide to tissue clearing,"

International Journal of Biochemistry and Cell Biology. 2017, doi: 10.1016/j.biocel.2016.12.009.

[115] D. S. Richardson and J. W. Lichtman, “Clarifying Tissue Clearing,” *Cell*. 2015, doi: 10.1016/j.cell.2015.06.067.